

Johannes Kaschke

Complex Helical Metamaterials fabricated via STED-inspired Laser Lithography

2015
Dissertation

COMPLEX HELICAL METAMATERIALS FABRICATED VIA STED-INSPIRED LASER LITHOGRAPHY

Zur Erlangung des akademischen Grades eines
DOKTORS DER NATURWISSENSCHAFTEN
von der Fakultät für Physik des
Karlsruher Instituts für Technologie (KIT)

genehmigte

DISSERTATION

von

Dipl.-Phys. Johannes Michael Kaschke
geboren in Jena

Tag der mündlichen Prüfung: 11.12.2015

Referent: Prof. Dr. Martin Wegener

Korreferent: Prof. Dr. Carsten Rockstuhl

CONTENTS

PUBLICATIONS 1

1 INTRODUCTION 5

2 FUNDAMENTALS 9

2.1 Light-Matter Interaction 10

2.2 Dispersion in Natural Materials 14

2.3 Polarization and Jones Formalism 16

2.4 Bianisotropic Media and Chiro-optical Effects 23

2.5 Reciprocity Constraints 28

2.6 A Short Introduction to Metamaterials 31

3 THEORY OF HELICAL METAMATERIALS 37

3.1 Conventional Helical Metamaterials 38

3.2 Theory of N-Helical Metamaterials 47

3.3 Optimizing N-Helical Metamaterials 56

3.4 Designs beyond Polarizer Applications 62

4	EXPERIMENTAL METHODS	71
4.1	Laser Lithography	72
4.1.1	Fundamentals of Direct Laser Writing	72
4.1.2	Breaking the Diffraction Limit	77
4.1.3	Lithography Setup	82
4.2	Electrochemical Deposition of Metals	84
4.2.1	Fundamentals of Electrochemical Deposition	84
4.2.2	Gold Deposition in Polymer Templates	90
4.3	Fabrication Process	92
4.3.1	Substrate Preparation	92
4.3.2	STED-inspired Direct Laser Writing	94
4.3.3	Electrochemical Gold Deposition	95
4.3.4	Polymer Removal and Post-processing	97
4.4	Circular-Polarization Infrared Spectroscopy	99
5	EXPERIMENTAL RESULTS	103
5.1	Triple-helical Metamaterials	104
5.2	Broadband Circular-Polarization Converters	112
5.3	Discussion	115
5.4	Alternative Fabrication Approaches	118
5.4.1	Double-Inversion of Direct Laser Written Templates	118
5.4.2	Fabrication Approaches beyond Direct Laser Writing	119
6	CONCLUSIONS AND OUTLOOK	125

A NUMERICAL PARAMETER SWEEP 129

BIBLIOGRAPHY 133

ACKNOWLEDGMENTS 147

PUBLICATIONS

PARTS OF THIS THESIS HAVE ALREADY BEEN PUBLISHED . . .

. . . in scientific journals:

- J. Kaschke, J. K. Gansel, and M. Wegener, “On metamaterial circular polarizers based on metal N-helices”, *Opt. Express* **20**, 26012–26020 (2012)
- J. Kaschke, M. Blome, S. Burger, and M. Wegener, “Tapered N-helical metamaterials with three-fold rotational symmetry as improved circular polarizers”, *Opt. Express* **22**, 19936–19946 (2014)
- J. Kaschke, L. Blume, L. Wu, M. Thiel, K. Bade, Z. Yang, and M. Wegener, “A Helical Metamaterial for Broadband Circular Polarization Conversion”, *Adv. Opt. Mater.* **3**, 1411–1417 (2015)
- J. Kaschke and M. Wegener, “Gold triple-helix mid-infrared metamaterial by STED-inspired laser lithography”, *Opt. Lett.* **40**, 3986–3989 (2015)
- J. Kaschke and M. Wegener, “Optical and infrared helical metamaterials” (invited review article), *Nanophotonics*, accepted

. . . at scientific conferences (only own presentations):

- J. Kaschke, J. K. Gansel, J. Fischer, and M. Wegener, “Metamaterial Circular Polarizers Based on Metal N-Helices”, CLEO 2013, San José, CA, USA, June 2013
- J. Kaschke, J. K. Gansel, J. Fischer, M. Thiel, and M. Wegener, “Recent experimental progress on quadruple-helix based metamaterials” (invited talk), SPIE Optics+Photonics, San Diego, CA, USA, August 2013

- J. Kaschke, L. Blume, M. Thiel, W. Lin, Z. Yang, and M. Wegener, “Circular Polarization Converters Based on Coupled Pairs of Oppositely-Handed Gold Helices”, CLEO 2014, San José, CA, USA, June 2014
- J. Kaschke, M. Blome, S. Burger, M. Wegener, “Recent Progress on Triple-helix Gold-based Metamaterials” (invited talk), SPIE Photonics West, San Francisco, CA, USA, February 2015

ADDITIONAL RELATED WORK HAS ALREADY BEEN PUBLISHED . . .

. . . in scientific journals:

- J. K. Gansel, M. Latzel, A. Frölich, J. Kaschke, M. Thiel, and M. Wegener, “Tapered gold-helix metamaterials as improved circular polarizers”, *Appl. Phys. Lett.* **100**, 101109 (2012)
- T. Bückmann, N. Stenger, M. Kadic, J. Kaschke, A. Frölich, T. Kennerknecht, C. Eberl, M. Thiel, and M. Wegener, “Tailored 3D Mechanical Metamaterials Made by Dip-in Direct-Laser-Writing Optical Lithography”, *Adv. Mater.* **24**, 2710–2714 (2012)
- X. Liu, S. Klinkhammer, K. Sudau, N. Mechau, C. Vannahme, J. Kaschke, T. Mappes, M. Wegener, and Uli Lemmer, “Ink-jet-printed organic semiconductor distributed feedback laser”, *Appl. Phys. Express* **5**, 072101 (2012)
- A. W. Schell, J. Kaschke, J. Fischer, R. Henze, J. Wolters, M. Wegener, and Oliver Benson, “Three-dimensional quantum photonic elements based on single nitrogen vacancy-centres in laser-written microstructures”, *Sci. Rep.* **3** (2013)
- M. Thiel, J. Ott, A. Radke, J. Kaschke, and M. Wegener, “Dip-in depletion optical lithography of three-dimensional chiral polarizers”, *Opt. Lett.* **38**, 4252–4255 (2013)
- B. Richter, T. Pauloehrl, J. Kaschke, D. Fichtner, J. Fischer, A. M. Greiner, D. Wedlich, M. Wegener, G. Delaittre, C. Barner-Kowollik, and M. Bastmeyer, “Three-Dimensional Microscaffolds Exhibiting Spatially Resolved Surface Chemistry”, *Adv. Mater.* **25**, 6117–6122 (2013)

-
- J. Fischer, J. B. Mueller, J. Kaschke, T. J. A. Wolf, A.-N. Unterreiner, and M. Wegener, "Three-dimensional multi-photon direct laser writing with variable repetition rate", *Opt. Express* **21**, 26244–26260 (2013)
 - A. W. Schell, T. Neumer, Q. Shi, J. Kaschke, J. Fischer, M. Wegener, and O. Benson, "Laser-written parabolic micro-antennas for efficient photon collection", *Appl. Phys. Lett.* **105**, 231117 (2014)
 - J. Fischer, J. B. Mueller, A. S. Quick, J. Kaschke, C. Barner-Kowollik, and M. Wegener, "Exploring the Mechanisms in STED-Enhanced Direct Laser Writing", *Adv. Opt. Mater.* **3**, 221–232 (2015)

I INTRODUCTION

How do we characterize light? In a classical picture, any light we observe corresponds to a superposition of electromagnetic waves, each with a certain electric field strength, frequency, and polarization. The human eye is certainly of no use for a quantitative analysis of these physical parameters. It is impossible for us to determine absolute values for the wavelength or intensity of a light source with our bare eye, even if that light source is monochromatic. By comparing different monochromatic light sources, however, we can interpret different wavelengths as different colors and, for example, easily distinguish a green solid-state laser at 532 nm from a red helium-neon laser at 633 nm. Furthermore, we can also tell whether a light source is brighter or darker in comparison to a light source of the same wavelength and, thus, compare the modulus of the electric field strengths.

Different polarizations of light, on the other hand, remain mostly imperceptible to the human eye if we neglect small physiological effects like Haidinger's brush [1]. Despite our inability to see or determine the polarization state, polarized light plays an important role in everyday applications. At radio frequencies, for example, not only the design but also the orientation of the antenna is relevant when emitting or receiving electromagnetic waves.

Much more importantly today, polarizing components are implemented in almost any electronic device with a display or screen. Liquid-crystal displays are based on rotating and blocking linearly polarized light at visible frequencies and have been a breakthrough technology in enabling mobile electronics.

Polarized light, however, also appears naturally. Sailors fancy sunglasses with polarizing filters, as they reduce glare from the reflected light on wa-

ter, which is polarized, due to reflection at Brewster's angle. Similarly, in photography, linear polarizers enhance the contrast in images by decreasing glare from unwanted reflections. Additionally, scattered light from the atmosphere is also polarized and thus blocked, leading to a contrast-enhancing darkening of the blue sky in the photograph.

For circularly polarized light, on the other hand, stereoscopy in movie theaters is just one example of emerging applications. In order to create a three-dimensional image, two images filmed with a certain parallax are projected onto one polarization-conserving screen. The images are circularly polarized by employing linear polarizers in combination with quarter-wave plates. Low-cost glasses, given out to the viewers in the theater, use the same combination but in reverse order as eyepieces, thus, discriminating the two circular polarizations and transmitting only the correct image to each eye. In contrast to a system with solely linear polarizers, circularly polarized light allows the viewer to tilt his head without seeing parts of the wrong image.

Naturally, there is a much larger variety of applications for circularly polarized light in scientific research. In many modern microscopy methods, such as STED-microscopy for example, circularly polarized laser radiation is required in order to achieve the desired intensity profiles in the focus [2].

While in microscopy single or few particles are examined, large ensembles of particles and their collective properties can be measured with far-field optical spectroscopy. A particular challenge is the discrimination of so-called *chiral* molecules: molecules that lack any mirror symmetries and therefore cannot be superimposed onto their mirror image. Inspired by the most prominent macroscopic example for such objects, the word *chirality* stems from the Greek word for "hand": *cheir* ($\chi\epsilon\iota\rho$). Many biologically important molecules, like sugars or proteins for example, are chiral and, thus, come in two versions that are commonly called enantiomers. While in the human body often only one enantiomer can be produced or utilized, both enantiomers are produced in a laboratory environment. This must be carefully monitored, for example, when synthesizing chiral molecules for pharmaceutical applications. Due to the identical chemical composition, these enantiomers cannot be distinguished by their mass, solubility, or even their chemical reactivity in non-chiral environments. However, chiral molecules exhibit chiro-optical responses and their respective concentrations

can therefore be determined by measuring, for example, a difference in absorption for the two circular polarizations. This technique, referred to as circular-dichroism spectroscopy, relies on characteristic spectral features at UV wavelengths and has been introduced half a century ago [3, 4]. More recently, circular-dichroism spectroscopy has attracted increasing attention at infrared or terahertz frequencies where vibronic excitations of chiral macromolecules are of particular interest [5, 6].

In the light of everyday life and scientific applications combined, it becomes obvious that there is a rapidly growing need for high-quality circular polarizers. While linear polarization can be achieved by the use of wire-grid polarizers that offer good performance over unmatched spectral bandwidths, circular polarization has long relied on combinations of linear polarizers and retardation wave plates. Especially the latter are not readily available at infrared or terahertz frequencies. Furthermore, with chiro-optical responses being low in natural materials, *metamaterials* have been moving into focus for fabricating broadband circular polarizers for the desired frequency range.

While natural crystalline materials consist of atoms, ions, or molecules arranged in a periodic lattice, metamaterials, in analogy, are periodic arrangements of so-called meta-atoms. These substructures with sizes smaller than the operating wavelength are tailored to create effective optical parameters, either strongly enhancing certain optical effects or achieving ones that are not found at all in natural materials. By creating chiral unit cells, chiro-optical responses many orders of magnitude larger than those found in any natural material have been realized [7]. However, it was not until the introduction of metallic helical metamaterials, fabricated *via* direct laser writing (DLW) and subsequent electrochemical deposition, that true broadband operation was achieved [8]. With bandwidths of more than one octave and simultaneously large extinction ratios, helical metamaterials seem like the perfect counterpart to the wire-grid polarizer at first sight. However, conventional helical metamaterials exhibit undesired circular-polarization conversions.

By composing complex helical-metamaterial unit cells, where a single-helix serves only as a basic building block in a more sophisticated design, one can eliminate these unwanted effects. Combining helices of different handednesses on the other side, offers broadband asymmetric transmission. Such more complex helical-metamaterial designs are however out of reach

for fabrication with conventional direct laser writing.

The central topic of this thesis will therefore be the introduction of new helical-metamaterial designs with the goal of either eliminating circular-polarization conversions completely or to strongly enhance them for broadband asymmetric transmission. To achieve this goal experimentally, a novel fabrication process based on diffraction-unlimited STED-inspired direct laser writing is introduced and the operation at mid-infrared frequencies is demonstrated.

OUTLINE OF THIS THESIS

Chapter 2 in this thesis will cover the fundamentals to allow the reader a thorough understanding of the discussion in the chapters thereafter.

In Chapter 3, I will first review conventional helical metamaterials as they will serve as the basic building blocks for the following designs. I will then introduce the concept of N -helical metamaterials and discuss their fundamentally different principle of operation, as well as advantages and limitations, using a symmetry-based theoretical analysis. Additionally, I will discuss geometrical optimizations for these N -helical metamaterials by analyzing numerical calculations. In the final section, I will then introduce a different helical-metamaterial design for operation as a broadband circular-polarization converter.

Thereafter, I will present the experimental methods that have been employed to fabricate helical metamaterials in the scope of this thesis in Chapter 4. Furthermore, the entire fabrication process and the method of optical characterization at mid-infrared frequencies is explained in detail.

In Chapter 5, experimental results for both N -helical metamaterials and circular-polarization converters are presented. Furthermore, I will briefly discuss an alternative fabrication route based on a double-inversion process. The chapter is concluded by a discussion of the results and a comparison to other fabrication approaches beyond laser lithography.

Finally, I will conclude and summarize my work in Chapter 6.

2 FUNDAMENTALS

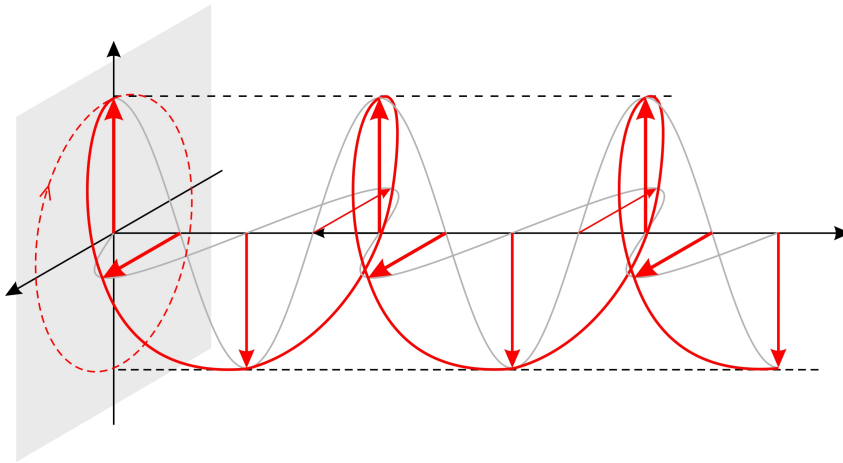


Illustration of the electric field vector for circular polarization.

In this chapter I will discuss the theoretical groundwork in order to ensure the reader's understanding in the chapters following thereafter. First, the interaction of light with matter, described by the macroscopic Maxwell's equations is introduced. With these equations at hand, the well-known Fresnel reflection and transmission coefficients are derived. Additionally, I will give a detailed discussion of the polarization state of light and its mathematical description via Jones formalism, both in linear- and circular-polarization basis. Subsequently, the theory of uniaxial bianisotropic media is discussed. Furthermore, I will highlight the importance of reciprocity and give a short introduction to the metamaterial concept.

Derivations for most of the following equations or findings are found in any common electrodynamics or optics text book. To the interested reader, I recommend References [9–12] where appropriate.

2.1 LIGHT-MATTER INTERACTION

The propagation of electromagnetic waves in free space, *i. e.*, vacuum, is described by Maxwell's equations, first formulated in 1865 [13, 14]. In the absence of free charges or currents, the electric field \vec{E} and the magnetic field \vec{H} are connected through these famous four equations,

$$\begin{aligned}\vec{\nabla} \times \vec{E}(\vec{r}, t) &= -\mu_0 \frac{\partial}{\partial t} \vec{H}(\vec{r}, t) \\ \vec{\nabla} \times \vec{H}(\vec{r}, t) &= \varepsilon_0 \frac{\partial}{\partial t} \vec{E}(\vec{r}, t) \\ \vec{\nabla} \cdot \vec{E}(\vec{r}, t) &= 0 \\ \vec{\nabla} \cdot \vec{H}(\vec{r}, t) &= 0,\end{aligned}\tag{2.1}$$

with the vacuum permittivity $\varepsilon_0 \approx 8.854 \cdot 10^{-12} \frac{\text{As}}{\text{Vm}}$ and the vacuum permeability $\mu_0 = 4\pi \cdot 10^{-7} \frac{\text{Vs}}{\text{Am}}$ [15]. Combining the first two equations, one can easily derive the wave equation for the electric field in free space

$$\left(\vec{\nabla}^2 - \frac{1}{c_0^2} \frac{\partial^2}{\partial t^2}\right) \vec{E}(\vec{r}, t) = 0,\tag{2.2}$$

with the vacuum speed of light $c_0 = (\sqrt{\varepsilon_0 \mu_0})^{-1}$. The corresponding wave equation for the magnetic field is naturally of identical form. Due to charged particles in media, *e. g.*, electrons or ions, these fields induce displaced charges and currents that in turn couple to the driving fields. Macroscopically, these microscopic charges and currents can be described as an effective polarization $\vec{P}(\vec{E}, \vec{H})$ and effective magnetization $\vec{M}(\vec{E}, \vec{H})$, yielding the electric displacement \vec{D} and the magnetic displacement \vec{B} :

$$\begin{aligned}\vec{D}(\vec{r}, t) &= \varepsilon_0 \vec{E}(\vec{r}, t) + \vec{P}(\vec{E}, \vec{H}) \\ \vec{B}(\vec{r}, t) &= \mu_0 \vec{H}(\vec{r}, t) + \mu_0 \vec{M}(\vec{E}, \vec{H}).\end{aligned}\tag{2.3}$$

In this first section, we will neglect coupling of the electric field components to the magnetic field components, thus, excluding chiral or bianisotropic media (see Section 2.4). This simplifies the dependence to $\vec{P}(\vec{E}, \vec{H}) = \vec{P}(\vec{E})$ and $\vec{M}(\vec{E}, \vec{H}) = \vec{M}(\vec{H})$. Furthermore, we limit our discussion to linear optics by a series expansion of the polarization and magnetization in which we neglect all terms of higher order. Generally, the polarization is then given by

$$\vec{P}(\vec{r}, t) = \varepsilon_0 \int_{-\infty}^{\infty} \int_{-\infty}^{\infty} \vec{\chi}_e(\vec{r}, \vec{r}', t, t') \vec{E}(\vec{r}', t') dt' d\vec{r}',\tag{2.4}$$

where $\overleftrightarrow{\chi}_e$ denotes the electric susceptibility tensor. I will also only discuss isotropic and homogeneous media in this first section. The former leads to $\overleftrightarrow{\chi}_e = \chi_e \overleftrightarrow{\mathbb{1}}$ and the latter to $\chi_e(\vec{r}, \vec{r}', t, t') = \chi_e(t', t)$. Without any particular time dependence and, furthermore, exploiting causality, the polarization in frequency domain can be simplified significantly to:

$$\vec{P}(\omega) = \varepsilon_0 \chi_e(\omega) \vec{E}(\omega). \quad (2.5)$$

Similarly, for the magnetization follows

$$\vec{M}(\omega) = \chi_m(\omega) \vec{H}(\omega), \quad (2.6)$$

with the magnetic susceptibility χ_m . Substituting these findings into equation 2.3, we find:

$$\begin{aligned} \vec{D}(\omega) &= \varepsilon_0 (1 + \chi_e(\omega)) \vec{E}(\omega) = \varepsilon_0 \varepsilon(\omega) \vec{E}(\omega) \\ \vec{B}(\omega) &= \mu_0 (1 + \chi_m(\omega)) \vec{H}(\omega) = \mu_0 \mu(\omega) \vec{H}(\omega). \end{aligned} \quad (2.7)$$

The material-specific parameters $\varepsilon(\omega)$ and $\mu(\omega)$ are called electric permittivity and magnetic permeability, respectively. In the absence of any free charges or currents, we can now write Maxwell's equations in frequency domain in a more general form which includes the material's response:

$$\begin{aligned} \vec{\nabla} \times \vec{E}(\vec{r}, \omega) &= i\omega \vec{B}(\vec{r}, \omega) \\ \vec{\nabla} \times \vec{H}(\vec{r}, \omega) &= -i\omega \vec{D}(\vec{r}, \omega) \\ \vec{\nabla} \cdot \vec{D}(\vec{r}, \omega) &= 0 \\ \vec{\nabla} \cdot \vec{B}(\vec{r}, \omega) &= 0. \end{aligned} \quad (2.8)$$

For every fixed frequency ω_0 , the first two equations can be combined to yield wave equations for \vec{E} and \vec{B} in time domain:

$$\begin{aligned} \left(\vec{\nabla}^2 - \frac{1}{c^2} \frac{\partial^2}{\partial t^2} \right) \vec{E}(\vec{r}, t) &= 0 \\ \left(\vec{\nabla}^2 - \frac{1}{c^2} \frac{\partial^2}{\partial t^2} \right) \vec{B}(\vec{r}, t) &= 0, \end{aligned} \quad (2.9)$$

with the speed of light in the medium $c(\omega_0) = \frac{1}{\sqrt{\varepsilon_0 \mu_0 \varepsilon(\omega_0) \mu(\omega_0)}} = \frac{c_0}{n(\omega_0)}$.

Here, we have introduced the refractive index of the material $n(\omega_0) = \sqrt{\varepsilon(\omega_0)\mu(\omega_0)}$. The solutions to the wave equations can therefore be found by using a plane-wave ansatz

$$\begin{aligned}\vec{E}(\vec{r}, t) &= \vec{E}_0 e^{i(\vec{k}\cdot\vec{r} - \omega_0 t)} \\ \vec{B}(\vec{r}, t) &= \vec{B}_0 e^{i(\vec{k}\cdot\vec{r} - \omega_0 t)},\end{aligned}\tag{2.10}$$

yielding the dispersion

$$\omega = \frac{c_0 |\vec{k}|}{n(\omega)},\tag{2.11}$$

from which group and phase velocity, $c_{\text{gr}} = \frac{\partial\omega}{\partial k}$ and $c_{\text{ph}} = \frac{\omega}{k}$ respectively, can be calculated if $n(\omega)$ is known. In passing, I have introduced the wave vector \vec{k} that gives the direction of propagation of a plane wave. In fact, in anisotropic media, the direction of energy flow, given by the Poynting vector $\vec{S} = \vec{E} \times \vec{H}$, may not be parallel to that of the wave vector. As mentioned previously, however, I will limit the discussion in this section to isotropic media.

With the solution of the wave equations and Maxwell's equations in media at hand, we will examine what happens with plane waves at the interface of two half-spaces, each with different material properties. This allows us to introduce the Fresnel coefficients for reflection and transmission. Taking the squared moduli of these coefficients will subsequently yield the reflectance and transmittance, observables we have to rely on in many optical experiments.

We consider one half-space from which the plane wave is originating with material properties n_1 , ε_1 , and μ_1 . Correspondingly, we will call the material properties of the second half-space n_2 , ε_2 , and μ_2 . With the use of Maxwell's equations, we can determine the angles of the reflected and the transmitted waves, θ_r and θ_t , respectively, in dependence on the incident angle θ_i :

$$\theta_r = \theta_i \quad \sin \theta_t = \frac{n_1}{n_2} \sin \theta_i.\tag{2.12}$$

In all cases, θ denotes the angle between the normal of the interface and the wave vector \vec{k} . These results could, in principal, also easily be obtained *via*

calculus of variation. Exploiting Maxwell's equations further, we can also calculate the reflected and transmitted fields [10]. We define the incident, reflected and transmitted electric fields as

$$\begin{aligned}\vec{E}_i(\vec{r}, t) &= \vec{E}_{0i} e^{i(\vec{k}_i \vec{r} - \omega t)} \\ \vec{E}_r(\vec{r}, t) &= \vec{E}_{0r} e^{i(\vec{k}_r \vec{r} - \omega t)} \\ \vec{E}_t(\vec{r}, t) &= \vec{E}_{0t} e^{i(\vec{k}_t \vec{r} - \omega t)},\end{aligned}\tag{2.13}$$

respectively. A full discussion of polarized light will follow in Section 2.3. Nevertheless, we will distinguish between two polarizations here already, namely s- and p-polarization. For the former, the incident electric field vector \vec{E}_{0i} is perpendicular to the plane defined by \vec{k}_i and \vec{k}_r . The index s is inspired by the German word for perpendicular: *senkrecht*.

In order to calculate the complex reflection and transmission coefficients, respectively, the reflected or transmitted field is divided by the incident field. Exploiting Maxwell's equations at the interface, this yields:

$$\begin{aligned}r_s &= \left(\frac{\vec{E}_{0r}}{\vec{E}_{0i}} \right)_s = \frac{Z_2 \cos \theta_i - Z_1 \cos \theta_t}{Z_2 \cos \theta_i + Z_1 \cos \theta_t} \\ t_s &= \left(\frac{\vec{E}_{0t}}{\vec{E}_{0i}} \right)_s = \frac{2Z_2 \cos \theta_i}{Z_1 \cos \theta_i + Z_2 \cos \theta_t}.\end{aligned}\tag{2.14}$$

Here, we have introduced the impedance of the medium $Z_j = \sqrt{\frac{\mu_0 \mu_j}{\epsilon_0 \epsilon_j}}$.

For p-polarization, in contrast to s-polarization, the electric field vector \vec{E}_{0i} lies within the plane defined by k_i and k_r . Similarly to above, we get:

$$\begin{aligned}r_p &= \left(\frac{\vec{E}_{0r}}{\vec{E}_{0i}} \right)_p = \frac{Z_1 \cos \theta_i - Z_2 \cos \theta_t}{Z_1 \cos \theta_i + Z_2 \cos \theta_t} \\ t_p &= \left(\frac{\vec{E}_{0t}}{\vec{E}_{0i}} \right)_p = \frac{2Z_2 \cos \theta_i}{Z_1 \cos \theta_t + Z_2 \cos \theta_i}.\end{aligned}\tag{2.15}$$

For normal incidence, *i. e.*, where $\theta_i = 0$, the reflection and transmission coefficients for s- and p-polarization are trivially equal. The squared moduli of the complex Fresnel coefficients yield the real reflectance R and transmittance T :

$$R = |r|^2 \quad \text{and} \quad T = |t|^2 \frac{n_2 \cos \theta_t}{n_1 \cos \theta_i}\tag{2.16}$$

with $T + R = 1$.

2.2 DISPERSION IN NATURAL MATERIALS

In the previous section, we have introduced the macroscopic version of Maxwell's equations and with that the electric permittivity $\varepsilon(\omega)$ and magnetic permeability $\mu(\omega)$. In almost all natural materials, one can set $\mu = 1$ at optical frequencies. Metamaterials, on the other hand, can exhibit effective material parameters with $\mu \neq 1$, as we will discuss in Section 2.6. Nevertheless, here we will focus on the electric permittivity and discuss two types of natural materials and their corresponding dispersion models.

LORENTZ MODEL

First, we take a look at the case of dielectrics, *i. e.*, materials with locally bound electrons. The driving electric field exerts a force on the electrons, causing a displacement and thus a dipole moment. Displacements of the atom nuclei can be neglected due to the much higher mass. The equation of motion for each electron is then given by

$$m \frac{d^2x}{dt^2} + m\gamma \frac{dx}{dt} + m\omega_0^2 x = -e E_0 e^{-i\omega t}, \quad (2.17)$$

where we have set the direction of \vec{E} along the x -axis, e the electronic charge, m the mass of the driven charge, ω_0 the resonance frequency, and γ the damping [10]. The dipole density N of the induced dipole moments $\vec{p} = e\vec{x}$ leads to a macroscopic polarization

$$\vec{P} = \varepsilon_0 \chi_e \vec{E} = \varepsilon_0 \frac{N e^2}{\varepsilon_0 m \omega_0^2} \frac{\omega_0^2}{\omega_0^2 - \omega^2 - i\gamma\omega} \vec{E}. \quad (2.18)$$

The complex electric permittivity can then be calculated as $\varepsilon(\omega) = 1 + \chi_e(\omega)$ and yields:

$$\begin{aligned} \Re(\varepsilon(\omega)) &= 1 + \frac{N e^2}{\varepsilon_0 m} \frac{\omega_0^2 - \omega^2}{(\omega_0^2 - \omega^2)^2 + \gamma^2 \omega^2} \\ \Im(\varepsilon(\omega)) &= \frac{N e^2}{\varepsilon_0 m} \frac{\gamma \omega}{(\omega_0^2 - \omega^2)^2 + \gamma^2 \omega^2}. \end{aligned} \quad (2.19)$$

The imaginary part $\Im(\varepsilon(\omega))$ has a characteristic Lorentzian distribution centered at the resonance frequency ω_0 . We will see similar resonant behavior for the effective material parameters of metamaterials in Section 2.6.

DRUDE MODEL

In contrast to the previously discussed Lorentz Model, applicable for dielectrics where electrons are bound to the atom nuclei, I will now discuss conductive materials. This includes metals and semiconductors – media with free electric charges. Contrary to dielectrics, there is no restoring force, collisions with the stationary atom nuclei, however, lead to damping. The equation of motion is therefore similar, but lacks the restoring force term:

$$m \frac{d^2x}{dt^2} + m\gamma \frac{dx}{dt} = -e E_0 e^{-i\omega t}, \quad (2.20)$$

where γ denotes the collision frequency which is dependent on the Fermi velocity and the mean free path of the free charges [11]. The electric permittivity results in

$$\varepsilon(\omega) = 1 - \frac{\omega_p^2}{\omega^2 + i\gamma\omega}. \quad (2.21)$$

Furthermore, we have introduced the plasma frequency

$$\omega_p = \sqrt{\frac{N e^2}{m \varepsilon_0}}. \quad (2.22)$$

We rewrite the permittivity, separating real and imaginary part, to

$$\varepsilon(\omega) = 1 - \frac{\omega_p^2}{\omega^2 + \gamma^2} + i \frac{\gamma \omega_p^2}{\omega(\omega^2 + \gamma^2)}. \quad (2.23)$$

Neglecting losses, we note that for frequencies below the plasma frequency, $\omega < \omega_p$, the electric permittivity is negative. As we continue to assume $\mu = 1$, this yields an imaginary refractive index $n = \sqrt{\varepsilon}$. As a result, we obtain an evanescent field inside such materials and no propagating wave.

2.3 POLARIZATION AND JONES FORMALISM

In the previous section I have discussed electromagnetic waves and their propagation in media. Furthermore, we have introduced the complex Fresnel coefficients for reflection and transmission at an interface. In that context, we have already discussed the concept of polarization in passing, distinguishing between s- and p-polarization. In this section, we will elaborate on different polarizations and will also introduce the Jones calculus.

As we have already seen in equation 2.10, the solution to the electric wave equation is given by:

$$\vec{E}(\vec{r}, t) = \vec{E}_0 e^{i(\vec{k}\vec{r} - \omega t)}. \quad (2.24)$$

Using Maxwell's equations, we can easily find that the vector \vec{E}_0 is perpendicular to the direction of propagation:

$$\vec{E}_0 \perp \vec{k}. \quad (2.25)$$

Without loss of generality, we define $\vec{k} = |\vec{k}| \hat{e}_z$. We can then rewrite \vec{E}_0 as $\vec{E}_0 = E_{0x} \hat{e}_x + E_{0y} \hat{e}_y$. The complex coefficients $E_{0x} = |E_{0x}| \exp(i\varphi_x)$ and $E_{0y} = |E_{0y}| \exp(i\varphi_y)$, however, can be chosen arbitrarily and define the state of polarization. Depending on the ratio of the moduli $|E_{0y}|/|E_{0x}|$ and the phase difference $\varphi = \varphi_y - \varphi_x$, three general cases are possible.

LINEAR POLARIZATION ($\varphi = 0$ OR $\varphi = \pi$)

I have already briefly discussed this case in Section 2.1 in the form of s- and p-polarization. These terms are, however, of no use under normal incidence. We define linear polarization more generally by a vanishing phase difference between E_{0x} and E_{0y} . For any point in space, we can then write the electric field as

$$\vec{E} = \begin{pmatrix} |E_{0x}| \\ |E_{0y}| \\ 0 \end{pmatrix} e^{-i\omega t} e^{i\varphi}, \quad (2.26)$$

where φ is an arbitrary phase. The electric field will therefore always be parallel or anti-parallel to a fixed direction which is defined by $|E_{0x}|$ and

$|E_{0y}|$, thus the name linear polarization.

CIRCULAR POLARIZATION ($\varphi = \pm \frac{\pi}{2}$, $|E_{0x}| = |E_{0y}|$)

Similar to above, we choose any point in space. We can then write the electric field as

$$\vec{E} = \begin{pmatrix} 1 \\ \pm i \\ 0 \end{pmatrix} |E_{0x}| e^{-i\omega t} e^{i\phi}, \quad (2.27)$$

where ϕ is again an arbitrary phase. Let us now compare the real parts of the x - and y -component of \vec{E} :

$$\begin{aligned} \Re(E_x(t)) &= +|E_{0x}| \cos(\omega t) \\ \Re(E_y(t)) &= \pm |E_{0x}| \sin(\omega t). \end{aligned} \quad (2.28)$$

At any point in space, the electric field describes a circle over time with radius $|E_{0x}|$, thus the name circular polarization. Furthermore, if we instead take a fixed point in time and set

$$\vec{r} = \begin{pmatrix} 0 \\ 0 \\ z \end{pmatrix} \quad \text{and} \quad \vec{k} = \begin{pmatrix} 0 \\ 0 \\ k \end{pmatrix}, \quad (2.29)$$

we obtain

$$\begin{aligned} \Re(E_x(z)) &= +|E_{0x}| \cos(kz + \phi) \\ \Re(E_y(z)) &= \mp |E_{0x}| \sin(kz + \phi), \end{aligned} \quad (2.30)$$

where ϕ is again an arbitrary phase. The real part of the electric field describes a helix along the z -axis, that is either left-handed (+) or right-handed (−), depending on the sign of the phase shift ϕ . We will therefore call these two polarizations *left-circular polarization* (LCP) and *right-circular polarization* (RCP), respectively. One must take care, as this nomenclature varies in literature. Here, we follow the convention of Reference [9].

Both linearly and circularly polarized light are illustrated in Figure 2.1. For right-circularly polarized light, as depicted in (b), it is crucial to note the

different sense of rotation (right-handed) of the electric field in space along the z -axis $\vec{E}(z, t=0)$ in contrast to the sense of rotation (left-handed) of the electric field over time at a fixed point $\vec{E}(z=0, t)$. This often leads to confusion in the definition of right-handed and left-handed polarization.

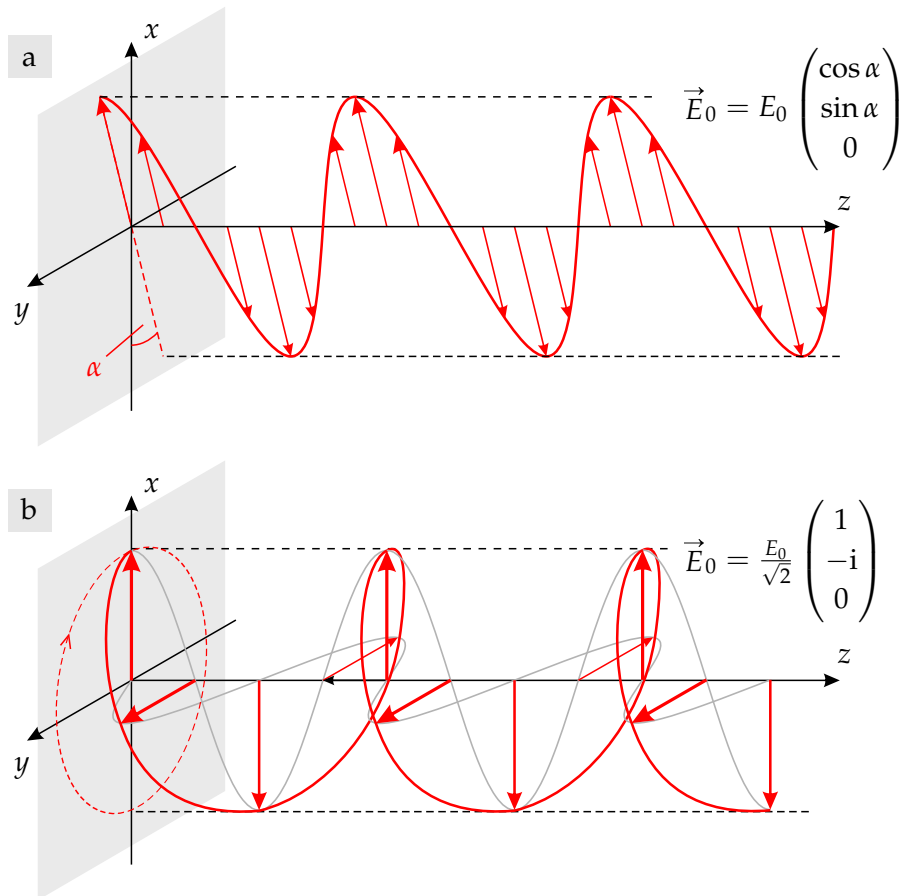


Figure 2.1: Linear polarization (a) and right-handed circular polarization (b) are depicted for a fixed point in time. In both cases the wave vector is in the positive z -direction.

ELLIPTICAL POLARIZATION

In any other case where \vec{E}_0 fulfills neither the requirements for linear, nor for circular polarization, as discussed above, the plane wave is elliptically polarized. At a given point in space the real part of the electric field vector then describes an ellipse over time.

JONES FORMALISM

Under normal incidence onto a plane interface, the wave vectors of the transmitted and reflected waves will be parallel and respectively anti-parallel to the incident wave vector. In these instances, the polarization of the plane waves can be described much more easily with the Jones formalism. As we have seen in the preceding paragraphs, the z -component of the electric field vector can be set to zero if an appropriate coordinate system is chosen where \hat{e}_z is parallel or anti-parallel to the wave vector \vec{k} . We will now extend this approach by dropping the z -component of the electric field in our notation altogether. The polarization will be described by a complex, two-dimensional vector called the Jones vector \vec{J} that lies within the plane normal to the direction of propagation:

$$\vec{J} = \begin{pmatrix} E_1 \\ E_2 \end{pmatrix} = E_1 \hat{e}_1 + E_2 \hat{e}_2. \quad (2.31)$$

The two normalized base vectors can in principle be chosen arbitrarily, but two orthonormal bases are most commonly used: linear and circular polarization. In the former case, any two orthonormal, real polarization vectors form such a basis. We will call these vectors \vec{x} and \vec{y} . Any other Jones polarization vector is then described by a superposition:

$$\vec{J}^{\text{lin}} = \begin{pmatrix} E_1 \\ E_2 \end{pmatrix} = E_1 \vec{x} + E_2 \vec{y}. \quad (2.32)$$

We can now represent linear polarization with an arbitrary angle α to \vec{x} as

$$\vec{J}_\alpha^{\text{lin}} = \begin{pmatrix} \cos \alpha \\ \sin \alpha \end{pmatrix} \quad (2.33)$$

and left-circular polarization and right-circular polarization as

$$\vec{J}_{\text{LCP}} = \frac{1}{\sqrt{2}} \begin{pmatrix} 1 \\ i \end{pmatrix} \quad \text{and} \quad \vec{J}_{\text{RCP}} = \frac{1}{\sqrt{2}} \begin{pmatrix} 1 \\ -i \end{pmatrix}, \quad (2.34)$$

respectively. In this thesis, circularly polarized light plays a central theme and representation of the polarization in a linear polarization basis is thus far from optimal. Note that the vectors \vec{J}_{LCP} and \vec{J}_{RCP} in fact are also orthonormal and can also be used to form a basis which we will call circular-polarization basis, correspondingly:

$$\vec{J}^{\text{circ}} = \begin{pmatrix} E_{\text{L}} \\ E_{\text{R}} \end{pmatrix} = E_{\text{L}} \hat{e}_{\text{LCP}} + E_{\text{R}} \hat{e}_{\text{RCP}}. \quad (2.35)$$

In order to switch from linear to circular-polarization basis or vice versa, we introduce the basis-change matrix

$$\vec{S} = \frac{1}{\sqrt{2}} \begin{pmatrix} 1 & -i \\ 1 & i \end{pmatrix}. \quad (2.36)$$

We can now also carry out polarization operations by matrix multiplication. A linear polarizer in linear polarization basis can thus easily be defined as

$$\vec{M} = \begin{pmatrix} 1 & 0 \\ 0 & 0 \end{pmatrix}. \quad (2.37)$$

To obtain corresponding polarization operations in circular-polarization basis \vec{M}^{circ} , we simply carry out a basis transformation:

$$\vec{M}^{\text{circ}} = \vec{S} \vec{M} \vec{S}^{-1}. \quad (2.38)$$

The total transmission \vec{t} of a system can easily be calculated by mere matrix multiplication of the individual components

$$\vec{t} = \vec{t}_N \cdot \vec{t}_{N-1} \cdot \dots \cdot \vec{t}_2 \cdot \vec{t}_1, \quad (2.39)$$

where \vec{t}_i denotes the transmission matrix of the i th component in the order of propagation. The total reflection matrix \vec{r} can be calculated accordingly.

We will exploit reciprocity and symmetry in the subsequent sections in order to eliminate some of the coefficients of the Jones matrices. In general,

however, the four coefficients of the overall transmission or reflection matrix are different, finite, and complex:

$$\vec{t} = \begin{pmatrix} t_{xx} & t_{xy} \\ t_{yx} & t_{yy} \end{pmatrix} \quad \vec{r} = \begin{pmatrix} r_{xx} & r_{xy} \\ r_{yx} & r_{yy} \end{pmatrix}. \quad (2.40)$$

In linear-polarization basis, the diagonal elements t_{xx} and t_{yy} describe the polarization-conserving transmittances, while t_{yx} and t_{xy} denote the conversion from x -polarized light to y -polarized light and vice versa. The Jones matrices in circular-polarization basis can be written in dependence of the linear coefficients by using Equation 2.38:

$$\begin{aligned} \vec{t}^{\text{circ}} &= \begin{pmatrix} t_{LL} & t_{LR} \\ t_{RL} & t_{RR} \end{pmatrix} \\ &= \begin{pmatrix} (t_{xx} + t_{yy}) + i(t_{xy} - t_{yx}) & (t_{xx} - t_{yy}) - i(t_{xy} + t_{yx}) \\ (t_{xx} - t_{yy}) + i(t_{xy} + t_{yx}) & (t_{xx} + t_{yy}) - i(t_{xy} - t_{yx}) \end{pmatrix} \end{aligned} \quad (2.41)$$

$$\begin{aligned} \vec{r}^{\text{circ}} &= \begin{pmatrix} r_{RL} & r_{RR} \\ r_{LL} & r_{LR} \end{pmatrix} \\ &= \begin{pmatrix} (r_{xx} + r_{yy}) + i(r_{xy} - r_{yx}) & (r_{xx} - r_{yy}) - i(r_{xy} + r_{yx}) \\ (r_{xx} - r_{yy}) + i(r_{xy} + r_{yx}) & (r_{xx} + r_{yy}) - i(r_{xy} - r_{yx}) \end{pmatrix}. \end{aligned} \quad (2.42)$$

Note that the diagonal elements of the reflection matrix in circular-polarization basis surprisingly denote the normal reflectance from LCP to RCP and respectively from RCP to LCP. The reason for this lies in the fact that the linear polarizations are unchanged, but the direction of propagation is changed. The coordinate system therefore changes from a normal right-handed to a left-handed one. Nevertheless, these are the normal reflectances, while the off-diagonal elements, *i. e.*, reflection from LCP to LCP and RCP to RCP, denote polarization conversions. This can be understood intuitively by recalling that for the normal reflectances, the phase shift between x - and y -polarized light must be conserved. The changed direction of propagation changes the coordinate system but not the phase shift in time or space.

The most important polarization states as well as a selection of polarization operations are displayed in Table 2.1.

Table 2.1: Some of the most important polarization states are shown in the upper part of the table, both in linear- and circular-polarization basis. In the lower part of the table, the Jones matrices of three commonly used polarization elements are shown. Arbitrary phase factors have been neglected in all cases.

	Linear Basis	Circular Basis
Linear polarization parallel to \vec{x}	$\begin{pmatrix} 1 \\ 0 \end{pmatrix}$	$\frac{1}{\sqrt{2}} \begin{pmatrix} 1 \\ +1 \end{pmatrix}$
Linear polarization parallel to \vec{y}	$\begin{pmatrix} 0 \\ 1 \end{pmatrix}$	$\frac{1}{\sqrt{2}} \begin{pmatrix} 1 \\ -1 \end{pmatrix}$
Linear polarization under angle α	$\begin{pmatrix} \cos \alpha \\ \sin \alpha \end{pmatrix}$	$\frac{1}{\sqrt{2}} \begin{pmatrix} 1 \\ e^{2i\alpha} \end{pmatrix}$
Left-circular polarization	$\frac{1}{\sqrt{2}} \begin{pmatrix} 1 \\ +i \end{pmatrix}$	$\begin{pmatrix} 1 \\ 0 \end{pmatrix}$
Right-circular polarization	$\frac{1}{\sqrt{2}} \begin{pmatrix} 1 \\ -i \end{pmatrix}$	$\begin{pmatrix} 0 \\ 1 \end{pmatrix}$
Linear polarizer for x -polarization	$\begin{pmatrix} 1 & 0 \\ 0 & 0 \end{pmatrix}$	$\frac{1}{2} \begin{pmatrix} 1 & 1 \\ 1 & 1 \end{pmatrix}$
Half-wave plate (45° axis)	$\begin{pmatrix} 0 & 1 \\ 1 & 0 \end{pmatrix}$	$\begin{pmatrix} 0 & -1 \\ 1 & 0 \end{pmatrix}$
Quarter-wave plate (45° axis)	$\frac{1}{\sqrt{2}} \begin{pmatrix} 1 & -i \\ -i & 1 \end{pmatrix}$	$\frac{1}{\sqrt{2}} \begin{pmatrix} 1 & -1 \\ 1 & 1 \end{pmatrix}$

2.4 BIANISOTROPIC MEDIA AND CHIRO-OPTICAL EFFECTS

We will now extend our discussion to the more general case of bianisotropic media, materials we have excluded in Section 2.1. A detailed discussion is given in References [16] and [17], the lines of which we will follow here.

The most general case of a linear medium allows for anisotropic response functions $\overleftrightarrow{\varepsilon} \neq \varepsilon \delta_{ij}$ and $\overleftrightarrow{\mu} \neq \mu \delta_{ij}$. Furthermore, we examine coupling of the electric to the magnetic field components, *i. e.*,

$$\begin{aligned}\vec{D} &= \overleftrightarrow{\varepsilon} \vec{E} + \overleftrightarrow{\zeta} \vec{H} \\ \vec{B} &= \overleftrightarrow{\mu} \vec{H} + \overleftrightarrow{\zeta} \vec{E}.\end{aligned}\tag{2.43}$$

In this case, the tensors $\overleftrightarrow{\varepsilon}$, $\overleftrightarrow{\mu}$, $\overleftrightarrow{\zeta}$, and $\overleftrightarrow{\zeta}$ are 3×3 matrices. A discussion of this very generalized medium is however beyond the scope of this thesis and we will limit ourselves to uniaxial bianisotropic media. A significant reduction in complexity would also be achieved by assuming isotropy of the medium, leading to scalar response functions. This subclass of bianisotropic media is called *biisotropic*. As the results obtained for axial propagation in uniaxial bianisotropic media and biisotropic media are identical, we will focus our discussion on the former.

In the case of uniaxial bianisotropic media, only one direction in space is distinct, while the response functions are invariant under rotation around that axis. By choosing the coordinate system appropriately and setting the z-axis along that direction, without any loss of generality, the off-diagonal elements of the four tensors $\overleftrightarrow{\varepsilon}$, $\overleftrightarrow{\mu}$, $\overleftrightarrow{\zeta}$, and $\overleftrightarrow{\zeta}$ are zero and the tensors take the diagonalized form [16]

$$\begin{aligned}\overleftrightarrow{\varepsilon} &= \begin{pmatrix} \varepsilon_t & 0 & 0 \\ 0 & \varepsilon_t & 0 \\ 0 & 0 & \varepsilon_z \end{pmatrix} & \overleftrightarrow{\mu} &= \begin{pmatrix} \mu_t & 0 & 0 \\ 0 & \mu_t & 0 \\ 0 & 0 & \mu_z \end{pmatrix} \\ \overleftrightarrow{\zeta} &= \begin{pmatrix} \zeta_t & 0 & 0 \\ 0 & \zeta_t & 0 \\ 0 & 0 & \zeta_z \end{pmatrix} & \overleftrightarrow{\zeta} &= \begin{pmatrix} \zeta_t & 0 & 0 \\ 0 & \zeta_t & 0 \\ 0 & 0 & \zeta_z \end{pmatrix}.\end{aligned}\tag{2.44}$$

Inspired by the metamaterial design that we will discuss in the scope of this thesis, we focus on wave propagation along the z-axis. Any two eigenpo-

larizations we choose for $\vec{k} \parallel \hat{e}_z$ must be perpendicular to \hat{e}_z . Therefore, only the transverse components will contribute. We introduce the transverse Tellegen parameter χ_t and transverse chirality parameter κ_t that will allow us to differentiate easily between different subcategories of uniaxial bianisotropic media [16]:

$$\begin{aligned}\tilde{\zeta}_t &= c_0 (\chi_t - i\kappa_t) \\ \zeta_t &= c_0 (\chi_t + i\kappa_t).\end{aligned}\tag{2.45}$$

As the z -components of the tensors have been eliminated, the equations obtained here are identical to those in biisotropic media [17]. The following discussion is therefore valid for both propagation in biisotropic media and axial propagation in uniaxial bianisotropic media. With χ_t and κ_t at hand, we can now discuss three different subclasses of uniaxial bianisotropic media.

NON-RECIPROCAL MEDIA ($\chi_t \neq 0$):

The Tellegen parameter describes the reciprocity or non-reciprocity of the medium. Non-reciprocal effects such as Faraday rotation occur for a non-vanishing χ_t . We will, however, examine only reciprocal materials in the scope of this thesis and will thus not go into further detail here. The term *reciprocity* will be discussed in more detail in Section 2.5.

NORMAL ANISOTROPIC MEDIA ($\chi_t = \kappa_t = 0$):

By setting both χ_t and κ_t to zero, we obtain a linear, anisotropic medium. However, as the z -components ε_z and μ_z do not contribute for axial propagation, we effectively obtain the same results as for an isotropic medium that we have discussed in Section 2.1.

UNIAXIAL CHIRAL MEDIA ($\chi_t = 0, \kappa_t \neq 0$):

Chiral media are of particular interest for interaction with circularly polarized light and we will therefore discuss this subclass of bianisotropic media in more detail. The word *chiral* stems from the Greek word for hand *cheir* ($\chi\epsilon i\rho$).

Similar to the human hand, chiral objects are defined by their lack of mirror symmetry. Therefore, the mirror image cannot be brought into superposition with the original image *via* translation or rotation. The existence of any mirror-symmetry, regardless whether the normal of that mirror plane is perpendicular or parallel to the z-axis, leads to $\kappa_t = 0$ [17].

We will focus not on macroscopic structures like the human hand, but microscopic chiral objects. An intuitive example is an ensemble of very small metal helices of only one handedness [16]. We will imagine a medium that consists of many of these randomly distributed helices, all aligned parallel to the z-axis, thus defining the special axis. If we “zoom out” far enough, we will see a homogeneous, but anisotropic and chiral medium.

Solving for the wave numbers of the eigenpolarizations [16], one obtains

$$k_{\pm} = \frac{\omega}{c_0} (\sqrt{\varepsilon_t \mu_t} \pm \kappa_t), \quad (2.46)$$

where (+) and (−) denote the right- and left-circularly polarized eigenwaves, respectively. Therefore, we can deduce the complex refractive index of these eigenpolarizations:

$$n_{\pm} = \sqrt{\varepsilon_t \mu_t} \pm \kappa_t = n_t \pm \kappa_t. \quad (2.47)$$

In contrast to the refractive index, the impedance is not dependent on the polarization [17]:

$$Z_{\pm} = \sqrt{\frac{\mu_{\pm}}{\varepsilon_{\pm}}} = \sqrt{\frac{\mu_t(1 \pm \kappa_t)}{\varepsilon_t(1 \pm \kappa_t)}} = \sqrt{\frac{\mu_t}{\varepsilon_t}} = Z. \quad (2.48)$$

Therefore, uniaxial bianisotropic media will yield equal reflection for both circular polarizations.

We do, however, expect effects on circularly polarized light for axial propagation due to the difference in the complex refractive index $n_{\pm} = n'_{\pm} + in''_{\pm}$. We will now distinguish between the terms *optical activity* and *circular dichroism*. As the former is based on a difference in the real part of the refractive index and the latter on a difference in the imaginary part, a bianisotropic medium will always exhibit both effects due to Kramers-Kronig relations [15]. Often, however, one effect can be neglected, while the other is dominant.

OPTICAL ACTIVITY ($n'_+ \neq n'_-$):

A difference in the real part of the refractive index leads to a phase shift of one circular polarization with respect to the other. As we have seen in Table 2.1, linearly polarized light under any arbitrary angle α with respect to the x -axis can be represented by a superposition of LCP and RCP with a phase shift of 2α . Thus, a difference in the real part of the refractive index will yield a rotation α_{rot} of the incoming linearly polarized light by

$$\alpha_{\text{rot}} = \frac{\omega d}{2c_0} \Delta n, \quad (2.49)$$

where $\Delta n = n'_+ - n'_-$ denotes the difference in the real parts of the refractive index and d the propagation length in the medium. This principle has in fact been used for a long time when determining the concentration of sugar in solution. Glucose, like many other biologically important molecules, is chiral and only one enantiomer, *i. e.*, mirror-image, is found in nature. Due to the random orientation and distribution of only one enantiomer, the solution can be described as a biisotropic medium. The effect is far from negligible in natural materials. For a saturated aqueous solution of glucose a propagation distance of $d \approx 36$ cm is sufficient to rotate linearly polarized at $\lambda = 589$ nm by 90 degrees [18].

I emphasize at this point, that one must take care not to confuse the principle of optical activity, where the rotation angle α_{rot} is independent of the orientation of the incoming linear polarization, with the operation of a half-wave plate. In the latter case, the change in polarization is due to linear birefringence and the angle of rotation as well as the polarization state depend on the incident linear-polarization orientation.

CIRCULAR DICHROISM ($n''_+ \neq n''_-$):

A difference in the imaginary parts on the other hand leads to a difference in absorption. For a plane wave propagating along the z -direction, we obtain

$$\begin{aligned} \vec{E} &= \vec{E}_{\pm} e^{i(n_{\pm} k_0 z - \omega t)} \\ &= \vec{E}_{\pm} e^{-n''_{\pm} k_0 z} e^{i(n'_{\pm} k_0 z - \omega t)}. \end{aligned} \quad (2.50)$$

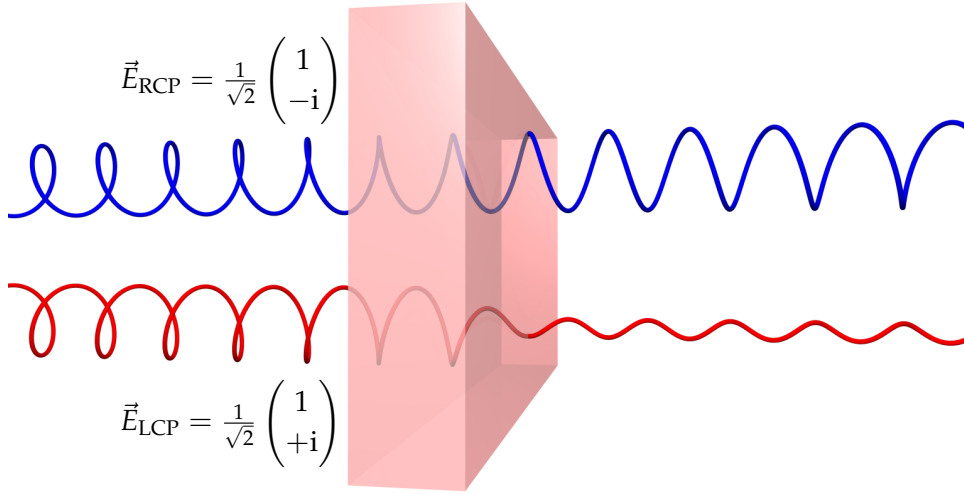


Figure 2.2: Illustration of the effect of circular dichroism. In this case, a fictitious material with $n''_+ > 0$ and $n''_- = 0$ is depicted and therefore only left-circularly polarized light is absorbed during propagation through the material.

We then define the absorption coefficient proportional to the imaginary part of the refractive index

$$\alpha_{\pm} = \frac{2\omega}{c_0} n''_{\pm}, \quad (2.51)$$

yielding the intensity of the circularly polarized plane waves I_{\pm} after propagation over a distance d

$$I_{\pm}(d) = I_0 e^{-\alpha_{\pm} d}, \quad (2.52)$$

where I_0 denotes the incident intensity. The effect is illustrated in Figure 2.2. In contrast to optical activity, circular dichroism is much less pronounced in natural materials.

2.5 RECIPROCITY CONSTRAINTS

In Section 2.3, we have defined the Jones transmission and reflection matrix in their most general form. We will now introduce reciprocity, which allows us to further simplify the Jones matrices. The term reciprocity has its origins in acoustics and has first been introduced by Lorentz in 1896, however in a slightly different form [19]. Even today, the term is used seldomly in text books. Ambivalent and even contradicting definitions found in literature have complicated the conception of the reciprocity principle. We will start our discussion with Lorentz's theorem. Let us assume two vector fields described by \vec{E}_1 and \vec{H}_1 and respectively \vec{E}_2 and \vec{H}_2 . For reciprocal media, *i. e.*, where the Tellegen parameter χ vanishes, Lorentz's theorem states:

$$\int_S (\vec{E}_1 \times \vec{H}_2 - \vec{E}_2 \times \vec{H}_1) \, dS = 0, \quad (2.53)$$

where S denotes an arbitrary closed surface [20]. A more thorough derivation and proof of the general reciprocity definition are beyond the scope of this thesis and for the interested reader I refer to the literature, where a more detailed discussion is given [17, 21]. We will limit ourselves to a discussion of the reciprocity term as it was derived by de Hoop by exploiting Lorentz's theorem shown above [20]. De Hoop showed that reciprocity can be defined *via* scattered fields and their projections for finite-sized scatterers. Figure 2.3 illustrates the situation that we will discuss in the following. We will consider an electric field \vec{E}_1 with wave vector \vec{k}_1 incident on a scatterer of finite size, yielding scattered waves, one of which is in the direction of \vec{k}_2 with field $\overleftrightarrow{M}\vec{E}_1$. \overleftrightarrow{M} denotes a general 3×3 scattering matrix. Similarly, for a wave propagating along $-\vec{k}_2$ with \vec{E}_2 , one will obtain a scattered wave in the direction of $-\vec{k}_1$ with $\overleftrightarrow{M}_r\vec{E}_2$. \overleftrightarrow{M}_r here denotes the scattering matrix for that reverse propagation direction. Note that all polarizations are arbitrary at this point. De Hoop showed that for any reciprocal medium, *i. e.*, where χ vanishes, we obtain:

$$\vec{E}_2 \cdot \overleftrightarrow{M}\vec{E}_1 = \vec{E}_1 \cdot \overleftrightarrow{M}_r\vec{E}_2. \quad (2.54)$$

Because we are still considering general propagation directions and polarizations, the conclusions from this finding are not intuitive at first. De Hoop

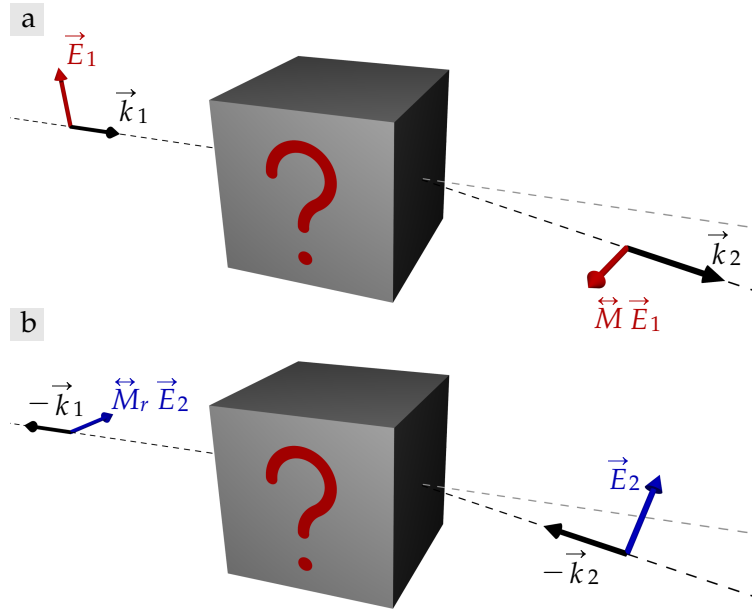


Figure 2.3: Illustration of the model discussed in context of de Hoop's reciprocity: (a) Forward propagation direction: An incident wave with wave vector \vec{k}_1 and field strength \vec{E}_1 is scattered. The field strength of the wave scattered into the direction of \vec{k}_2 is $\vec{M}_r \vec{E}_1$. (b) Reverse propagation direction: An incident wave with wave vector $-\vec{k}_2$ and field strength \vec{E}_2 is scattered. The field strength of the wave scattered into the direction of $-\vec{k}_1$ is $\vec{M}_r \vec{E}_2$.

has shown, that the scattering amplitude for a wave in the direction of \vec{k}_2 and polarized along \vec{E}_2 resulting from an incident wave polarized along \vec{E}_1 with wave vector \vec{k}_1 is equal to the scattering amplitude of a wave in the direction of $-\vec{k}_1$ and polarized along \vec{E}_1 resulting from an incident wave polarized along \vec{E}_2 with wave vector $-\vec{k}_2$ [21].

Similar results were obtained by Born and Wolf. By assuming scalar fields and thus, neglecting different polarizations one obtains

$$f(\vec{k}_1, \vec{k}_2) = f(-\vec{k}_2, -\vec{k}_1), \quad (2.55)$$

where $f(\vec{k}_i, \vec{k}_s)$ denotes the scattering amplitude for a wave incident with wave vector \vec{k}_i and scattered into a direction \vec{k}_s [22]. As the state of polarization is a central theme in this thesis, we will follow the more general form of reciprocity as stated by de Hoop.

We will now simplify the discussion significantly by considering solely plane waves of normal incidence onto a slab of a reciprocal medium. The only scattered waves that have to be considered in the following are therefore the reflected ($\vec{k}_2 = -\vec{k}_1$) and the transmitted ($\vec{k}_2 = \vec{k}_1$) waves. This allows us to discuss reciprocity in the Jones formalism, which we will exploit extensively in this thesis. By applying de Hoop reciprocity to the Jones formalism one finds

$$\overleftrightarrow{t}_r = \overleftrightarrow{t}^T \quad \text{and} \quad \overleftrightarrow{r}_r = \overleftrightarrow{r}^T, \quad (2.56)$$

where \overleftrightarrow{t} and \overleftrightarrow{r} denote the overall transmission and reflection matrices [23]. Correspondingly, \overleftrightarrow{t}_r and \overleftrightarrow{r}_r are the Jones matrices for reverse propagation and can be calculated by simply taking the transpose. We emphasize that reverse propagation means that the direction of the incident wave vector is set anti-parallel to that of the scattered wave vector. While in the case of transmission, where $\vec{k}_2 = \vec{k}_1$, this corresponds to an incident wave from the opposing direction, in the case of reflection we obtain

$$-\vec{k}_2 = \vec{k}_1. \quad (2.57)$$

As reverse propagation therefore denotes incidence on the identical system, the reflection matrices in forward and backward propagation direction must be equal, yielding

$$\overleftrightarrow{r} = \overleftrightarrow{r}^T. \quad (2.58)$$

The Jones reflection matrix must thus be symmetric, a finding that will be of importance in the following chapter. As we have mentioned previously, one must be careful when discussing reflection in circular polarization basis, in order not to confuse conversions with polarization-conserving reflectances. In order to circumvent this problem in Jones notation, we simply substitute our findings from a linear-polarization basis, *i. e.*, $r_{yx} = r_{xy}$, into Equation 2.42, which yields

$$r_{RL} = r_{LR}. \quad (2.59)$$

For a reciprocal scatterer the normal reflectances are therefore identical.

2.6 A SHORT INTRODUCTION TO METAMATERIALS

In the previous sections, we have introduced the interaction of electromagnetic waves with natural material through the complex material parameters $\varepsilon(\omega)$ and $\mu(\omega)$. These response functions are defined by the interaction with charges on a microscopic scale. We have seen in Section 2.2 that we obtain very different results for ε depending on the state of these charges, *i. e.*, whether they are bound to the atoms or not. At optical frequencies, dielectrics exhibit electric permittivities with a real part approximately in the range from 1 to 10. Values outside of this range are only observed in close spectral proximity to resonances, where on the other side the imaginary part is strongly increased. In contrast, materials with free charges, *e. g.*, metals, exhibit negative electric permittivities for frequencies below the corresponding plasma frequency ω_p .

By choosing the appropriate material or by mixing two materials, we can find the electric permittivity $\varepsilon(\omega)$ fitting for most applications. Despite the freedom we have in ε , we cannot pick a refractive index n independently from the impedance Z . The reason for this is the magnetic permeability, which can in good conscience be set to $\mu = 1$ at optical frequencies. The induced magnetization can be neglected at these high frequencies and the magnetic susceptibility thus is 0:

$$\vec{M}(\omega) = \chi_m(\omega) \vec{H}(\omega) \approx 0. \quad (2.60)$$

To overcome limitations of normal materials, *metamaterials* have been introduced at the beginning of this millennium [24]. Many different definitions of this term can be found in the literature, some of which emphasize on the aspect of them being “man-made” materials. Others limit the definition to periodic structures with all feature sizes much smaller than the wavelength and here-from resulting effective material parameters. A precise and unambiguous definition of metamaterials is tricky and therefore we will use a very general one in the scope of this thesis. The prefix “meta” stems from the Greek word $\mu\epsilon\tau\alpha$, meaning “beyond” [12]. Metamaterials are thus “beyond” normal materials, either in their constitution, their optical properties, or both.

The first central defining property we require is periodicity. Similar to the

atoms in a crystal, a metamaterial shall consist of a periodic substructure that can be seen as an arrangement of “meta-atoms”. In contrast to normal crystals, not only the constituent materials, but mainly the geometry of these meta-atoms will define the optical properties of our metamaterial. In order to distinguish metamaterials from photonic crystals, we furthermore require the lattice periods of the metamaterial to be smaller than the operating wavelength. This therefore excludes higher diffraction orders from which one would be able to deduce the existence of a periodicity.

If the lattice period is much smaller than the operating wavelength, $a \ll \lambda$, the scale of the inhomogeneities within each unit cell is so small that one can introduce effective parameters ϵ_{eff} and μ_{eff} that accurately describe the response of the metamaterial to an electromagnetic wave. By designing the meta-atom carefully, effective parameters beyond those found in natural materials can be achieved.

A paradigm building block for metamaterials with effective parameters is the split-ring resonator that has appeared in many groundbreaking metamaterial publications [25–30]. As we will see in Chapter 3, the split-ring resonator has also been the inspiration for other more complex metamaterials.

The operation principle is illustrated in Figure 2.4. A split-ring resonator consists, as the name suggests, of a conductive wire loop into which a small gap has been introduced. The split-ring has a capacity C , due to the two open ends, and, because of the finite length of the wire, an inductivity L . An analogous circuit diagram is depicted in Figure 2.4(b). It is the well-known LC circuit, for which the resonance frequency is given by

$$\omega_{\text{LC}} = \sqrt{\frac{1}{LC}}. \quad (2.61)$$

An oscillating current in the wire induces a perpendicularly oriented oscillating magnetic dipole moment and vice versa. The entity of these magnetic dipole moments for an arrangement of many split-ring resonators leads to a macroscopic magnetization \vec{M} . Therefore, if the driving magnetic field has a non-zero component perpendicular to the plane of the split ring, one

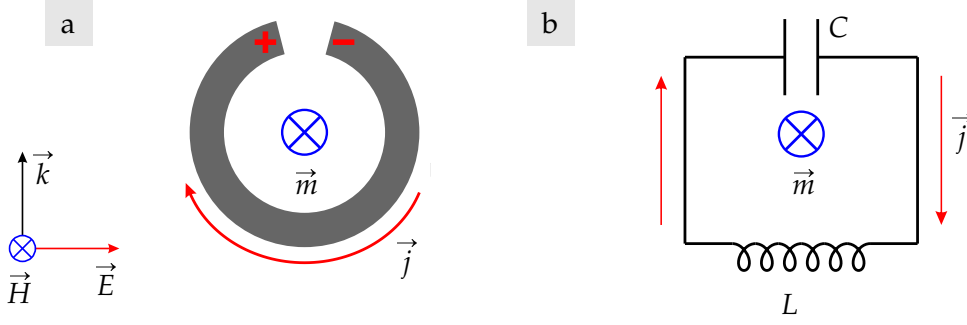


Figure 2.4: (a) Illustration of the operation principle of a split-ring resonator. Both the driving electric field and magnetic field couple to the split-ring resonator by inducing an oscillating current and an oscillating magnetic dipole moment, respectively. (b) An analogue circuit diagram for the split-ring resonator, assigning a capacity C to the two open ends and an inductivity L to the wire loop.

observes resonant coupling to the external magnetic field:

$$\vec{M} = \chi_m \vec{H}. \quad (2.62)$$

For the magnetic permeability we obtain [28]

$$\mu_{\text{eff}}(\omega) = 1 + \frac{F \omega^2}{\omega_{\text{LC}}^2 - \omega^2 - i\gamma\omega}. \quad (2.63)$$

F denotes the filling fraction of the unit cell and γ the damping which is due to Ohmic and radiative losses. Additionally, the driving electric field also couples to the split-ring resonator in the configuration shown in Figure 2.4(a), leading to electric dipole moments and the effective electric permittivity

$$\varepsilon_{\text{eff}}(\omega) = 1 + \frac{A \cdot F}{\omega_{\text{LC}}^2 - \omega^2 - i\gamma\omega}. \quad (2.64)$$

The parameter A depends on the geometrical parameters of the split-ring resonator. One should note that in the discussed configuration above, the split-ring will in fact also exhibit bianisotropy [28].

For operation at optical or near-infrared frequencies, fabrication is challenging as noble-metal structures with feature sizes below 100 nm have to be created. Electron-beam lithography (EBL) combined with subsequent

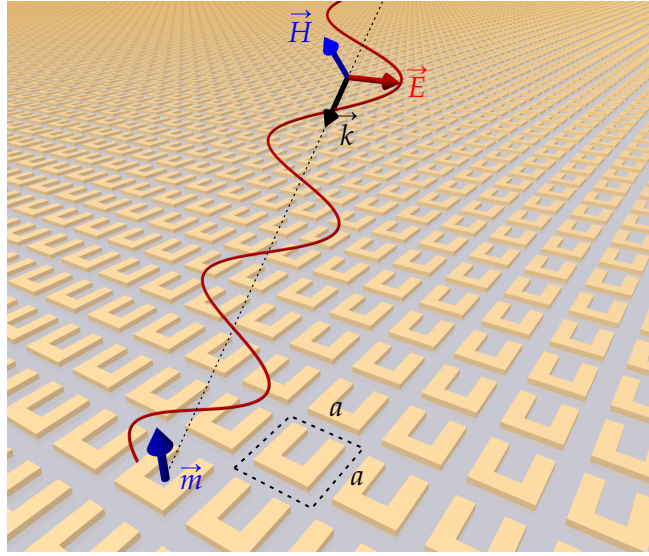


Figure 2.5: Artistic illustration of a two-dimensional metamaterial design based on split-ring resonators with lattice period a . Under oblique incidence, as depicted, magneto-electric coupling is observed.

metal evaporation and lift-off procedures offers the necessary resolution but can only deliver two-dimensional structures. Therefore, periodicity is only possible within the plane of the split-ring resonator. Such an EBL-compatible split-ring resonator design is depicted in Figure 2.5. As seen above, magnetic coupling to split-ring resonators is only possible, if the driving magnetic field is not in the plane of the resonator. For this metamaterial design, this would be the case under normal incidence. For oblique incidence as depicted here, on the other hand, magnetic coupling is observed.

Over the past decade, many other metamaterial designs have been introduced and experimentally realized [31]. Fish-net and cut-wire pair designs have allowed for magnetic coupling under normal incidence. By stacking multiple layers of two-dimensional designs, more complex, bulk-like metamaterials have been achieved. The realization of fully three-dimensional metamaterial designs, however, remains a challenge [32].

Nevertheless, the ability to tailor the material parameters of metamaterials has inspired many new applications. One of the most frequently discussed applications in the context of metamaterials is perfect lensing [33]. The idea is based on the possibility of achieving a negative refractive index, which is the case when both the effective electric permittivity ϵ_{eff} and the effective

magnetic permeability μ_{eff} are negative:

$$n_{\text{eff}} = \sqrt{\varepsilon_{\text{eff}} \mu_{\text{eff}}} < 0 \quad \text{if} \quad \varepsilon_{\text{eff}} < 0 \quad \text{and} \quad \mu_{\text{eff}} < 0. \quad (2.65)$$

A number of different metamaterial designs with a negative refractive index have been proposed and also experimentally achieved [34–38]. As this is only possible at resonance though, losses will not be negligible and operation is limited to narrow bandwidths.

Another growing application has been the idea of cloaking objects, *i. e.*, making them invisible [39]. Corresponding theoretical concepts were first introduced in 2006 [40, 41]. As Maxwell’s equations are form-invariant under coordinate transformations, it is possible to map a virtual transformation onto a realizable spatial distribution of $\vec{\varepsilon}(x, y, z)$ and $\vec{\mu}(x, y, z)$. Note that in general, both ε and μ need to be anisotropic and inhomogeneous. Successful cloaking has thus only been achieved at microwave frequencies with narrowband operation [42]. Broadband operation has been demonstrated for designs of reduced complexity [43–45] or in diffuse optics where the characteristic propagation speed is far below the vacuum speed of light [46].

In the scope of this thesis, we will not consider the effective material parameters of metamaterials $\vec{\varepsilon}_{\text{eff}}$ and $\vec{\mu}_{\text{eff}}$, but rather focus on chiral metamaterials. These designs are characterized by their lack of mirror-symmetries and thus

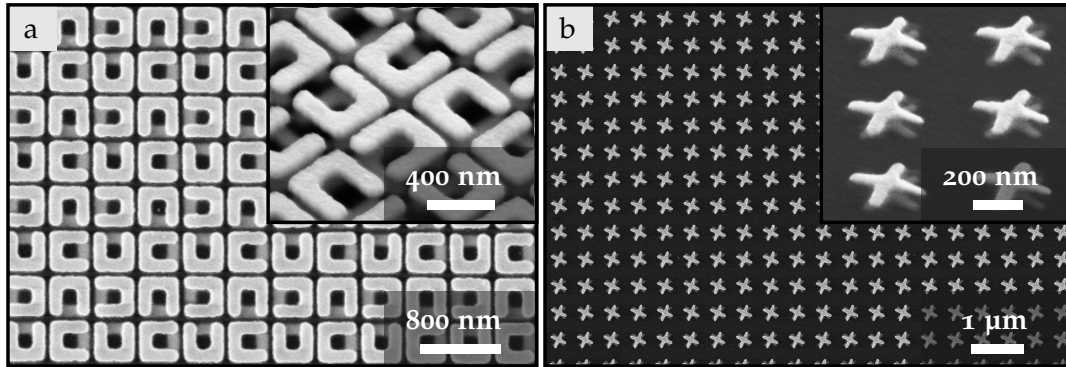


Figure 2.6: Scanning electron micrographs of two examples for chiral metamaterials. (a) Two layers of differently oriented split-ring resonators (adapted with permission from Reference [47]). (b) Two layers of twisted crosses (adapted with permission from Reference [48]).

exhibit strong chiro-optical effects like circular dichroism or optical activity, similar to uniaxial bianisotropic media. In contrast to natural materials, however, where these effects are normally very small, they can be many orders of magnitude larger in chiral metamaterials. Chiral metamaterials have on one side been proposed to be an alternative route to negative refractive indexes [49], but more importantly could offer efficient and broadband control of circularly-polarized light. Furthermore, the scalability of metamaterials could bring circular-polarization optics to frequency regimes that have previously been difficult to access. Many designs have been proposed and fabricated over the past decade, most of them based on the principle of stacking multiple two-dimensional layers with different orientations [47, 48, 50–55]. Two examples are depicted in Figure 2.6. While the observed chiro-optical effects are much larger than those found in any natural material, their operation bandwidth is usually very small. In the next chapter we will therefore discuss helical metamaterials, a class of chiral metamaterials with broadband operation capabilities.

3

Chapter 3

THEORY OF HELICAL METAMATERIALS



Illustration of N -helical metamaterials with $N = 4$ and $N = 3$.

In this chapter, I will introduce the concept of helical metamaterials and discuss their principle of operation. I will then point out the existence of performance-diminishing circular-polarization conversions that are inherent to the conventional helical metamaterial design due to linear birefringence.

To solve this dilemma N -helical metamaterials have been introduced. I will give a very general theoretical analysis based on symmetry and reciprocity, proving that the elimination of circular-polarization conversions causes a fundamentally different principle of operation. This analysis will be followed by a discussion of N -helical metamaterials and corresponding numerical calculations. I will also point out certain geometrical optimizations that significantly improve polarizer performance.

Finally, I will discuss another helical-metamaterial design, serving as a broadband circular-polarization converter and exhibiting strong, broadband asymmetric polarization conversions.

3.1 CONVENTIONAL HELICAL METAMATERIALS

In the previous chapter I have already briefly introduced the concept of chiral metamaterials, *i. e.*, metamaterials that exhibit chiro-optical effects that are many orders of magnitude larger than in natural materials. Naturally, this inspires applications as a circular polarizers that have long relied on a combinations of linear polarizers and retardation wave plates. Many different chiral metamaterial designs have been proposed and realized experimentally over the past decade [7]. The majority of these designs is based on stacking multiple achiral layers with varying lateral orientation or composition [27, 47, 48, 51, 53, 56]. Operation of most of these designs, however, is based on single resonances, therefore yielding only small bandwidths. The same disadvantage holds true for chiral photonic crystals [57–61]. Metamaterials based on periodic arrays of metal helices allow for very strong extinction of one circular polarization over a large bandwidth as we will see in this section.

The word *helix* stems from the Greek word $\epsilon\lambda\iota\zeta$ meaning “twisted” or “curved” [62]. Mathematically, a helix can be described by a three-dimensional parametric function

$$\vec{r}(t) = \begin{pmatrix} r_H \sin(2\pi t) \\ \pm r_H \cos(2\pi t) \\ Ht \end{pmatrix}, \quad t \in [0, N_p]. \quad (3.1)$$

In this instance, the axis of the helix has been chosen along the z -axis. The parameters r_H , H , and N_p denote the helix radius, axial pitch, and number of pitches, respectively. We will continue to use this notation in the following chapters. The choice of sign yields either a left-handed (+) or a right-handed (−) helix.

Helices appear in many instances in nature and everyday life. Screws and springs are of helical geometry, for example. Spiral staircases have allowed for space-efficient construction for centuries. Filaments in a conventional light bulb are in fact formed by a helical path around which the actual wire describes an additional helix. This so-called coiled coil leads to a wire length that is orders of magnitude larger than the actual size of the filament and, thus, increases the efficiency. In biology, an entire group of

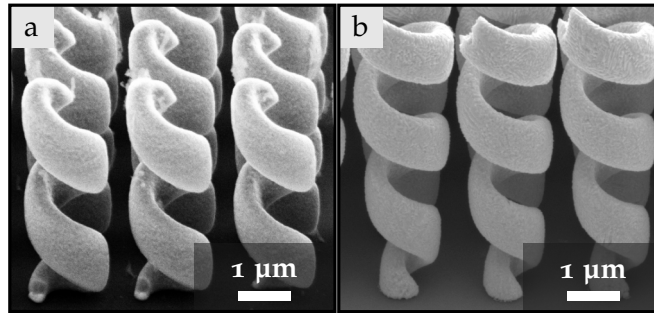


Figure 3.1: Scanning electron micrographs of two examples for helical metamaterials. (a) Conventional helical metamaterial based on gold helices and fabricated *via* direct laser writing and subsequent electro-chemical gold deposition (adapted with permission from Reference [8]). (b) Improved helical-metamaterial design based on tapered gold helices (adapted with permission from Reference [63])

molecules, helicenes, are named on the basis of their helical geometry. An even more famous example is the double-helix geometry of deoxyribonucleic acid (DNA), where two helices with a mutual axis are intertwined. Early on, helical structures have also appeared in purely theoretical discussions of chiral bianisotropic media as we have seen in Section 2.4.

Here, I will concentrate on helical metamaterials, *i. e.*, periodic arrays of metallic helical structures. These were the very first chiral metamaterial design to exhibit both a large operation bandwidth and at the same time pronounced extinction for one circular polarization, making them ideal as broadband circular polarizers. Helical metamaterials can thus be seen as the analogue to the common wire-grid polarizer for linear polarization. Scanning electron micrographs in Figure 3.1 depict two possible helical-metamaterial designs.

The unit-cell sizes that I consider are not much smaller than the operating wavelength and I will therefore refrain from considering effective parameters. I will, however, consider only wavelengths that are smaller than the lateral lattice period a , thus eliminating higher diffraction orders entirely from the discussion.

In this first section I review the operation principle of conventional helical metamaterials as they have been proposed and experimentally demonstrated

for the first time in 2009 [8]. I do so by considering numerically calculated spectra for which I have employed the commercial software package CST Microwave Studio and the therein implemented time-domain solver. In a first step, the complex components of the linear Jones matrices in transmission and reflection were calculated. From here, exploiting Equation 2.41, we can calculate the corresponding Jones matrices in circular-polarization basis. The underlying substrate has been neglected in these calculations as it only contributes to small spectral shifts, but not to any qualitative changes. Furthermore, I only consider the total transmittance for each circular polarization in this section, not discriminating between different resulting polarizations. These total transmittances are given by

$$\begin{aligned} T_{\text{LCP}} &= |t_{\text{LL}}|^2 + |t_{\text{RL}}|^2 \\ T_{\text{RCP}} &= |t_{\text{LR}}|^2 + |t_{\text{RR}}|^2, \end{aligned} \quad (3.2)$$

where t_{ij} denotes the complex entries of the Jones transmission matrix in circular-polarization basis. The constituent metal is assumed to be gold modeled by Drude parameters $\omega_p = 1.37 \cdot 10^{16} \text{ s}^{-1}$ and $\gamma = 1.2 \cdot 10^{14} \text{ s}^{-1}$. Here, as well as in the following sections, I will use a set of standard geometrical parameters with a lattice period of $a = 1 \mu\text{m}$, a helix radius of $r_H = 300 \text{ nm}$, a wire radius of $r_W = 50 \text{ nm}$, and where it applies an axial pitch of $H = 1 \mu\text{m}$.

In order to understand the basic principle of operation, we first consider the split-ring resonator that I have introduced in Section 2.6. A unit cell with a single split-ring resonator is of course achiral, as there exists a plane of mirror symmetry, even in the presence of a substrate. Such a unit cell and the corresponding spectra are depicted in Figure 3.2(a). Under normal incidence, the transmittances for left-circularly polarized light (LCP) and right-circularly polarized light (RCP) are therefore identical.

Two distinct resonances can be identified, corresponding to an “electric” and “magnetic” mode for linearly-polarized light [25]. Note that under oblique incidence so-called extrinsic chirality occurs for certain azimuthal angles [64]. I will limit our discussion in this entire thesis to normal incidence and, thus, the intrinsic chirality of the structures discussed.

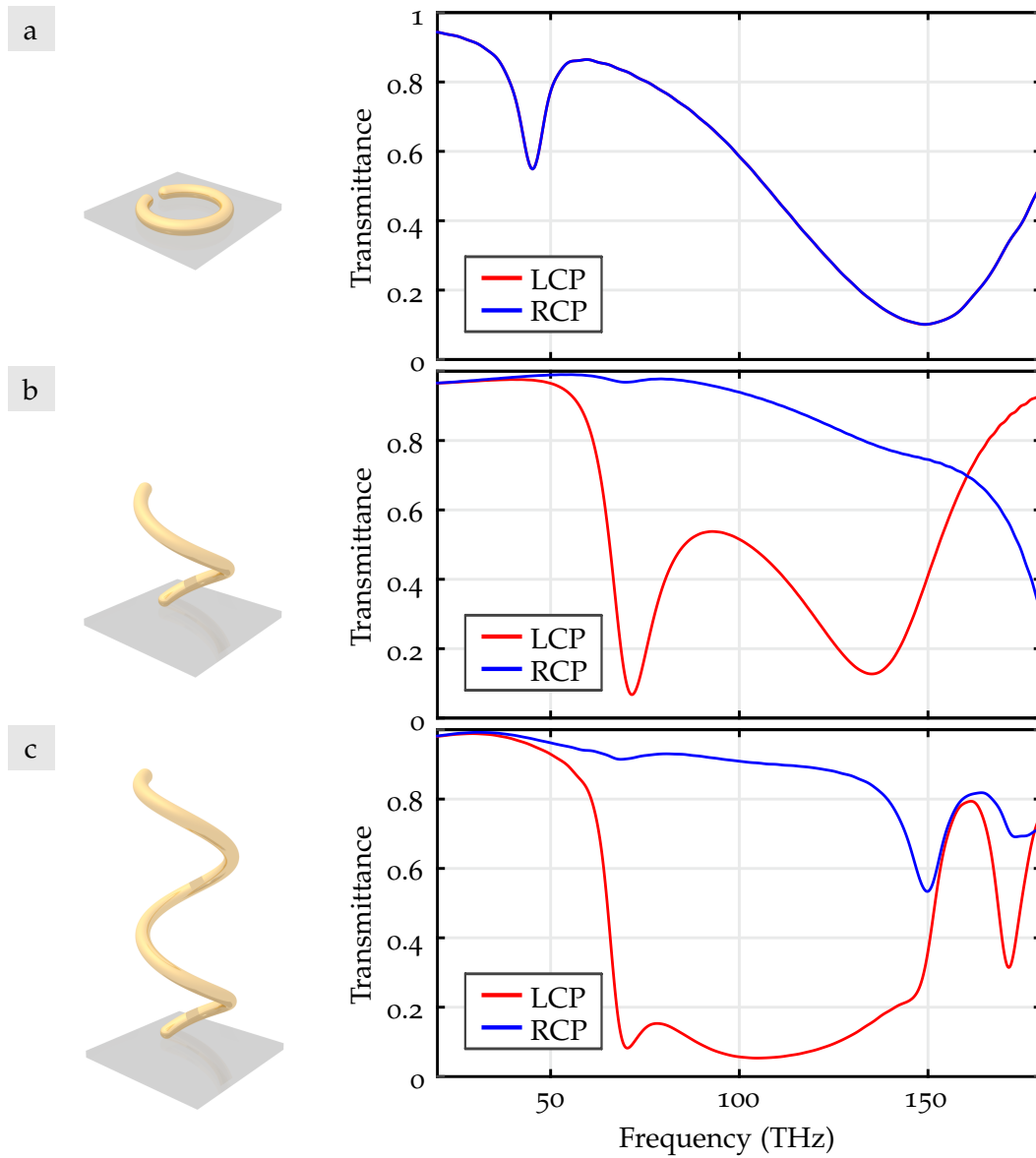


Figure 3.2: Numerically calculated transmittance spectra for both circular polarizations are transmitted for three cases. In (a) the achiral split-ring resonator yields no difference for RCP and LCP and therefore only one line with two distinct resonances is visible. (b) By pulling one end of the split-ring resonator up in space one creates a helix that exhibits a large difference between LCP and RCP. (c) By increasing the number of pitches a broad polarization band forms with a bandwidth of approximately one octave.

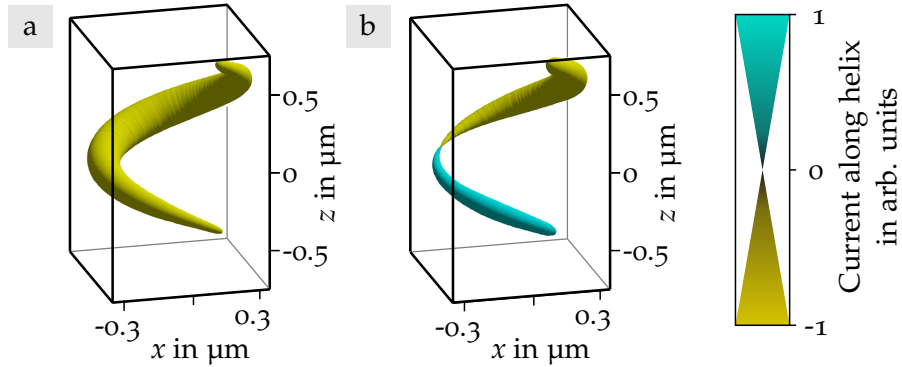


Figure 3.3: Calculated current densities along the helix wire under incidence of left-circular polarization are illustrated. Two frequencies are depicted: the left panel shows the current density at 70 THz and the right panel at 140 THz. The color indicates the sign of the current for this fixed moment in time, while the thickness indicates the magnitude.

We now create a helical structure, by taking the left open end of the splitting resonator in Figure 3.2(a) and move it up in space. This left-handed helix has approximately one pitch, depending on the size of the gap of the split-ring resonator. As the mirror-symmetry is now broken, this unit cell is chiral. Figure 3.2(b) illustrates the unit cell together with the corresponding transmittance spectra. In contrast to the split-ring resonator spectra, the transmittances for LCP and RCP are considerably different. Circularly polarized light with matching handedness, *i.e.*, LCP for this left-handed helix, couples to this helix, induces a current, and is reflected. Similar to the spectra in (a), two distinct resonances are observed, corresponding to the fundamental and first harmonic mode, *i.e.*, induced current distributions with no nodes and one node, respectively. We have calculated these current distributions, using the commercial software package COMSOL Multiphysics, at the resonance frequencies $f_0 = 70$ THz and $f_1 = 140$ THz under normal incidence of left-circular polarization. In Figure 3.3 the results are depicted. Coupling of right-circularly polarized light, on the other hand, is much less pronounced (not shown here) leading to high transmittance for RCP.

Figure 3.2(c) furthermore demonstrates that by increasing the number of pitches to merely two, a broad polarization band with a bandwidth of more than one octave is achieved. In all instances where I discuss the bandwidth,

I will refer to the relative bandwidth in octaves defined by

$$B = \log_2 \left(\frac{f_{\max}}{f_{\min}} \right), \quad (3.3)$$

where f_{\max} and f_{\min} denote the high- and low-frequency end of the operation band, respectively. This broad operation band originates from the superposition of different modes, for which the number of nodes in the current distribution increases with increasing frequency [8]. To illustrate this, we have calculated the current distribution again, however, at a frequency of $f = 100$ THz, where for a helix with only one pitch, coupling is weak. The left panel in Figure 3.4 clearly shows that under normal incidence of left-circular polarization a mode with two current nodes is excited. This mode cannot be excited for a helix of only one pitch, due to the boundary conditions given by the ends of the helix wire. When right-circular polarization is incident on this left-handed helix coupling is much less pronounced and the currents are much lower as can be seen in the panel on the right.

For a more detailed discussion, I have plotted the moduli of the individual Jones transmission and reflection matrices for a single-helix unit cell with one pitch in Figure 3.5. Furthermore, to examine the effect of losses, we have carried out additional calculations, where the constituent metal of the helix was modeled as a perfect electric conductor (PEC). The results of are shown in the left panels. As the lateral lattice period is smaller than the wavelength, no higher diffraction orders other than the zeroth orders exist. Therefore, without losses any light that is blocked from transmission is reflected. As expected from Equation 2.59, the normal reflectances $|r_{\text{RL}}|^2$ and $|r_{\text{LR}}|^2$ are identical. The difference in transmission is therefore based on a difference between $|r_{\text{LL}}|^2$ and $|r_{\text{RR}}|^2$, the polarization conversions in reflection. In particular the conversion $|r_{\text{LL}}|^2$ reaches values of up to 95%.

Conversions are also not negligible in transmission where $|t_{\text{RL}}|^2$ and $|t_{\text{LR}}|^2$ reach values of approximately 10%. For a polarizer application these conversions are unwanted, as they will yield the undesired circular polarization, even when only the desired polarization is incident. As we have neglected the substrate in our calculations, our sample is invariant under inversion of direction of propagation. Therefore, the Jones transmission matrix will

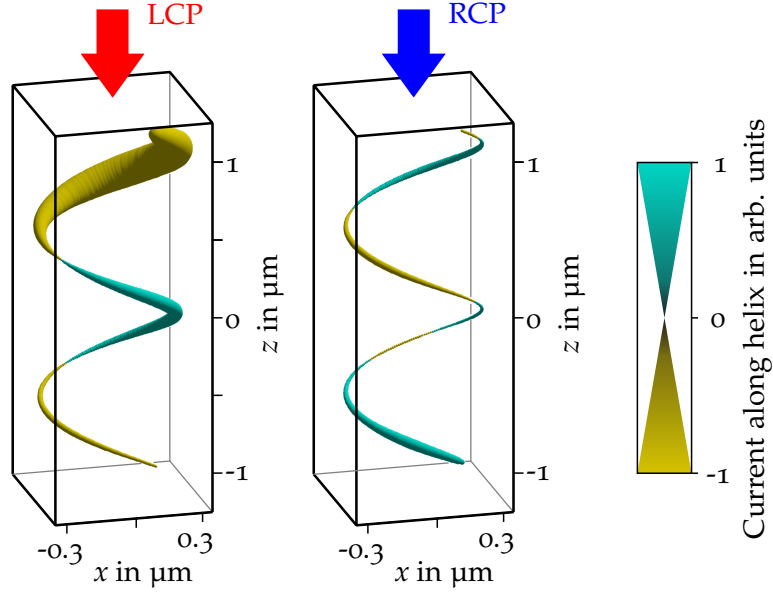


Figure 3.4: In analogy to Figure 3.3, calculated current densities along the helix wire are shown, here for a frequency of 100 THz. Both incident circular polarizations, *i. e.*, LCP and RCP are shown in the left and in the right panel, respectively. The color indicates the sign of the current for this fixed moment in time, while the thickness indicates the magnitude.

be symmetric (see Equation 2.56). In general, however, these conversions will not be identical, especially in the presence of a substrate. While optimized geometrical parameters might lead to slightly decreased conversions in transmission, they cannot be fully eliminated for conventional helical metamaterials as I will discuss in the next section. Such optimized geometrical parameters have been discussed for conventional helical metamaterials in detail through numerical calculations [65, 66].

From the right panels it becomes clear that losses lead to minor quantitative changes, but are neither improving, nor hindering the performance of the metamaterial significantly. We will see in the following section that this can be fundamentally different for more complex helical metamaterials.

Instead of only varying geometrical parameters, more complex helical metamaterial designs lead to even further improved performance. When searching for such an improved design that yields a larger bandwidth or a higher extinction ratio $\frac{T_{\text{RCP}}}{T_{\text{LCP}}}$, nature delivers one inspiring and prominent

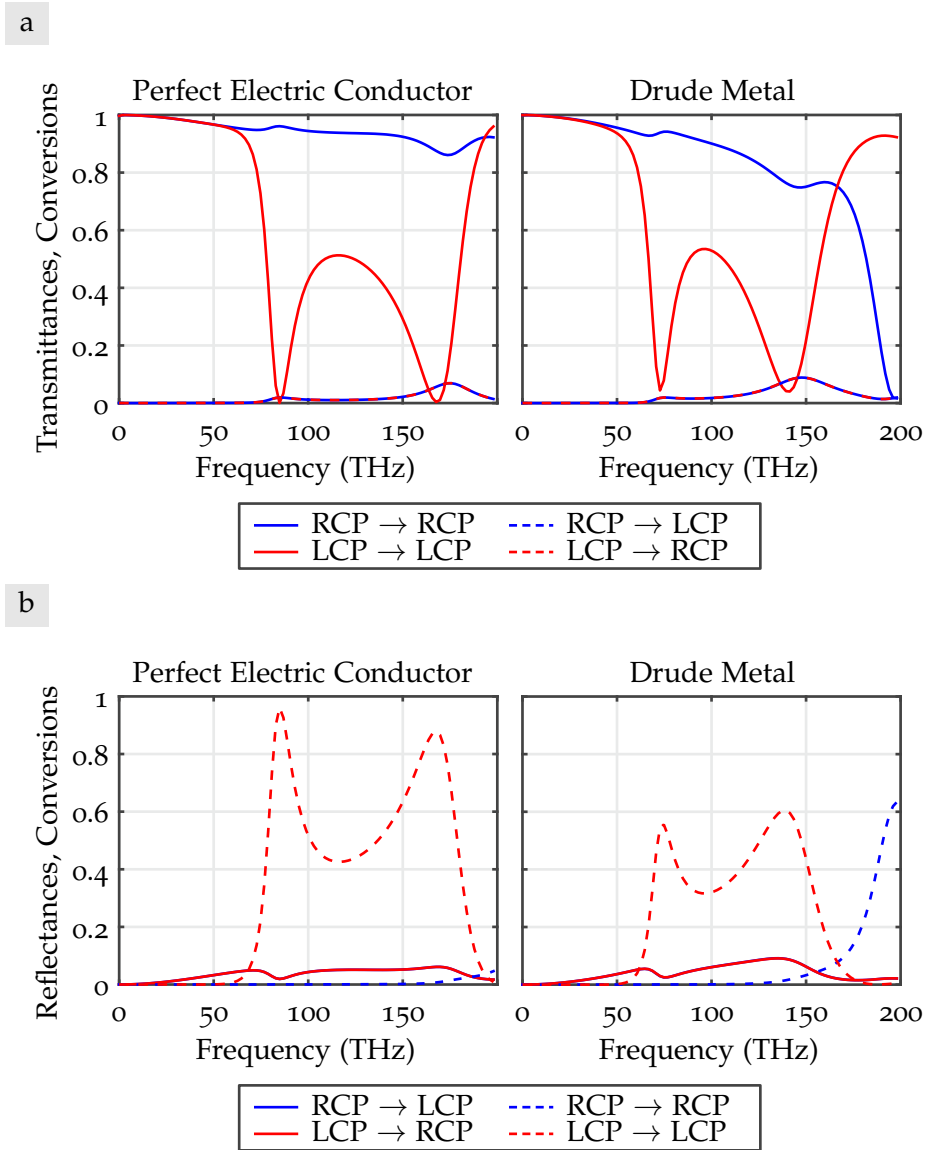


Figure 3.5: (a) The squared moduli of the individual entries of the Jones transmission matrix are depicted for the lossless case modeled by a perfect electric conductor (left panel) and for finite losses modeled by a Drude metal (right panel). The solid lines denote the normal transmittances and the dashed lines denote polarization conversions. (b) In analogy to (a), the squared moduli of the Jones reflection matrix are depicted.

example, namely the DNA double helix. By intertwining two helices within one unit cell, Yang *et al.* showed numerically that the performance of helical metamaterials based on gold or aluminum double helices can be improved considerably [67, 68]. This leads to a strong increase in bandwidth with a slightly decreased average extinction ratio though.

To circumvent this trade-off, a different approach to increase the bandwidth was introduced by Gansel *et al.* where the helix radius was tapered along the helix axis, as depicted in Figure 3.1 [63]. The bandwidth in this design was enlarged to values of approximately 1.5 octaves. At the same time, the extinction ratio was improved. Care must however be taken, as this design is not invariant with regard to the direction of propagation. Due to inherent circular polarization conversions, the transmittance spectra for incoming circular polarization are different depending on the direction from which light impinges, making the design for a certain orientation optimal as either a circular polarizer or a circular-polarization analyzer.

The optimized designs described above, namely intertwining two helices within one unit cell and tapering the helix radius along the helix axis, can be combined to yield a tapered double helix, introduced by Zhao *et al.* [69]. Here, extinction ratio and bandwidth were also improved simultaneously. Nevertheless, all of these designs exhibit circular-polarization conversions, a problem that we will tackle in the next section.

3.2 THEORY OF N-HELICAL METAMATERIALS

In the previous section, I have introduced conventional helical metamaterials that offer high extinction ratios and a large bandwidth. Undesired circular-polarization conversions, however, cannot be fully eliminated. Here, I will discuss a more complex class of helical-metamaterial designs that allows for a complete elimination of these conversions, while at the same time offering strong, broadband circular dichroism [70, 71]. Before we look at numerical calculations, I introduce a symmetry-based analysis that is valid not only for helical metamaterials but for all chiral metamaterials with certain symmetry properties.

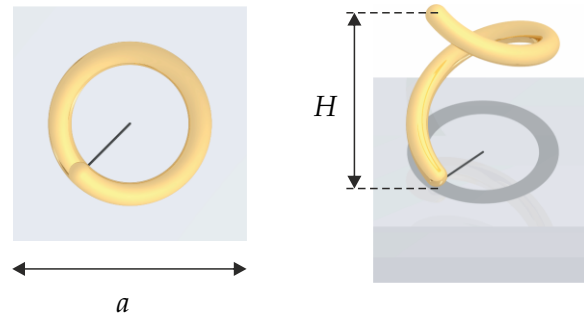


Figure 3.6: Unit cell with a single helix. The rotational symmetry is broken and linear birefringence is introduced, indicated by the small black line, leading to circular-polarization conversions.

Circular-polarization conversions are due to the fact, that the two circular-polarization states are not eigenstates of the system. By taking a closer look at the unit cell which is depicted in Figure 3.6, we can intuitively understand this fact. The end of the helix wire together with the axis or center of the helix define a direction in space that breaks the rotational symmetry and thus introduces linear birefringence, indicated by the thin black line here. Examining Equation 2.41, we see that the off-diagonal elements are caused by linear birefringence, *i. e.*, $t_{xx} \neq t_{yy}$ [72].

Recovering full rotational symmetry is, however, impossible if we want to discuss metamaterials based on periodic arrays. Instead, we show that by recovering any N -fold rotational symmetry, where $N \geq 3$, circular-

polarization conversions are completely eliminated. For this, we require the linear Jones transmission and reflection matrices to be invariant under rotations of $\varphi_N = \frac{2\pi}{N}$. We use the rotation matrix

$$\overleftrightarrow{M}_N = \begin{pmatrix} \cos \varphi_N & -\sin \varphi_N \\ \sin \varphi_N & \cos \varphi_N \end{pmatrix} \quad (3.4)$$

and require N -fold rotational invariance for the Jones transmission matrix

$$\overleftrightarrow{t} = \overleftrightarrow{M}_N \cdot \overleftrightarrow{t} \cdot \overleftrightarrow{M}_N^{-1}. \quad (3.5)$$

Solving this, yields two independent equations:

$$\begin{aligned} (t_{xx} - t_{yy}) \sin^2 \varphi_N + (t_{xy} + t_{yx}) \sin \varphi_N \cos \varphi_N &= 0 & \text{(i)} \\ (t_{xx} - t_{yy}) \sin \varphi_N \cos \varphi_N - (t_{xy} + t_{yx}) \sin^2 \varphi_N &= 0 & \text{(ii)} \end{aligned} \quad (3.6)$$

For $N \in \{1, 2\}$ the solution is trivial and no further knowledge on t_{ij} is gained. On the other side, for any integer N larger than two $\sin \varphi_N$ is not equal to zero. We can therefore divide the first equation by $\tan \varphi_N$ and after adding (i) and (ii), we obtain $t_{xy} = -t_{yx}$. This furthermore yields $t_{xx} = t_{yy}$ and we end up with a simplified Jones matrix [70–72]:

$$\overleftrightarrow{t} = \begin{pmatrix} t_{xx} & t_{xy} \\ -t_{xy} & t_{xx} \end{pmatrix}. \quad (3.7)$$

If \overleftrightarrow{t} is invariant under rotations of $\frac{2\pi}{N}$ for $N \geq 3$, \overleftrightarrow{t} is also invariant under rotations of any other angle. Clearly, linear birefringence has therefore been eliminated. However, we are much more interested in the Jones transmission matrix in circular-polarization basis and thus exploit Equation 2.38, which yields

$$\overleftrightarrow{t}^{\text{circ}} = \begin{pmatrix} t_{xx} + it_{xy} & 0 \\ 0 & t_{xx} - it_{xy} \end{pmatrix}. \quad (3.8)$$

Therefore, I have shown that it is not necessary to recover full rotational symmetry but any N -fold rotational symmetry with $N \geq 3$ will completely eliminate circular-polarization conversions [70, 71, 73]. In the same way, the Jones reflection matrix can be derived. Furthermore, we know that due to

reciprocity (see Equation 2.59) the diagonal elements of the reflection matrix in circular-polarization basis are equal. As the off-diagonal elements have been eliminated, this leaves a reflection matrix that is proportional to the unity matrix:

$$\vec{r}^{\text{circ}} = r_{xx} \begin{pmatrix} 1 & 0 \\ 0 & 1 \end{pmatrix}. \quad (3.9)$$

This is already an important finding, significantly different from what we have seen for conventional helices. Any difference in circular-polarization transmittances must therefore be due to a difference in absorption, as we have also eliminated all conversions and reflectance is equal for both circular polarizations. Furthermore, no higher diffraction orders than the zeroth orders exist, as $\lambda > a$. For lossless media, one would therefore expect absolutely no circular-polarizer effect.

Let us summarize these general findings:

- N -fold rotational symmetry for $N \geq 3$ eliminates all circular-polarization conversions, both in transmission and reflection.
- By further assuming only reciprocal constituent media, one obtains polarization-independent reflectance.
- For lossless media no circular-polarization effect can occur, due to conservation of energy.

Independently of the actual geometry, not only the unit cell must fulfill N -fold rotational symmetry, but the overall structure. As we are considering periodic arrays for which N -fold rotational symmetries with $N = 5, 7, 10, \dots$ do not exist, I will limit the discussion in the following to multiples of $N = 3$ and $N = 4$.

First of all, it is interesting to point out the difference to linear polarizers here. The famous wire-grid polarizer, for example, does not exhibit any linear-polarization conversions. Despite the lack of polarization conversions, both in reflection and in transmission, the undesired linear polarization can be blocked by simply being reflected. Therefore, even without or with negligible losses a high extinction ratio can be achieved. No matter what

we choose as our metamaterial design, the identical principle of operation cannot be achieved with constituent reciprocal materials.

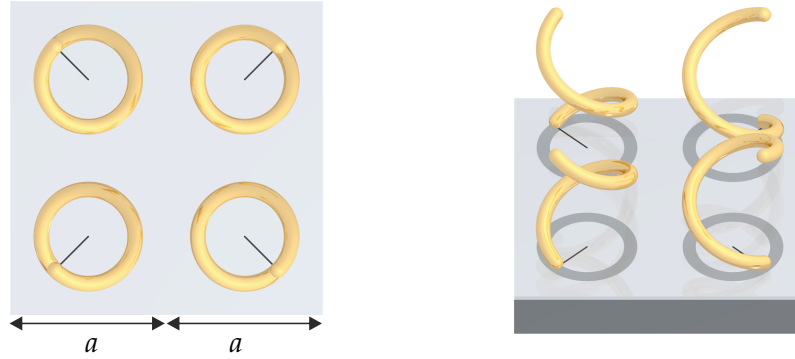


Figure 3.7: Larger unit cell with four individual rotated single helices, thus recovering 4-fold rotational symmetry.

Even though these are general findings that are valid for all chiral-metamaterial designs, I now turn back to helical metamaterials. There is more than one way to recover N -fold rotational symmetry for helical metamaterials. One example is depicted in Figure 3.7 where the lateral size of the unit cell has been double to $2a$ and four helices are respectively rotated by 0, 90, 180, and 270 degrees. The drawback of this design is the increased lattice period that also leads to an increase of minimum wavelength by a factor of two.

Instead, I will discuss unit cells of unchanged lateral sizes in which N helices with one mutual have been intertwined, calling the resulting design N -helical metamaterial [70, 71, 74]. This might seem like a minor modification to conventional helical metamaterials. Due to our symmetry-based analysis, we however expect fundamental differences.

At first we consider $N = 4$, *i. e.*, quadruple helices, in the same quadratic array that I have discussed in the previous section. The corresponding unit cell is depicted in Figure 3.8. We have carried out numerical calculations, corresponding to those for conventional helical metamaterials, again for the cases of a lossless constituent metal, modeled by a perfect electric conductor, and the case of a Drude model for gold with finite losses ($\omega_p = 1.37 \cdot 10^{16} \text{ s}^{-1}$, $\gamma = 2 \cdot 10^{14} \text{ s}^{-1}$). The former case, depicted in the left panels of 3.9, is fun-

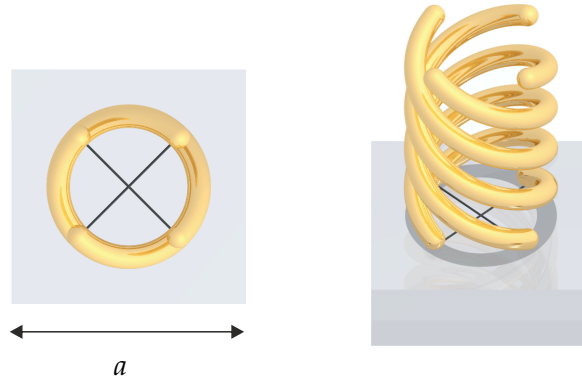


Figure 3.8: $N = 4$ helical-metamaterial design where four helices with a mutual helix axis have been intertwined within one unit cell, thus recovering 4-fold rotational symmetry.

damentally different from conventional helical metamaterials. Conversions have been fully eliminated, both in reflection and in transmission which was the original goal. Furthermore, not only the normal reflectances but also the normal transmittances are equal. The former results from reciprocity and the latter is therefore due to conservation of energy.

Let us consider the more realistic case of a Drude metal with finite losses, depicted in the right panels. Conversions are nevertheless zero as it results solely from N -fold rotational symmetry. Furthermore, the reflection spectra exhibit only minor quantitative differences to the lossless case.

More importantly, circular-polarization transmittances are different and show strong circular dichroism over a large frequency range. Here, the term circular dichroism is appropriate, as the difference in transmittance is due to a difference in absorption, just as I have defined the term in Section 2.4.

In this context, I note that these results are well known and expected for uniaxial bianisotropic and biisotropic media. However, as the operation wavelength is not much larger than the lattice period, one cannot simply apply these results. Our symmetry-based analysis does not assume effective materials and is therefore also valid for wavelengths close to Wood's anomaly.

While certainly much stronger than in natural materials, circular dichroism observed in $N = 4$ helical metamaterials with only one pitch is insufficient

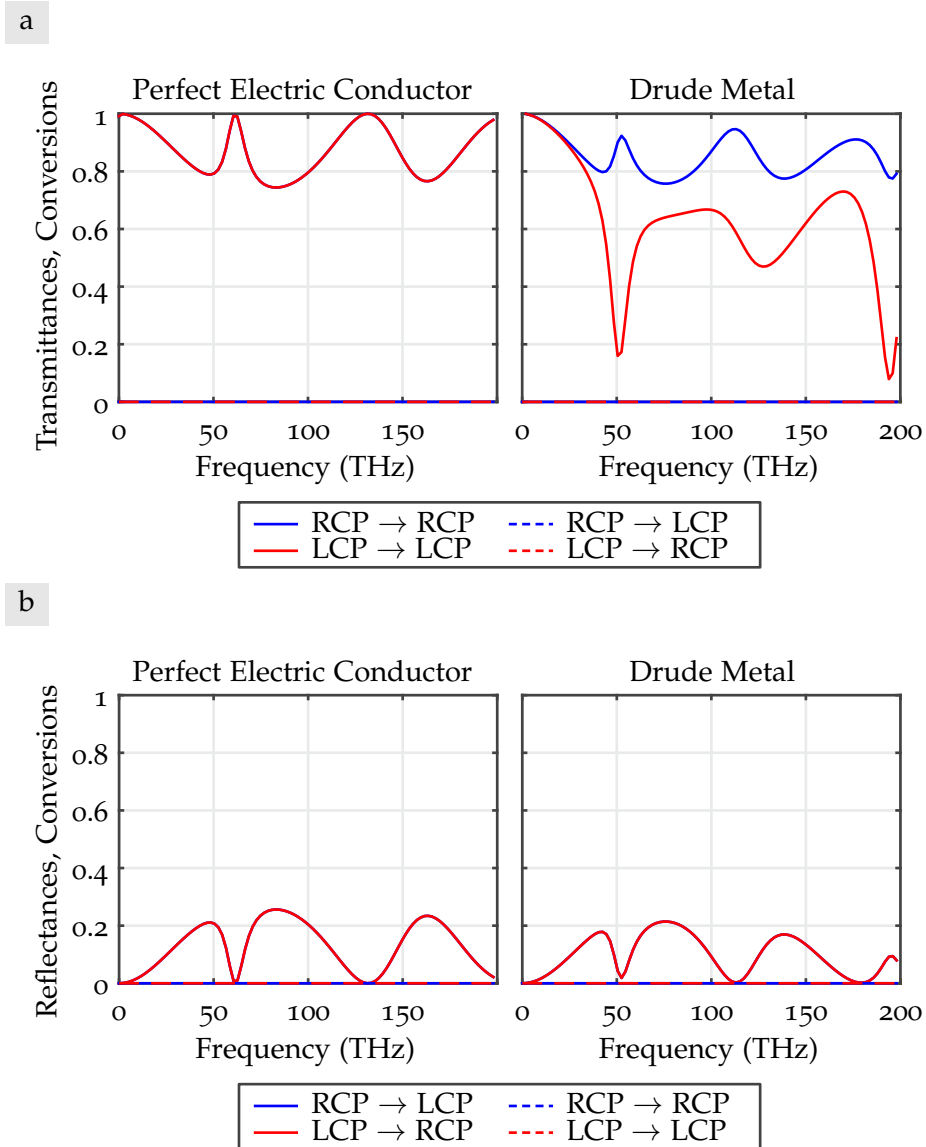


Figure 3.9: In analogy to Figure 3.5, the squared moduli of the Jones transmission (a) and reflection (b) matrix have been plotted. Qualitative differences are visible for the case of a lossless constituent metal as depicted in the left panels in comparison to a Drude metal as shown in the right panels.

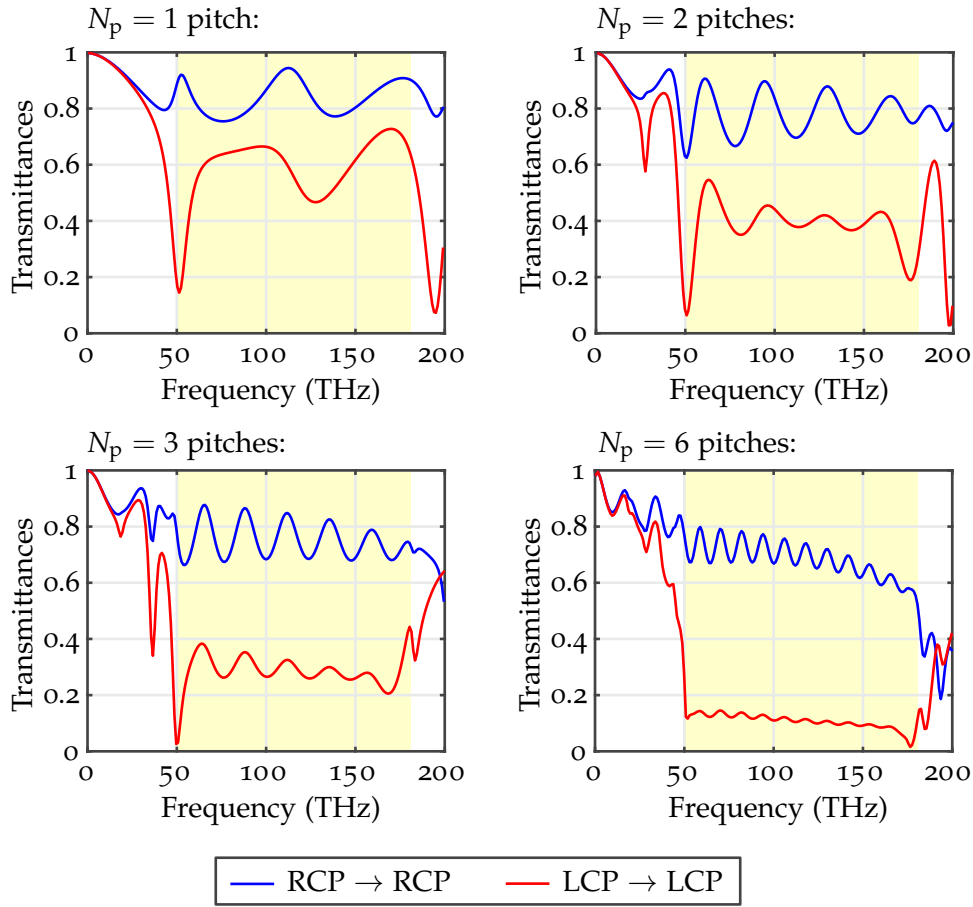


Figure 3.10: The polarization-conserving transmittances are plotted for an increasing number of pitches, *i. e.*, for $N_p = 1$, $N_p = 2$, $N_p = 3$, and $N_p = 6$. The yellow shaded region indicates the polarization band forming for high numbers of pitches. Conversions have been neglected in these plots as they are strictly zero.

for polarizer applications. Similar to the case of conventional helical metamaterials, we slowly increase the number of pitches as depicted in Figure 3.10. Even though the extinction ratio is increased successively, a much larger number of pitches is necessary in order to obtain similar performance. This is expected, as the undesired circular polarization cannot simply be reflected but must be absorbed. For the case of $N_p = 6$ pitches a large extinction is achieved with a bandwidth of 1.8 octaves, indicated by the yellow-shaded

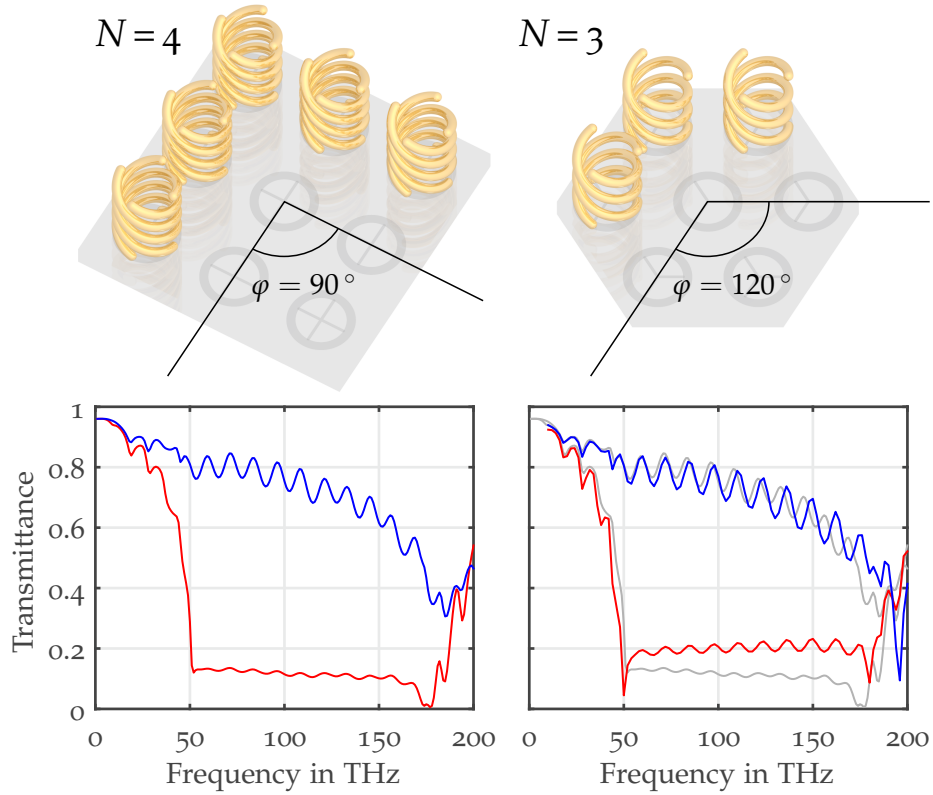


Figure 3.11: Comparison of N -helical metamaterials with $N = 4$ (left panels) and $N = 3$ (right panels). In the latter case an underlying hexagonal lattice is necessary to eliminate circular-polarization conversions. Corresponding numerical calculations depicting the polarization-conserving transmittances are depicted below. In the right diagram the spectra for $N = 4$ have been added as grey lines as guide to eye.

region and unmatched by any other chiral metamaterial.

Before I will discuss geometrical optimizations for N -helical metamaterials in the next section, we first consider the case of $N = 3$ which is the lowest degree of discrete rotational symmetry that fully eliminates circular-polarization conversions. In contrast to $N = 4$, only three helices have to be intertwined within one unit cell, thus facilitating fabrication for operation at visible or near-infrared frequencies considerably. As mentioned previously, the underlying translational lattice must fulfill the same discrete rotational symmetry. Otherwise, the entire system will inherently exhibit linear bire-

fringe and thus circular-polarization conversions again [75]. Therefore, we will consider $N = 3$ helices arranged in a hexagonal lattice, as depicted in Figure 3.11.

For comparison, the case of $N = 4$ is depicted on the left-hand side. Corresponding numerical calculations are depicted below, showing no qualitative changes, especially for the transmittance of RCP (blue line). The extinction ratio for $N = 3$ is slightly lower, which is to be expected, due to the lower filling fraction and thus decreased absorption. Conversions are not shown in the diagrams as they are dead zero, supported by our symmetry arguments.

In conclusion, we have found that we can eliminate undesired circular-polarization conversions with N -helical metamaterials, while at the same time achieving strong and broadband circular dichroism with unmatched bandwidths. However, this is not simply a minor adjustment, but care must be taken as certain limitations apply due to the different principle of operation. More complex unit cells and a much higher number of axial pitches is required to achieve extinction ratios comparable to those of conventional helical metamaterials. In the next section geometrical improvements for $N = 3$ helices will therefore be discussed.

3.3 OPTIMIZING N -HELICAL METAMATERIALS

So far I have discussed the effect of recovering N -fold rotational symmetry and we have seen that while circular-polarization conversions are eliminated, the extinction ratio of N -helical metamaterials is inferior to that of conventional helical metamaterials. Until now I have only discussed one set of standard geometrical parameters that yielded good results for single helices. The question that naturally arises is: can we find different geometrical parameters for N -helical metamaterials? For this we again have considered the case of $N = 3$. The following numerical calculations have been carried out in the scope of a cooperation with the group of S. Burger (Zuse Institute Berlin) using JCMsuite (JCMwave), which is based on a frequency-domain finite-element method [71].

The most crucial geometrical parameter is the helix radius r_H . In the case of conventional helical metamaterials an increasing helix radius has led to both a better extinction ratio and a larger bandwidth [65]. The only downside here was a strong increase of polarization conversions in transmission to values of up to 16%. As circular-polarization conversions are, however, strictly zero for N -helical metamaterials an increasing helix radius should

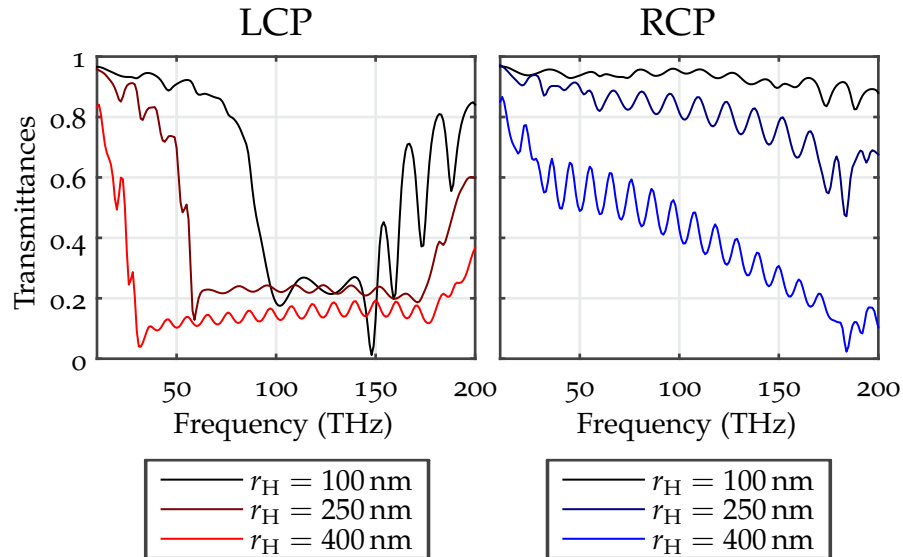


Figure 3.12: Numerically calculated spectra for different helix radii r_H .

intuitively be a win-win situation.

The following calculations have been carried out for the same geometrical parameters as before, however with $N_p = 6$ pitches and varying the helix radius from 100 nm to 400 nm. For a small number of selected values, the transmittance spectra for left-circular (LCP) and right-circular polarization (RCP) are depicted in Figure 3.12.

Let us first examine the case of LCP in the left panel. Here, the bandwidth is strongly increased to previously unmatched values of more than two octaves, spanning across almost the entire mid-infrared spectrum. Additionally, the transmittance is also slightly decreased as desired. When examining the transmittance for RCP on the other hand, we observe a strong decrease here too. Even though a similar behavior was found for conventional helices in Reference [65], it is much more pronounced here. Therefore, increasing the helix radius does not lead to an improved extinction ratio for N -helical metamaterials.

As a variation of the axial pitch or the diameter of the helix wire have much smaller impact on the transmittance spectra, I will not discuss them here in detail. Instead, I consider a geometrical optimization that had also lead to significant improvement in the case of conventional helical metamaterials: tapering the helix radius along the helix axis. In contrast to Reference [63], the radius $r_H(z)$ along the helix axis is increased linearly:

$$r_H(z) = (r_2 - r_1) \frac{z}{N_p H} + r_1. \quad (3.10)$$

We keep r_1 fixed at 100 nm, the minimum value that I have previously discussed for non-tapered triple-helices, and introduce the taper ratio $\eta = \frac{r_2}{r_1}$:

$$r_H(z) = (\eta - 1) \frac{z r_1}{N_p H} + r_1. \quad (3.11)$$

For selected values of η , the corresponding transmittance spectra are depicted in Figure 3.13. By increasing the taper ratio η similar bandwidths are achieved as before for the largest radius in the non-tapered case. This strongly suggests that the bandwidth is governed mainly by the maximum radius, rather than the radius function $r_H(z)$.

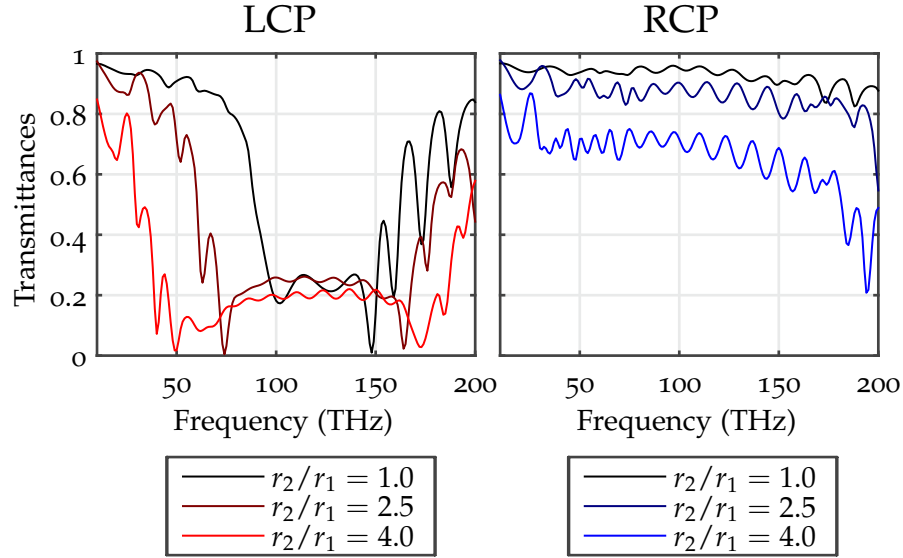


Figure 3.13: Numerically calculated spectra for tapered helices with different taper ratios r_2/r_1 .

In order to analyze the results more quantitatively, I have first normalized the transmittance of LCP to that of RCP and have then fitted a box function to extract a value for the relative bandwidth for operation. Furthermore, the transmittances were averaged inside that frequency range. The ratio of the two averaged transmittances then yields the extinction ratio $\frac{\langle T_{\text{RCP}} \rangle}{\langle T_{\text{LCP}} \rangle}$. These extracted values are plotted in Figure 3.14 for the non-tapered case on the left-hand side and for the tapered case on the right-hand side. In the non-tapered case, the bandwidth increase to values of up to 2.7, but the extinction ratio shows now significant enhancement for larger helix radii. On the contrary, in the tapered case the increasing taper ratio leads to an enhancement simultaneously for the extinction ratio and the bandwidth. Note, that the opening angle of the depicted tapered triple-helix is strongly exaggerated. All calculations have been carried out for $N_p = 6$ pitches. The maximum taper ratio therefore corresponds only to an opening angle of 2.9° .

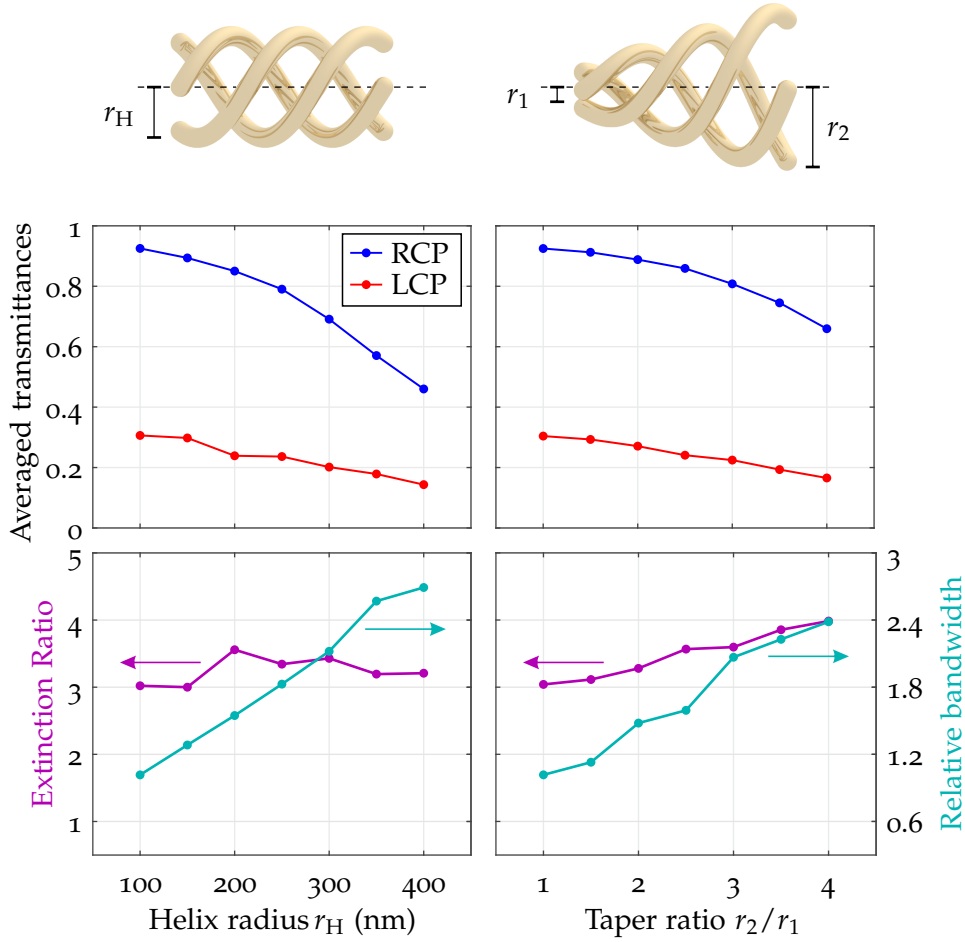


Figure 3.14: A summary of extracted values for the case of non-tapered (left panels) and tapered helices (right panels) are shown. In the upper diagrams, the corresponding averaged transmittances are shown in dependence of the helix radius or the taper ratio, respectively. Below, extinction ratio (purple) and the relative bandwidth (turquoise) are shown.

Finally, I will briefly discuss the effect of an increasing number of pitches N_p . Neglecting reflections and boundary effects and, thus, assuming only the effect of bulk absorption, one would expect the square of the transmittance when the number of pitches is increased by a factor of two. To examine this, we compare transmittance spectra for $N_p = 12$ and $\eta = 4$ to the squared previously calculated spectra ($N_p = 6$). The original calculation with $N_p = 6$ is depicted in black and our simple approximation is shown by the grey

dashed line. The numerical calculation for the case of $N_p = 12$ is depicted by a red and a blue line, respectively for LCP and RCP. Clearly, especially for LCP the calculation is in very good agreement with the approximation. In the case of RCP, however, the approximation yields lower transmittances. This is due to the additional reflectances in the approximation that are not present for a bulk. Note that this really is only a rough estimation as we have kept the taper ratio constant, but have increased the number of pitches and have therefore also varied the opening angle of the taper. As I have discussed before, however, especially the bandwidth is mainly governed by the maximum radius along the tapered helix. This is well reproduced, seeing that the bandwidth remains nearly the same when doubling the number of pitches.

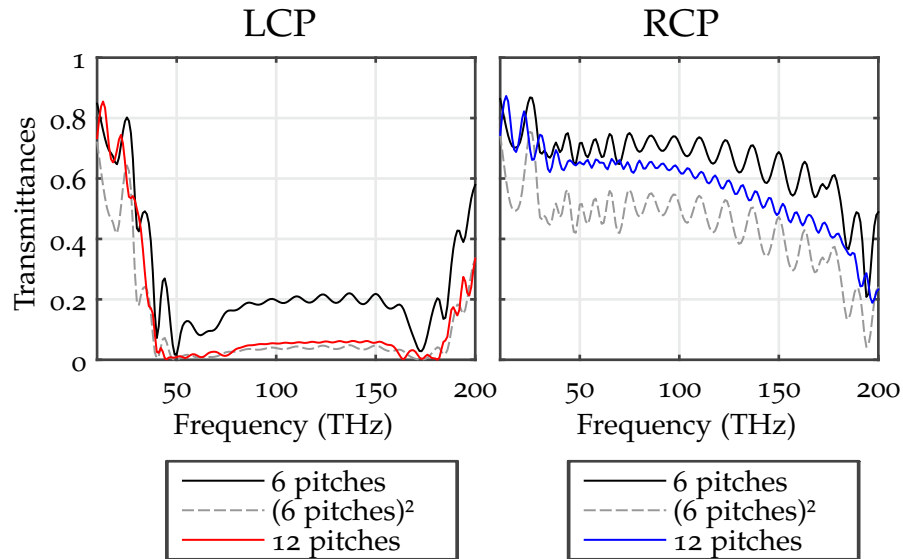


Figure 3.15: The effect of an increasing number of pitches is illustrated for tapered triple-helices with taper ratio $r_2/r_1 = 4$. Spectra are shown for $N_p = 6$ and $N_p = 12$ pitches. Furthermore, the transmittances for six pitches have been squared to give a rough approximation for a pure bulk effect, depicted by the dashed grey line.

In conclusion, I have shown in this section that for non-tapered N -helical metamaterials the bandwidth and extinction ratio cannot be optimized simultaneously, in large contrast to conventional helical metamaterials. By

introducing tapered N -helices, however, we have managed to achieve previously unmatched bandwidths of more than two octaves while at the same time enhancing the extinction ratio. Despite this improvement and the complete absence of polarization conversions, the polarizer performance is below that of conventional helical metamaterials and many orders of magnitude worse than what is achievable with wire-grid polarizers for linearly polarized light. Here, even more complex designs might bring the extinction ratio of helical metamaterials with N -fold rotational symmetry to competitive values.

We have to keep in mind though, that due to the fundamentally different principle of operation, *i.e.*, absorption of the undesired polarization instead of reflection, the polarization effect is based on true circular dichroism. Compared to other chiral metamaterials with N -fold symmetry and especially in comparison with natural chiral materials, such pronounced circular dichroism over a bandwidth of more than two octaves is unmatched.

3.4 DESIGNS BEYOND POLARIZER APPLICATIONS

In this final theoretical section, I will look at other possible applications for helical metamaterials beyond the simple broadband polarizer. For example, N -helical metamaterials have recently been proposed to serve as chiral near-field sources [76]. For this, $N = 4$ helices are not excited by circularly polarized, but by linearly polarized light, propagating in a direction orthogonal to the helix axis as depicted. The induced currents in the helices lead to a magnetic field in the enclosed volume that is either parallel or antiparallel to the electric field, depending on the handedness of the helices, thus, leading to strong chiral near-fields within the helical volume that could be employed for sensing of chiral molecules.

Here, we turn away from N -helical metamaterials for the scope of this section and instead introduce a completely different helical-metamaterial design where we do not eliminate circular-polarization conversions but rather enhance them purposefully.

We start by a small *gedankenexperiment*: Let us assume, that we let light propagate through an array of left-handed single gold helices and after a distance d , that shall be sufficiently large, through an array of right-handed gold helices with identical geometrical parameters. Both, left-handed and right-handed helices shall consist of 1.5 axial pitches each and from what we have learned in Section 3.1, over a broad frequency band we expect mainly right circularly polarized light after passage through the first array, as left-circularly polarized light couples to the left-handed helices and is reflected. As the second array, however, consists of right-handed helices, we expect the remaining light to be also reflected in that frequency band, due to the matching handedness. Similar to the case of two crossed linear polarizers one would therefore expect very little transmission for both circular polarizations.

What happens though if we move these two arrays of helices closer and closer together until they are finally connected? The resulting unit cell is depicted on the right-hand side in Figure 3.16. A small connection arc with radius r_C has been added to ensure a continuous gold wire without any sharp bends. Furthermore, a set of geometrical parameters feasible for later on fabrication was used in the scope of the following numerical calculations. The parameters are a lattice period of $a = 2 \mu\text{m}$, a helix radius

of $r_H = 500$ nm, a wire radius of $r_W = 250$ nm, and an axial lattice period of $H = 2$ μm . If we examine the total transmittances for LCP and RCP we find that LCP is blocked, as we would have expected, but the transmittance for RCP is unexpectedly high and on the order of approximately 80 %.

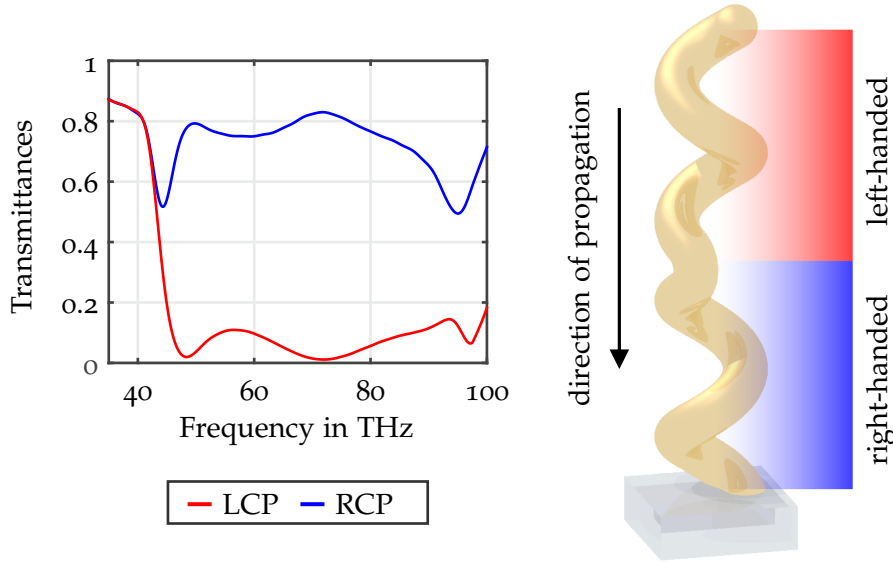


Figure 3.16: The novel helical-metamaterial design consisting of two coupled helices with opposite handedness is depicted on the right. For the indicated direction of propagation, the total transmittances for LCP and RCP have been calculated and are depicted in the diagram on the left. Surprisingly, high total transmittance for RCP is observed.

The reason for this lies in the circular-polarization conversion from RCP to LCP as we can see if we examine not the total transmittances but the squared moduli of the four individual elements of the Jones transmission matrix in circular-polarization basis. These are depicted in Figure 3.17. The normal transmittances are low, as expected for the case of orthogonal polarizers. In contrast to all previous metamaterial designs we have seen so far, the circular-polarization conversion from RCP to LCP is surprisingly high over a large band where it reaches values of 70 to 80 %.

Inspired by the asymmetry of the Jones matrix, *i. e.*, the large difference of the off-diagonal elements, the term *asymmetric transmission* has been coined.

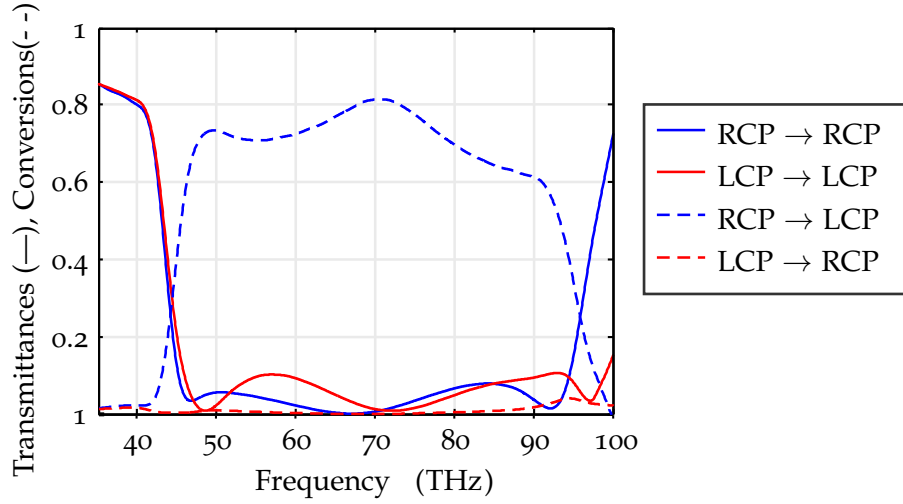


Figure 3.17: Squared moduli of the Jones transmission matrix are depicted. While the diagonal elements are low, the polarization conversion from RCP to LCP reaches values of up to 80 %.

One must however be careful not to confuse this term with the principle of an optical isolator, where by the use of non-reciprocal media, the total transmittance for unpolarized light varies depending on the direction of propagation. As I discuss reciprocal constituent materials only, the sum of all normal transmittances and conversions will always be equal for forward and reverse propagation direction, independent of the chosen polarization basis, as can easily be verified by Equation 2.56. Let us, however, take a closer look at the total transmittances for both directions of propagation. In forward direction these are given by

$$\begin{aligned} T_{\text{LCP}} &= |t_{\text{LL}}|^2 + |t_{\text{RL}}|^2, \\ T_{\text{RCP}} &= |t_{\text{LR}}|^2 + |t_{\text{RR}}|^2, \end{aligned} \quad (3.12)$$

as I have introduced them at the beginning of this chapter. For the reverse propagation we can exploit Equation 2.56 to substitute the coefficients of \vec{t}_r with those of \vec{t} :

$$\begin{aligned} T_{\text{LCP},r} &= |t_{\text{LL},r}|^2 + |t_{\text{RL},r}|^2 = |t_{\text{LL}}|^2 + |t_{\text{LR}}|^2, \\ T_{\text{RCP},r} &= |t_{\text{LR},r}|^2 + |t_{\text{RR},r}|^2 = |t_{\text{RL}}|^2 + |t_{\text{RR}}|^2. \end{aligned} \quad (3.13)$$

So let us now examine the difference in the transmittances for each circular polarization depending on the direction of propagation:

$$\begin{aligned}\Delta T_{\text{LCP}} &= T_{\text{LCP}} - T_{\text{LCP},r} = |t_{\text{RL}}|^2 - |t_{\text{LR}}|^2, \\ \Delta T_{\text{RCP}} &= T_{\text{RCP}} - T_{\text{RCP},r} = |t_{\text{LR}}|^2 - |t_{\text{RL}}|^2.\end{aligned}\tag{3.14}$$

By exploiting reciprocity we find that an asymmetry in the Jones matrix also leads to a difference in transmission for each circular polarization depending on the direction of propagation. Possible applications like diode-like devices have been proposed for metamaterials with such asymmetric Jones matrices [77].

Strong asymmetric transmission has been achieved experimentally for linear polarization with broadband operation [78, 79] and many more designs have been proposed [80–84]. For circularly polarized light very few metamaterial designs with asymmetric transmission have been reported so far, with generally either small operation bandwidth or small asymmetry ΔT [85–89].

But how can we understand this very high, asymmetric polarization conversion? From our *gedankenexperiment* earlier, we can already deduce, that it must be due to some sort of coupling between the two oppositely-handed helices. To examine this effect in detail, we have employed the commercial software package COMSOL Multiphysics to calculate the currents along the metal wire and we have done so at a frequency in the operation band, namely at 75 THz. In Figure 3.18(a) the current density is depicted for the case of a unit cell with a single right-handed helix with 1.5 pitches. I have already discussed similar calculations in Section 3.1. Nevertheless, I want to focus on a particular detail that we have previously ignored. As intuitively expected, incident left-handed circular polarization (LCP) does not couple to the helix and currents are rather small along the entire helix wire. On the contrary, when the handedness of the incoming circular polarization matches that of the helix, in this case RCP, pronounced coupling to the helix is present and strong currents are observed. The crux, however, is that the currents are mainly large in magnitude at the end of the helix from where the light impinges.

With this in mind, let us now examine our new design, the two coupled

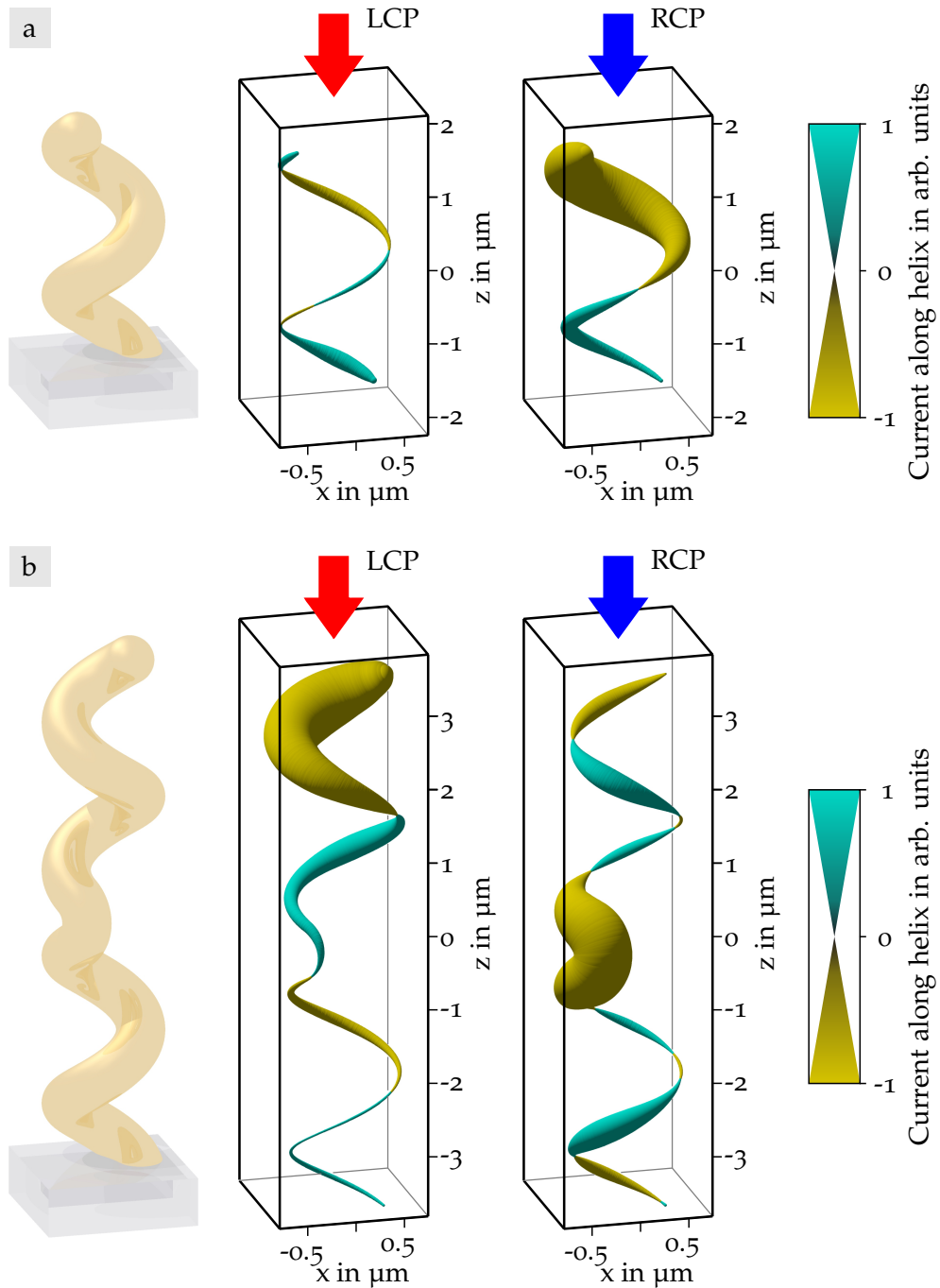


Figure 3.18: Similar to the calculations before in Section 3.1, the current densities along the helix wire have been calculated. In (a) the case of a single helix with 1.5 pitches is depicted under incident LCP (left panel) and incident RCP (right panel). Again, the color indicates the sign of the current for this fixed moment in time, while the thickness indicates the magnitude. In a similar way, in (b) the current densities have been calculated for the converter design.

helices within one unit cell. We therefore add a left-handed helix on top of the previously existing right-handed helix. On the left-hand side, again LCP is incident. There is no real surprise here, as the incident left-circularly polarized light couples to the left-handed helix and is reflected. As large currents are almost entirely limited to the very top of the structure, the bottom, right-handed helix does not play a role at all.

Let us now look at incident right-circular polarization, for which we expect strong conversions to left-circularly polarized light based on our numerically calculated spectra. The incident RCP couples to the lower right-handed helix, but as currents are now large in close vicinity to the connection arc, coupling between the two helices is evident and strong currents are also present in the left-handed helix. We have therefore excited the left-handed helix which will now emit into the far-field and it will do so with its respective handedness, *i. e.*, LCP, due to time-reversal symmetry [90].

Finally, the direction of this emission is also of importance for a complete understanding. As currents in the left-handed helix have been excited only in close vicinity to the connection arc, emission into the reverse direction, *i. e.*, reflection is blocked from the upper part of the helix. It will therefore emit only into the forward direction, thus completing the conversion from RCP to LCP.

To further illustrate the effect and necessity of coupling, we have carried out a series of numerical calculations, where the helical structure has been cut into two halves at the center of the connection arc. The circular-polarization conversion from RCP to LCP was then calculated for different separation distances between the two halves, starting at 0 nm, *i. e.*, connected helices, and going up to 1 μm . The results are depicted in Figure 3.19. Clearly, for most of the operation band, the conversion quickly decreases even for small separation distances. Therefore, most of the coupling can be assigned to direct coupling of the currents. Interestingly, however, at lower frequencies the conversion remains above 50 % even at separation distances of 1 μm . Keeping in mind that the fundamental mode is excited at 45 THz which also leads to a strong magnetic dipole moment, similar to a splitting resonator, one possible explanation for this effect could be long-range magnetic coupling.

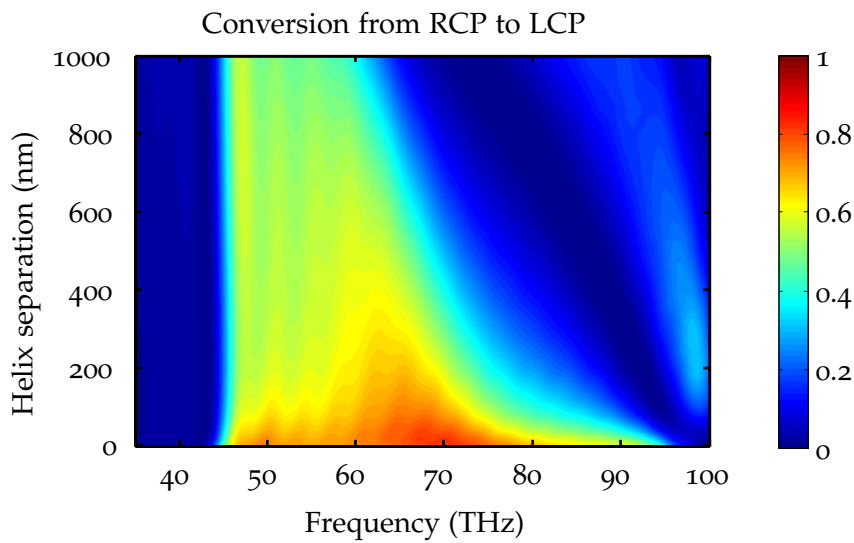


Figure 3.19: False-color plot depicting the conversion from RCP to LCP for a separated converter structure with a certain separation distance.

Additional numerical parameter sweeps are included in the Appendix A to illustrate the effects of varying for example the number of pitches or the helix radius.

To conclude this section, we recall that a metamaterial consisting of both right-handed and left-handed helices must not necessarily exhibit equal transmission for left- and right-circularly polarized light. While the normal transmittances are in fact equal – minor differences occur only due to the presence of the substrate – the modulus of the two circular-polarization conversions can in fact be very different, leading to strong asymmetric transmission. We have seen that the introduced design exhibits such circular-polarization conversions and asymmetric transmission of around 80% over a large bandwidth of approximately one octave, unmatched by any other reported design. I have explained this behavior by numerical calculations and have assigned it to a particular coupling effect based on electric coupling, but also possibly magnetic-dipole coupling.

With this, I also conclude the chapter on the theory of helical metamaterials. I have introduced a number of different helical-metamaterial designs, all predicated on the basic building block, the single helix. By combining multiple helices within a unit cell, be it by intertwining them or by connecting oppositely-handed helices, new chiro-optical effects have arisen. Circular-polarization conversions are not merely a side-effect anymore. We can either fully eliminate them for conversion-free polarizer operation or specifically enhance them to allow for strong asymmetric transmission. In the same way that these new features are appealing, fabrication of even more complex helical-metamaterial designs is challenging. In the following chapter the experimental methods for fabrication and characterization are introduced, before we get back to the different metamaterial designs that we have fabricated for operation at mid-infrared frequencies.

4 Chapter 4

EXPERIMENTAL METHODS

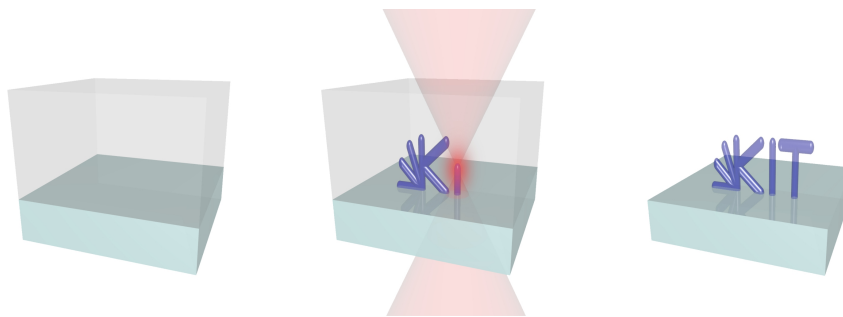


Illustration of the general direct laser writing workflow.

In this chapter, I will first review the principle of direct laser writing and briefly touch upon the diffraction limit for three-dimensional laser lithography. Furthermore, I will explain the concept of stimulated-emission-by-depletion-inspired direct laser writing (STED-DLW). Subsequently, the fundamentals of electrochemical deposition of metals will be explained, as well as the electrochemical gold deposition process employed in the scope of this thesis. I will introduce a novel fabrication approach for helical metamaterials, based on STED-DLW. Finally, the optical characterization at mid-infrared frequencies is explained.

4.1 LASER LITHOGRAPHY

4.1.1 FUNDAMENTALS OF DIRECT LASER WRITING

The success story of metamaterials was mainly possible, because fabrication techniques, for example, electron-beam lithography were already well established and have allowed for realizing complex metallic structures with sub-micron feature sizes, thus enabling operation at visible or infrared frequencies. Nevertheless, fabrication processes based on electron-beam lithography can only yield two-dimensional metamaterials, therefore limiting not only possible effects and applications to one spatial direction. Creating bulk-like metamaterials by self-assembly techniques has been proposed, with the advantages of scalable fabrication and unmatched feature sizes [91]. On the downside, however, self-assembly is limited in design freedom.

By successively applying electron-beam lithography with subsequent metal-evaporation processes, multiple layers of a two-dimensional metamaterial can be stacked to form bulk-like metamaterials. Despite the possibility to vary the design from layer to layer, this rather time-consuming approach does not yield full three-dimensional freedom. Geometrical structures like helices cannot be realized by such layered metamaterial designs. The fabrication of three-dimensional metamaterials therefore remains a challenge [32].

Here, we will employ a technique called “direct laser writing” (DLW) that can be seen as the high-resolution analogue to conventional macroscopic 3D printing [92, 93]. DLW allows for the fabrication of almost arbitrary three-dimensional structures with sub-micron feature sizes [94–96]. The high resolution is achieved by a strongly focused laser that leads to a change in solubility inside a liquid or solid photoresist. Before examining details and limitations of direct laser writing, I will first discuss the general principle and workflow.

Figure 4.1 illustrates the workflow of direct laser writing in three basic steps. In a first step, a photoresist is either spin-coated or drop-cast onto a substrate. The laser is then tightly focused into the photoresist, where in the focal volume it will induce a change of solubility. I will consider almost exclusively negative-tone photoresists in which this change in solubility is

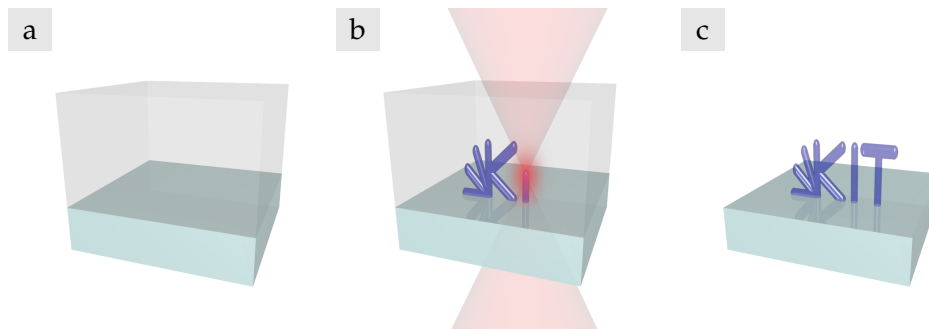


Figure 4.1: Illustration of the general workflow of direct laser writing. (a) A substrate is first covered by a liquid or solid photoresist, by either drop casting or spin coating, respectively. (b) By strongly focusing a laser into the photoresist, local polymerization is initiated. Three-dimensional structures can be created by moving the focus relatively to the substrate. (c) Rinsing the sample in a solvent washes away unexposed photoresist, while the polymerized resist remains.

achieved by local polymerization of a monomer contained in the photoresist. By then moving the relative position of the focus with regard to the substrate, almost arbitrary three-dimensional structures can be created. Apart from limitations due to resolution that will be discussed later on, the choice of geometry is only limited by the fact that free-floating structures cannot be created. In a final step, the remaining, unexposed photoresist is washed away with a solvent, leaving only the insoluble three-dimensional polymer structure. The individual components and fabrication steps will now be explained in more detail.

THE PHOTORESIST

The photoresists that I will consider in the scope of this thesis shall consist of a transparent monomer, usually based on multi-functional acrylates that can undergo radical-based polymerization. Furthermore a photo-sensitive initiator molecule, the photoinitiator, is added to the monomer. The excitation energy of the photoinitiator molecule is on the order of 3 eV. After excitation the molecule will decay, giving rise to two or more radicals that in turn initiate the chain reaction. Most photoresists, exhibit a reasonably high threshold, meaning that a certain minimum exposure dose must be reached

in order to obtain the necessary degree of insolubility.

THE EXPOSURE LASER

The large majority of direct laser writing approaches is based on multi-photon exposure. To understand the necessity of this nonlinear absorption process let us first consider a purely linear excitation and polymerization process. This also implies excitation of the photoinitiator *via* one-photon absorption ($1PA$). The wavelength of the laser λ_{1PA} must thus be chosen so that it corresponds to the excitation energy of the initiator molecule ΔE

$$\lambda_{1PA} = \frac{hc}{\Delta E}. \quad (4.1)$$

In this case, low photoinitiator concentrations are crucial, as otherwise the intensity would strongly decrease along the optical axis. We choose a coordinate system where the z -axis is parallel to the optical axis. The intensity of the laser shall be denoted as $I(z)$. I use the term intensity here synonymous for the squared modulus of the electric field $|\vec{E}|^2$. This is not completely accurate, as the intensity which is the time-averaged Poynting-vector $\langle \vec{E} \times \vec{H} \rangle$ is in general different from the time-averaged squared modulus of the electric field $\langle |\vec{E}|^2 \rangle$. For the sake of convenience, however, I will use the terms interchangeably here, as it is often done in literature.

The number of photons absorbed in a volume element at (x, y, z) is proportional to the intensity $I(x, y, z)$, which reaches maximal values at the focus. The integral of the intensity in each z -slice, however, is constant as we assume low photoinitiator concentration and therefore constant transmitted power along the optical axis:

$$\int I(x, y, z) dx dy = P(z) = \text{const.} \quad (4.2)$$

Therefore the number of absorbed photons is also constant in each z -slice. If we now were to write a simple plane with large enough dimensions, located at $z = z_0$, points below and above that plane would experience the exact same exposure and we would not write a plane but rather a block. Nevertheless, direct laser writing based one-photon absorption can still yield certain three-dimensional designs, due to the threshold behavior or the nonlinearity of subsequent processes leading to polymerization [97].

To allow for full three-dimensional writing capability, nonlinear multi-photon excitation is employed. While it is not clear how large the degree of nonlinearity is precisely in many photoresists, I will limit my discussion here to the case of two-photon excitation (2PA), as the findings are qualitatively the same for multi-photon excitations of higher order. The laser wavelength is chosen such, that

$$\lambda_{2\text{PA}} = 2 \frac{hc}{\Delta E}. \quad (4.3)$$

Here, ΔE must denote the fundamental energy transition, as otherwise, the normally very weak two-photon absorption would be dominated by much stronger one-photon absorption. The exposure dose, *i. e.*, the number of absorbed photons, is now proportional to the square of the intensity. In contrast to what we have seen before, the integrated exposure dose in each z -slice is not constant:

$$\int I(x, y, z)^2 dx dy \neq \text{const.} \quad (4.4)$$

This, in combination with the previously discussed threshold behavior, allows for localized polymerization in all three dimensions and therefore arbitrary three-dimensional designs.

In reality, two-photon absorption cross sections are very small and the one-photon absorption cross section is never completely negligible. Pulsed excitation lasers with tightly confined focuses in time on the order of a few hundred femtoseconds, yield high peak intensities and are therefore favorable for direct laser writing applications.

FOCUSING OPTICS

High-numerical aperture objective lenses, typically on the order of $NA = 1.2 - 1.4$, are used to achieve sub-micron resolution. Lower numerical apertures lead to a large increase in the axial dimension of the focus. Therefore, one obtains also a worsened aspect ratio, defined as the ratio of axial to lateral dimension of the focus. Naturally, a high aspect ratio of the point-spread function also translates to a high aspect ratio of the polymerized volume element, that we will call *voxel* in style of the word pixel for a two-dimensional picture element. I will discuss the term resolution and the importance of a high numerical aperture of the focusing optics in more detail in Section 4.1.2.

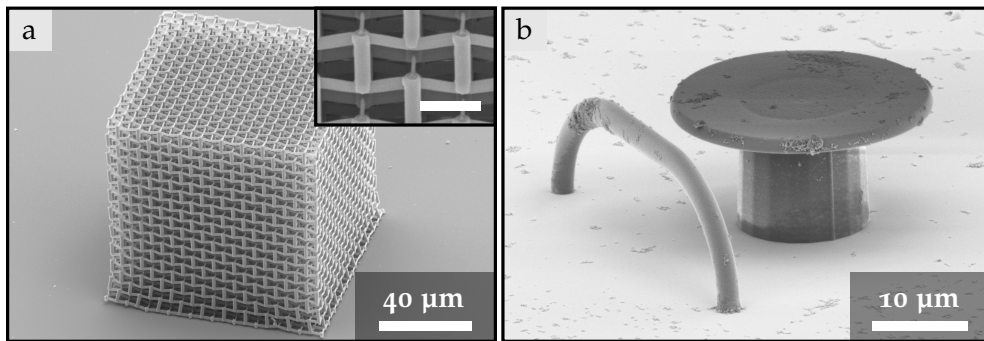


Figure 4.2: Scanning electron micrographs of two examples for polymer structures created with direct laser writing. (a) Mechanical metamaterial exhibiting a negative Poisson's ratio. The scale bar in the inset corresponds to $5\ \mu\text{m}$ (courtesy of T. Bückmann). (b) Waveguide and disc resonator, created with direct laser writing, both containing nanodiamonds that serve as single-photon sources.

Some examples of three-dimensional polymer structures created *via* direct laser writing are depicted in the scanning electron micrographs in Figure 4.2. In the left-hand image a mechanical metamaterial with a negative Poisson's ratio is depicted [98]. In this case, so called "Dip-in" direct laser writing was employed, where instead of immersion oil the photoresist itself was used as an immersion medium into which the objective lens was immersed. This allows us to eliminate height-dependent aberrations and height limitations due to the finite working distance. In Figure 4.2(b) nanodiamonds with inherent nitrogen-vacancy centers have been dispersed in the photoresist [99]. These function as single-photon emitters that can be included *via* direct laser writing in integrated-optics designs. We see that the possible applications for direct laser writing are numerous [93]. Nevertheless, in the following section I will discuss certain limitations with regard to the achievable resolution.

4.1.2 BREAKING THE DIFFRACTION LIMIT

In the previous section, I have discussed the general workflow of direct laser writing and have seen that *via* multi-photon absorption it is possible to create arbitrary three-dimensional structures. I have furthermore briefly mentioned the threshold of the photoresist that causes polymerization only in a confined volume where the intensity of the excitation laser is sufficiently high. In principal, one can slowly decrease the power of the excitation laser so that the maximum intensity in the focus approaches the threshold intensity. The exposed volume will then also decrease to arbitrarily small sizes. In reality, however, small fluctuations in either the laser power or in the threshold intensity, due to thermic effects for example, will not allow arbitrarily small structures. Nevertheless, there is no fundamental lower limit for the feature size, *e. g.*, size of a voxel or line.

One could now be inclined to think that if it is possible to write arbitrarily small features, one can also place them arbitrarily close together. We will see, however, that there is a minimum distance when placing two voxels or lines next to each other, below which the two objects cannot be distinguished anymore. A very similar concept was formulated for imaging in microscopy more than 150 years ago by Ernst Abbe in his famous equation often called Abbe's diffraction limit:

$$a_{xy} = \frac{\lambda}{2NA} \quad (4.5)$$

Abbe's formula states that when imaging a grid of lines, the minimum distance between those lines a_{xy} for which they can still be seen as separate lines is proportional to the imaging wavelength λ and inversely proportional to the numerical aperture NA . While the results are very similar, one cannot simply use Abbe's formula when discussing the resolution of direct laser writing based on two-photon absorption.

First, we must clarify why there is a lower limit at all. A thorough discussion can be found in References [100] and [101]. Here, I will outline the most important findings to give the reader a basic understanding of the involved mechanisms in diffraction-limited and -unlimited direct laser writing.

While simultaneous exposure of two parallel lines is similar to the case of imaging, subsequent exposure of two parallel lines does not seem to be

bound by diffraction limits. This would in fact be true, if the photoresist lacked any form of “memory”, *i.e.*, any region that had previously been exposed only to intensities below the threshold intensity, would still be in its initial state. However, due to good agreement of experiments and calculations for the expected lower limit, photoresists do tend to have this memory effect.

One can partially explain the threshold behavior for example, by a minimum chain length or cross linking in the polymerized structure in order to yield the necessary insolubility of the final structure. In the regions exposed with intensities below the threshold intensity, polymerization still occurs, but the degree of insolubility is not achieved after a single exposure. By exposing a volume several times with intensities below threshold intensity, the exposure doses add up and the volume will be polymerized. To determine the minimum lateral distance for two voxels to be separated, one can calculate the electric field $E(x, y, z)$ in the focus and then add up the moduli by the power of four, as we assume two-photon absorption, for a voxel placed at $(0, 0, 0)$ and one placed at $(a_{xy}, 0, 0)$. Following Sparrow’s criterion, we define the critical distance as the distance where the added squared intensities $|E(x, y, z)|^4 + |E(x - a_{xy}, y, z)|^4$ yield a flat-top profile around $x = a_{xy}/2$. For common experimental parameters ($\lambda = 800$ nm, $NA = 1.4$, and circular polarization), one obtains a critical distance, which we will from now on call lateral resolution of $a_{xy} = 200$ nm. Similarly, the axial resolution can be calculated to $a_z = 500$ nm [101].

It is also possible to adapt Abbe’s diffraction limit to the case of two-photon absorption, by assuming Gaussian intensity distributions. Two-photon absorption then should lead to an increased confinement by a factor of $\sqrt{2}$, thus giving

$$\begin{aligned} a_{xy} &= \frac{\lambda}{2\sqrt{2}NA} = 202 \text{ nm} \\ a_z &= \frac{\lambda \cdot AR}{2\sqrt{2}NA} = 505 \text{ nm} \end{aligned} \tag{4.6}$$

where AR denotes the aspect ratio of the focal volume. Clearly, these values are very close to the ones calculated numerically *via* the generalized Sparrow criterion for two-photon absorption and are therefore a very good

approximation for the resolution of a lithography system.

While in mechanics, biology, or integrated optics the resolution of direct laser writing is more than sufficient, it restricts operation for photonic crystals and optical metamaterials to near-infrared or mid-infrared frequencies. In order to break this diffraction limit, we add a second laser to the direct laser writing setup that is used for stimulated emission depletion (STED) of the excited photoinitiator molecules.

STED-microscopy was first introduced by Stefan Hell in 1992 [102]. In microscopy, a fluorescent dye molecule is excited *via* one-photon absorption with a first laser, the excitation laser. Before the molecule can fluoresce, a second laser, which we will call the depletion laser, with a wavelength at the short-wavelength edge of the fluorescence spectrum, brings the molecule back into the ground state by stimulated emission. By shaping the depletion-laser focus appropriately, fluorescence can be confined to a much smaller volume. By spectral filtering, one can finally easily discriminate between the desired fluorescence and the depletion wavelength. With this, lateral resolution down to values of 5 nm has been demonstrated [103].

In STED-inspired direct laser writing on the other hand, the goal is to confine radical formation by the photoinitiator molecule to a small volume. The focal shapes of the two employed lasers are depicted in Figure 4.3(a). Just as in the case of conventional direct laser writing, a near-infrared femtosecond laser is used for two-photon excitation. The displayed squared modulus of electric field has been calculated for a wavelength of $\lambda_{\text{exc}} = 810 \text{ nm}$ and a numerical aperture $NA = 1.4$, using the focus calculation method described in Reference [100]. After two-photon excitation into some higher state, the molecule will relax non-radiatively to the S_1 state as depicted in the Jablonski diagram in Figure 4.3(b). From here, without the presence of a depletion laser, the molecule can on one hand go back down to the ground state by spontaneous emission. On the other hand, it can also undergo intersystem-crossing into an excited triplet state, from which it decays to form radicals and initiate polymerization. In the same way that fluorescence has been suppressed in STED-microscopy, we now suppress both fluorescence and inter-system crossing by stimulated emission depletion of the excited photoinitiator molecule, thus also suppressing polymerization. Of course, we do

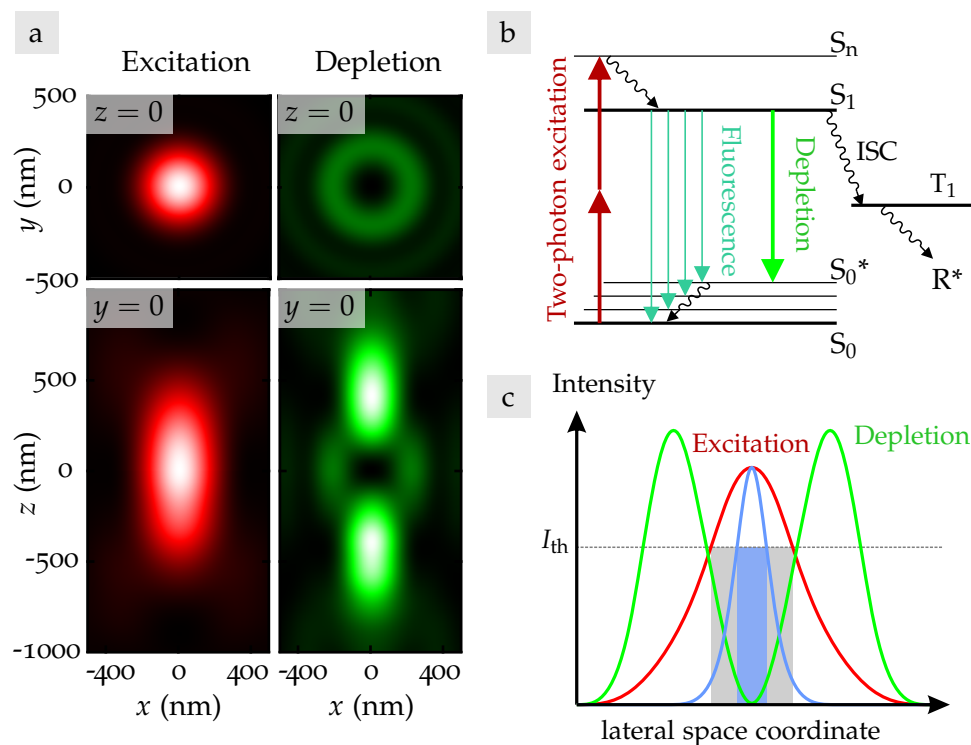


Figure 4.3: (a) Calculated squared moduli of the electric field $|\vec{E}|^2$ for excitation and depletion focus for an objective lens with numerical aperture $NA = 1.4$. The left and right panels depict $x-y$ and $x-z$ cuts for the the excitation laser at $\lambda = 810\text{nm}$ and the depletion laser at $\lambda = 532\text{nm}$, respectively. A cylindrical disk-shaped phase mask is used to achieve the point-spread function of the depletion focus. (b) Jablonski diagram of a basic model for two-photon excitation, subsequent inter-system-crossing (ISC) to a triplet state (T_1) and radical (R^*) generation. The depletion path from the lowest electronically excited state (S_1) to a vibronically excited state (S_0^*) is also indicated. (c) Illustration of the depletion principle in one dimension. Without the depletion laser, a line width corresponding to the width of the grey box would be achieved. Through depletion on the outskirts of the focus, the line width is reduced to the width of the blue box.

not want to suppress polymerization entirely. For this, the depletion laser passes through a phase mask prior to focusing that induces a phase shift φ of

$$\varphi = \begin{cases} \pi & \text{for } r \leq r_{\max}/\sqrt{2} \\ 0 & \text{for } r > r_{\max}/\sqrt{2} \end{cases} \quad (4.7)$$

where r_{\max} denotes the radius of the opening aperture at the microscope objective lens. The resulting squared modulus of the electric field is also depicted in Figure 4.3 for a wavelength of $\lambda = 532$ nm. This focal shape, also called “bottle focus”, leads to depletion laterally around the focal point and to even stronger depletion along the optical axis above and below the focal point. Therefore, not only lateral and axial resolution, but also the aspect ratio, *i. e.*, the ratio of axial to lateral dimensions of a voxel, will be enhanced [104]. Employing STED-inspired direct laser writing, three-dimensional resolution well below the diffraction limit has been achieved experimentally:

$$\begin{aligned} a_{xy} &= 175 \text{ nm} && \text{with donut-focus depletion} \\ a_z &= 373 \text{ nm} && \text{with bottle-focus depletion} \end{aligned} \quad (4.8)$$

With this enhanced resolution applications such as complete photonic bandgaps or carpet cloaks have become possible at visible frequencies [45, 105].

I note, that the choice of wavelength for the depletion laser is not trivial. At longer wavelengths the oscillator strength decreases and therefore also the depletion is less efficient. At shorter wavelengths, on the other side, one-photon absorption of the depletion laser increases which ultimately leads to a worse resolution than without depletion. Also one must emphasize, that the model shown in Figure 4.3(b) is a crude simplification of reality. On one hand, higher-order effects than only two-photon absorption play an important role for most photoinitiators [106]. Furthermore, the effect of quenching molecules, in particular dissolved oxygen, plays an important role and has been neglected from discussion here [107].

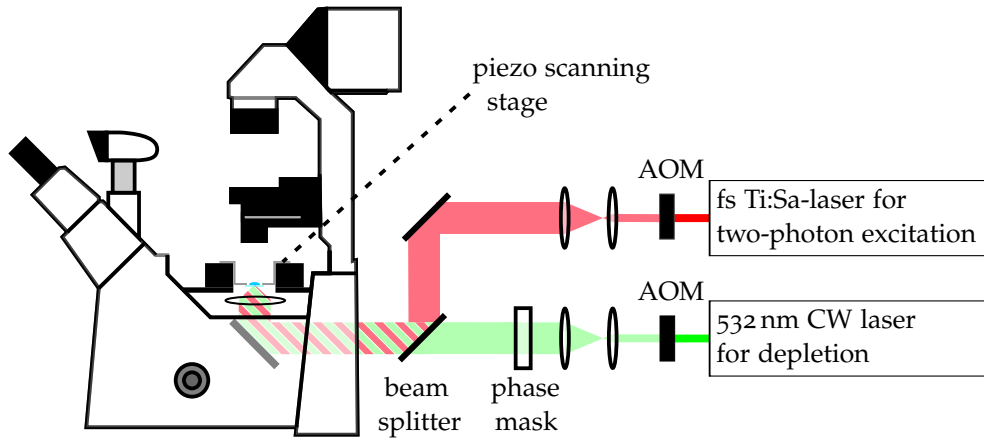


Figure 4.4: Schematic illustration of the lithography setup used in the scope of this thesis. A femtosecond pulsed titanium-sapphire laser serves as the excitation laser. A frequency-doubled continuous-wave (CW) neodymium-YAG laser is used for depletion. Acousto-optical modulators (AOM) allow for convenient control over the laser power. The sample is moved with respect to the focus in three-dimensions with a piezo scanning stage.

4.1.3 LITHOGRAPHY SETUP

The lithography setup employed in this thesis is described in detail in Reference [100] and is depicted schematically in Figure 4.4. A titanium-sapphire laser (Spectra Physics MaiTai HP) at $\lambda_{\text{exc}} = 810 \text{ nm}$ with pulse lengths of approximately 100 fs was used as the excitation laser. The depletion laser is a frequency-doubled continuous-wave neodymium-doped yttrium-aluminium-garnet laser (Spectra Physics Millennia X) at $\lambda_{\text{depl}} = 532 \text{ nm}$. Acousto-optical modulators (AOM) are used for convenient and quick control of the transmitted laser power. The focusing objective lens has a numerical aperture of $NA = 1.4$ (Leica HCX PL APO 100x Oil). The sample is mounted onto a piezoelectric stage (Physik Instrumente P-527.3CL) allowing for precise translation in all three dimensions during exposure. The piezoelectric stage is furthermore mounted onto a motorized stage (Märzhäuser Wetzlar, SCAN IM 120 x 100) so that the writing field of the piezoelectric stage, $200 \mu\text{m} \times 200 \mu\text{m} \times 20 \mu\text{m}$, can be moved across the entire sample. Throughout this thesis a photoresist containing the monomer pentaerythritol triacrylate (PETA) and 0.25 wt% 7-diethylamino-3-thenoylcoumarin (DETC)

as photoinitiator was used [104, 108]. After excitation of DETC radicals are generated that initialize polymerization of the monomer PETA. As the latter is a multi-functional monomer, *i. e.*, a monomer with more than one acrylate groups, a cross-linked polymer network is created that is insoluble.

4.2 ELECTROCHEMICAL DEPOSITION OF METALS

4.2.1 FUNDAMENTALS OF ELECTROCHEMICAL DEPOSITION

In the previous sections, I have discussed conventional and STED-inspired direct laser writing, lithography methods that can both yield three-dimensional structures with sub-micron feature sizes. While for photonic crystals or applications in transformation optics the constituent polymer suffices, for metamaterial applications and in particular for helical metamaterials we require metallic structures. Metallization of polymer templates can be achieved *via* physical vapour deposition (PVD) [109]. While PVD offers good and probably unmatched metal quality, due to the anisotropic evaporation process true three-dimensional metallization is impossible. Furthermore, the underlying will also be metallized which therefore impedes operation in transmission. The same problem is at hand when utilizing chemical vapour deposition (CVD). In contrast to PVD, however, CVD allows for isotropic deposition. Three-dimensional polymer templates can therefore be truly reproduced [110]. On the downside, metal quality is usually much lower, leading to an increase in losses.

In the scope of this thesis, electro-chemical deposition of gold from aqueous solution was employed that had previously been introduced already for the fabrication of conventional helical metamaterials [8]. Good metal quality and deposition within almost arbitrarily structured templates are the biggest advantages of this approach. However, as will be discussed in the following section, electro-chemical deposition poses higher demands at either the geometry or the chemical properties of the polymer template.

Before I introduce the electrochemical process employed in this work, I first discuss some fundamentals of electrochemical deposition of metals from aqueous solutions. For a more detailed discussion of the topic, I recommend Reference [111], which has also inspired certain figures within this section.

To fully understand the deposition of metals from aqueous solution, we must first discuss how metals are brought into solution. In contrast to molecular matter like sugar for example, metals are insoluble in water. *Via* redox-reactions, however, metals can form salts in the presence of either an acid or a non-metal. Salts are crystalline, ionic compounds of the two

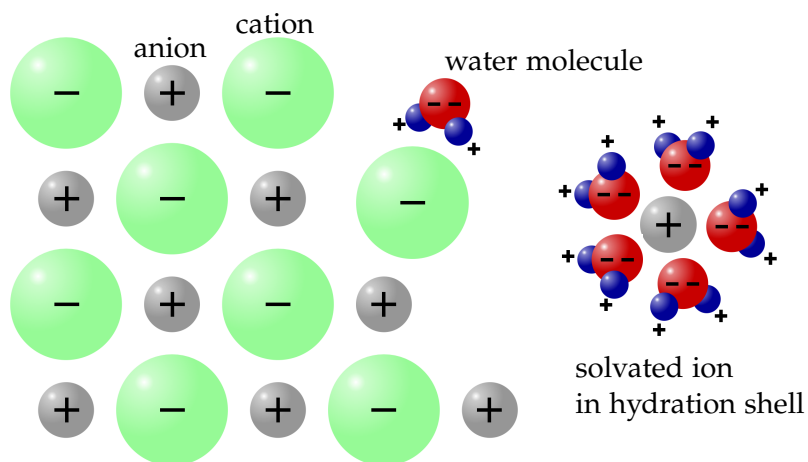


Figure 4.5: Schematic depiction of an ionic crystal and its solvation in water. The water molecules form a hydration shell around a solvated ion, due to the dipole moments, indicated by the plus and minus symbols.

corresponding ions. For the metal atom the number of electrons is usually decreased, *i. e.*, it is oxidized, leaving the positively charged anion. Similarly, the non-metal atom is reduced and one obtains the negatively charged cation. We are familiar with these reactions as they appear in the form of corrosion in everyday life.

A schematic illustration of such an ionic crystal is shown in Figure 4.5. Many of these salts are soluble in water. The reason for this lies in the polar configuration of the water molecule that originates from the high electronegativity of oxygen. The charged ions are separated from the crystal lattice and interact with the polarized water molecules that then form hydration shells around the ions, as shown for the solvated ion on the right-hand side. Due to the hydration shell, multiple ions cannot aggregate anymore which would in turn cause precipitation. In reality, the situation is more complex. Water molecules are not only oriented in the hydration shell, but also partially in close proximity to it. Furthermore, due to attractive forces between oppositely charged ions, ion pairs with mutual or shared hydration shells occur. Here, I however restrict the discussion to this simple picture.

Let us now imagine a metal electrode M that has been immersed into such a solution with metal ions M^+ . The processes at the interphase between

the aqueous solution and the electrode are very complex, due to potential differences and the interaction of bound metal atoms, solvated ions, and the hydration shells. The details are described by the Grahame triple-layer model, which is an extension to Helmholtz's compact double-layer model and Stern's model [111]. The latter includes the presence of a diffuse layer as described in the Gouy-Chapman model. A small fraction of metal atoms from the electrode will go into solution and some solvated ions in turn will adsorb to the metal electrode. Let us assume that the former direction of ion movement is dominant, leaving behind an excess of electrons at the surface. The negatively charged surface in turn repels the negatively charged anions and attracts additional hydrated metal ions. Therefore, the metal electrode has an effective negative charge close to the interface, while the solution in close proximity to the electrode is effectively positively charged.

Directly at the negatively charged metal interface this leads to an overall orientation of the water molecules, due to their electric dipole moment. The volume defined by the water molecules is called the "inner Helmholtz layer". Metal ions that appear here, are either already partially or fully dehydrated.

Further away from the metal-solution interface the "outer Helmholtz layer" is formed by the closest possible distance for still hydrated ions. The distribution of these positive ions is homogeneously spread across the electrode interface, thus forming an effectively positively charged plane parallel to the negatively charged metal interface. Similar to a parallel-plate capacitor, the potential will therefore decrease linearly in this region.

Even further away from the electrode there still exists an excess of positively charged, solvated ions due to attraction from the negatively charged metal surface. The excess concentration decreases exponentially with increasing distance from the interface which in turn also causes an exponentially decreasing potential. The dimensions of the diffuse layer depend on the concentration and for very high concentration the diffuse layer can be neglected.

The three layers are illustrated in Figure 4.6 together with a qualitative depiction of the potential. The dissociation, solvation, and hydration energies, as well as factors like temperature will define the final equilibrium state. One possible application for such interfaces are galvanic cells where two of such metal-solution interfaces lead to an electrical current which can then be

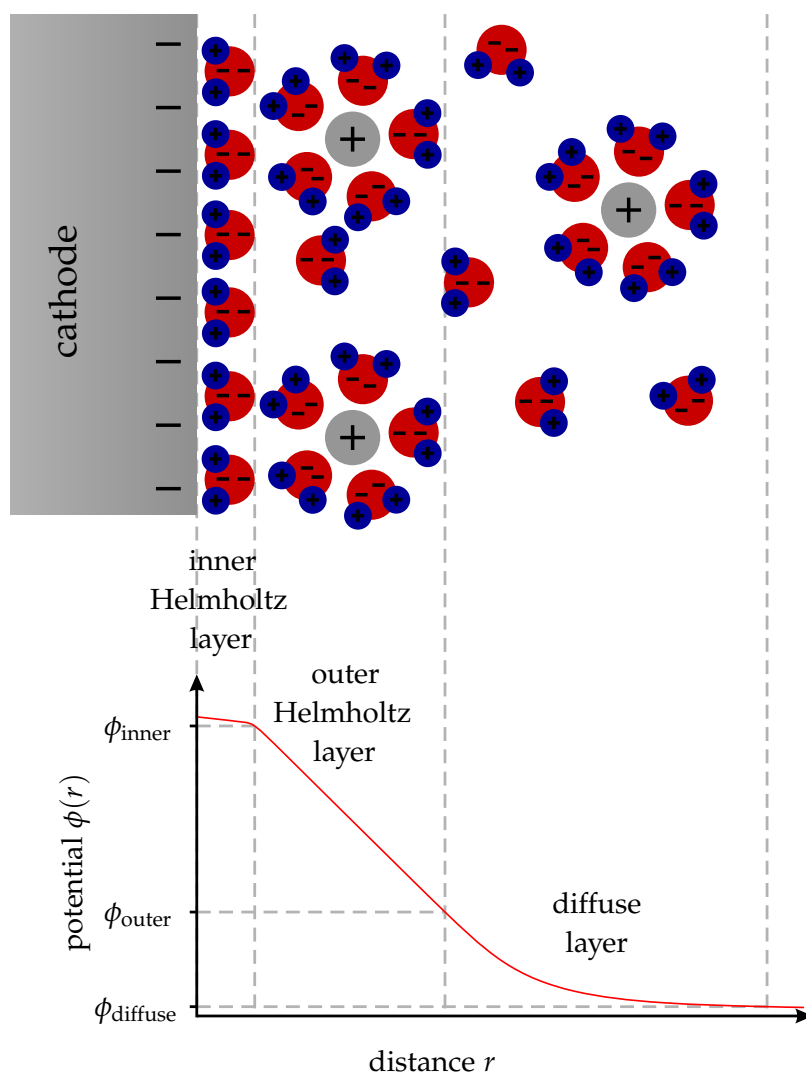


Figure 4.6: The triple-layer model is depicted. In close proximity to the metal surface, oriented water molecules form a densely packed layer (inner Helmholtz layer). Stationary adsorbed, but still hydrated ions form the outer Helmholtz layer. Here the potential, as depicted below, decreases linearly. Further away from the interphase in the diffuse layer, an excess of positively charged ions is present, leading to an exponential decrease of the potential. Far away from the interphase, *i. e.* in the bulk liquid, the sum of all charges is zero.

used to drive an electrical load.

Here, we are more interested in the case of an electrolytic cell, where we apply a certain voltage to two metal electrodes, both immersed in the same solution. The situation is illustrated in Figure 4.7. Note that the elements constituting the anode and cathode do not have to be the same as the one of the ions respectively, as we will see later in the case of electrochemical gold deposition. For now, we simply assume that both electrodes consist of a noble metal that is considered insoluble in water. At the negatively charged cathode one will now observe the following equilibrium reaction:



where z denotes the electric charge of a single metal cation in units of elementary charge.

By applying a voltage, this equilibrium reaction is pushed towards the right, leading to a deposition of metal atoms on the cathode and a current

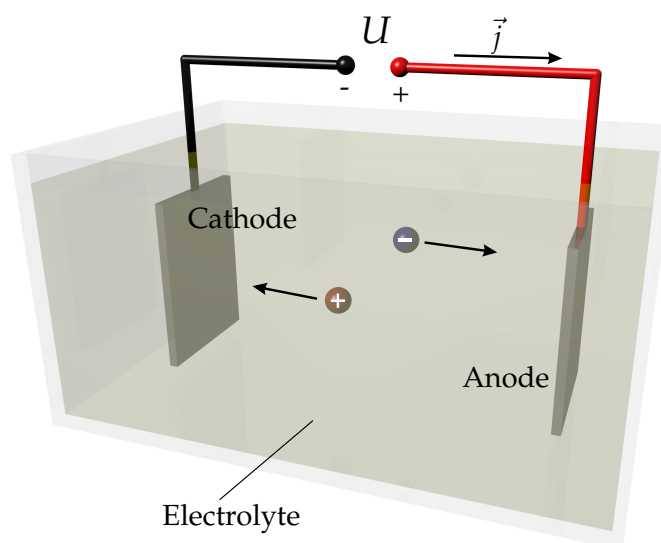


Figure 4.7: Principle of an electrolytic cell. By applying a voltage across two immersed electrodes, a current results that is carried by ion movement in the solution. The positively-charged metal anions move to the cathode, where they are reduced – provided that the potential is chosen appropriately – and metal is deposited.

supported by ion movement in the electrolyte. Neglecting any other possibly involved ions, by simple conservation of charge one can calculate the deposited metal mass m_M for a given current I and deposition time t by exploiting Faraday's laws of electrolysis [112]:

$$m_M = \frac{I \cdot t \cdot M}{F \cdot z} \quad (4.10)$$

where $F = N_A \cdot e$ denotes Faraday's constant and M is the molar mass of the metal. If furthermore the surface area A of the cathode is given, the equation above can be divided by A and one obtains the change in deposited material thickness over time:

$$\frac{d_M}{t} = \frac{j \cdot M}{F \cdot z \cdot \rho}. \quad (4.11)$$

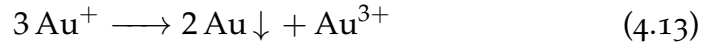
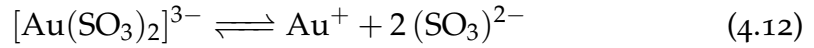
In passing, I have introduced the current density $j = \frac{I}{A}$ and the bulk metal density ρ . While this is certainly only a rough estimation, not taking into account the electrode efficiency or participation of other ions, we will see that it yields very precise results for our system. The accuracy of this approximation is however strongly dependent on the current. The electrode efficiency, *i.e.*, the ratio of the actually deposited mass to the calculated deposited mass, can decrease significantly if the current is chosen to large, as currents in the electrolyte might be diffusion limited. Furthermore, metal quality may decrease with increasing currents, especially on electrodes of a different material. When ions are adsorbed at the metal-solution interface they are not stationary, but can undergo subsequent surface diffusion. Lower currents lead to prolonged surface-diffusion timescales and thus larger grain sizes.

In this work gold has been deposited from aqueous solution in a process where a constant current was applied. In situations, where not only the deposition of the metal, but also the metal-salt is possible, the driving voltage must be controlled very precisely. A more thorough discussion of electrochemistry is necessary to fully understand the finer details of the deposition mechanism and to determine the potentials when depositing in such a voltage-controlled environment. As it does not apply here, I refer to literature for the interested reader [111].

4.2.2 GOLD DEPOSITION IN POLYMER TEMPLATES

After having discussed the fundamentals of electrochemical deposition of metals, I will now give a detailed description of our process with which we have successfully deposited gold in nanostructured polymer templates previously fabricated *via* STED-inspired direct laser writing. The general procedure has been introduced by J. K. Gansel and we have employed the same process with some adjustments [113].

The electrolyte was provided by K. Bade from Institute of Microstructure Technology (KIT). As individual gold ions are not stable in aqueous solutions, the gold is bound in sulfite complex ions $[\text{Au}(\text{SO}_3)_2]^{3-}$. The corresponding anions are sodium ions. The complex ions are disassociated to Au^+ and $(\text{SO}_3)^{2-}$ at the cathode during deposition. In a subsequent reaction step atomic gold precipitates:



In solution the complex ions can undergo the same reactions. To prevent the resulting precipitation of gold in solution, the sulfite concentration is increased by adding sodium sulfite to the solution. This pushes the equilibrium to the left and hinders the formation of free gold ions. The other components of the electrolyte are listed in Table 4.1. Titriplex ($\text{C}_{10}\text{H}_{16}\text{N}_2\text{Na}_2\text{O}_8 \times 2 \text{H}_2\text{O}$) is added to increase conductivity and furthermore bind other metallic ions to ensure high gold purity. In a similar way ethylene diamine ($\text{C}_2\text{H}_4(\text{NH}_2)_2$) is added to bind free gold ions Au^+ that form an equilibrium in solution. The pH-value of the electrolyte is set to $\text{pH} = 7.5$ and the temperature was set to $T = 57^\circ \text{C}$.

A platinum mesh electrode serves as the anode in solution. Here, sulfite ions are oxidized to dithionite and sulfate ions. Similar to Reference [113], a sample holder made of polytetrafluoroethylene is used. The opening is however smaller, thus exposing a smaller area of the substrate to the electrolyte ($A = 28.26 \text{ mm}^2$). This is necessary, as gold will be deposited on the majority of the accessible substrate surface. Larger surface areas lead to an undesirably high electrical current for a fixed current density.

Table 4.1: Chemical components in the gold electrolyte and respective concentrations used in this work.

Component	Concentration
Sodium gold sulfite	25 g/l
Sodium sulfite	20 g/l
Titriplex	30 g/l
Ethylene Diamine	22 ml/l

Furthermore, the current density was slightly reduced to $j = 2.68 \frac{\mu\text{A}}{\text{mm}^2}$ by empirical optimization. The current is supplied by a constant-current source (6221 AC and DC current source, Keithley Instruments GmbH).

4.3 FABRICATION PROCESS

Having covered the fundamentals of both, STED-inspired direct laser writing and electrochemical deposition of gold, I will now go through the fabrication procedure step by step. The process is based on a very similar approach by Gansel *et al.* from 2009, where conventional direct laser writing in a positive-tone photoresist was employed to yield voids that were subsequently filled gold *via* electrochemical deposition [8]. The achievable axial resolution is insufficient to fabricate more complex helical metamaterials as they have been discussed in Sections 3.2 and 3.4. The fabrication procedure was therefore modified, basing it on polymer structuring with STED-inspired direct laser writing that offers the necessary axial resolution but lacks the existence of compatible positive-tone photoresists. The entire process is also illustrated in Figure 4.8.

4.3.1 SUBSTRATE PREPARATION

Conventional microscopy glass cover slips with dimensions of 22 mm \times 22 mm and a thickness of 170 μm serve as the underlying substrate. The required conductivity of the substrate for electrochemical deposition is ensured by depositing a thin film (25 nm) of indium-tin oxide (ITO) onto the glass substrate *via* electron-beam evaporation. To ensure transparency of the ITO film, the substrate is subsequently tempered in a tube furnace at air atmosphere and a temperature of 450° C for 33 hours.

To improve adhesion of direct laser written polymer structures on bare and ITO-covered glass substrates, the substrates were silanized with a methacrylate-based silane. This increases the adhesion significantly as the molecule, covalently attached to the substrate, can be incorporated in the cross-linked polymer network during lithography. For this, an oxygen plasma etching was applied to the samples for 30 minutes, leading to hydroxy-groups at the surface. The formation of these necessary hydroxy-groups is easily achieved on bare glass substrates for which this silanization process was designed. Nevertheless, ITO-films can also form these groups under plasma exposure [114].

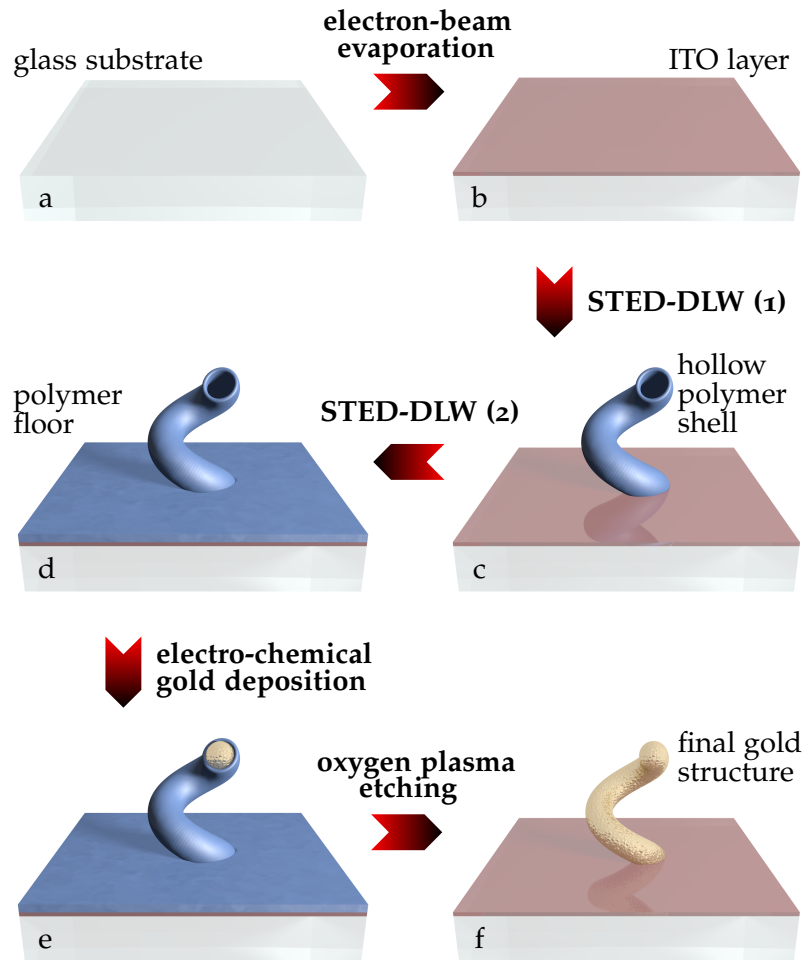


Figure 4.8: Illustration of the major steps during the fabrication process for helical gold metamaterials *via* STED-inspired direct laser writing (STED-DLW). A glass substrate (a) is covered by a thin film of indium-tin-oxide (ITO) and subsequently tempered and silanized (b). A polymer shell of the desired gold structure is written with STED-DLW (c). Without intermediate development, a second STED-DLW step is carried out to fabricate a polymer floor around the previously fabricated polymer structures (d). Gold is deposited inside the hollow polymer shells *via* electrochemical deposition (e). Finally, the polymer shell is removed with oxygen-plasma etching (f).

Following the plasma exposure, the substrates are immersed in a solution of 3-(trimethoxysilyl)propyl-methacrylate in toluene with a concentration of 1 mM. After one hour the samples are rinsed in demineralized water and blown dry with nitrogen.

Other approaches, based on the functionalization of the ITO film with phosphoric-acid-2-hydroxyethyl-methacrylate ester was also examined, however with no significant improvement of the polymer adhesion [115].

4.3.2 STED-INSPIRED DIRECT LASER WRITING

In contrast to previous publications, no positive-tone photoresist can be used. To avoid a much more challenging fabrication approach with multiple inversion steps, that will be discussed in Section 5.4, we instead write a polymer shell of the actual, desired structure. Figure 4.8(c) illustrates this for the case of a single helix with one pitch. The writing path is chosen such that z -component is increased continuously but slowly, while x - y -movement of the piezo stage serves to create the desired three-dimensional geometry. To allow for high writing speeds on the order of $60\ \mu\text{m/s}$ the piezo movement was overcompensated with a self-designed Fourier-based algorithm.

To furthermore prevent unwanted deposition of gold, before development, a polymer floor was written on top of the bare ITO film, covering the entire area between the shell structures. Additionally, the polymer-floor dimensions extended $30\ \mu\text{m}$ into any lateral direction from the edge of an array. This is necessary as, in contrast to Reference [113] where the positive-tone photoresist prevented gold deposition anywhere but in the written voids, here gold is subsequently deposited also on the entire substrate. The polymer floors were fabricated by meandering along the area with writing velocities of up to $200\ \mu\text{m/s}$ leaving holes only where the polymer shell structures had previously been created. The high speeds lead to significant lags of the piezo which in turn leads a lateral displacement of holes and shell structures, as illustrated in Figure 4.9(a). These lateral shifts were compensated by measuring the corresponding lateral shift from a piezo-coordinate readout.

After having written both, shell structures and floor, the samples were developed in the commercial solvent mr-Dev 600 (micro resist technology

GmbH) for a minimum of 15 minutes. Subsequently, the samples were rinsed with acetone and super-critically dried in carbon-dioxide (Leica EM CPD030). Super-critical drying prevents damages to the polymer templates due to capillary forces.

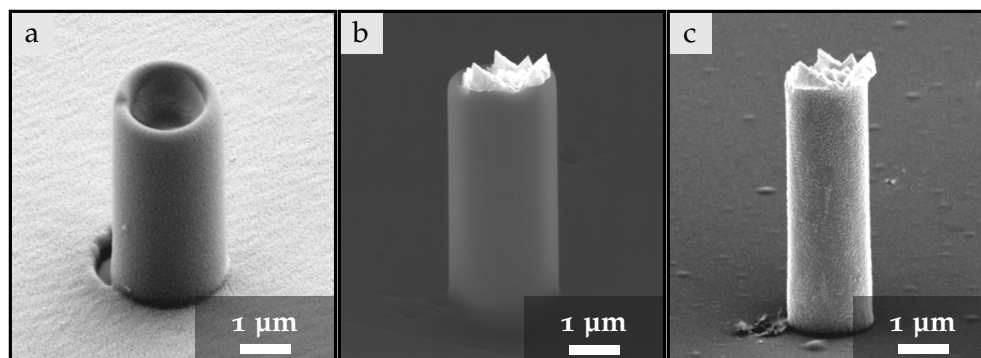


Figure 4.9: Scanning electron micrographs of a demonstration structure at different stages during fabrication. (a) Polymer structures after STED-inspired direct laser writing and development. The hollow polymer tube and the polymer floor are slightly misaligned in this instance for demonstration purposes. (b) After electrochemical deposition gold is visible (bright white), emerging from the top of the polymer structure. (c) After oxygen-plasma etching only the gold structure remains.

4.3.3 ELECTROCHEMICAL GOLD DEPOSITION

As the employed electrolyte is an aqueous solution, wetting of the polymer channels with diameters of well below one micron and depths of up to ten microns is a challenge. The reason for this is the low solubility of nitrogen in the electrolyte, in large contrast to the solubility of carbon-dioxide. Therefore, the samples were exposed to a pure carbon-dioxide atmosphere for a period of up to one hour and then immersed into demineralized water. The carbon-dioxide dissolves in the water and thus the water is pulled into the small voids. Subsequently, the samples were transferred into the electrolyte.

Alternatively, directly after development the samples were rinsed in acetone, isopropyl alcohol, and water and then transferred to the electrolyte

without intermediate drying, thus eliminating capillary forces and circumventing the problem of wetting all together. On the downside, intermediate characterization of these samples with far-field optical microscopy was not possible.

After a period of 20 minutes allowing on one hand for the water in the voids to be replaced by the electrolyte and the other hand for the temperature to be settled at 57° C, a current of $I = 0.758$ mA was applied, corresponding to a current density of $j = 2.68 \frac{\mu\text{A}}{\text{mm}^2}$. Here, I have assumed that the area is fixed at ($A = 28.26 \text{ mm}^2$) which is only an approximation as it should be corrected by the area covered by the polymer floor. As the area of the bare ITO film exposed to the electrolyte is two to three orders larger than that of the polymer floor, I have neglected this correction. With the current density given, the growth rate can be approximated from Equation 4.11 and yields for bulk gold ($z = 1$, $M = 197 \frac{\text{g}}{\text{mol}}$, $\rho = 19.3 \frac{\text{g}}{\text{cm}^3}$) a growth rate of $\frac{d_{\text{Au}}}{t} \approx 190 \frac{\text{nm}}{\text{min}}$.

Figure 4.9(b) depicts a similar polymer template as in (a) after electrochemical gold deposition. The desired height in this finger exercise was 5 μm and the deposition time was therefore set to 26.3 minutes. After polymer-removal, which is discussed in the following paragraph, a scanning electron microscope was used to determine the actual height to 5.169 μm . The error of the actual growth rate in that situation was therefore below 5%. However, the growth rate does depend heavily on the geometrical parameters of the polymer structure and the nearby environment. For smaller polymer-shell diameters, the growth rate decreases, as diffusion of complex ions to the electrode surface is hindered. Furthermore, for densely packed arrays a smaller growth rate is observed, as the supply of new complex ions is consumed over a larger area. Therefore, for each set of geometrical parameters, an empirical growth rate was determined. Nevertheless, the deviation from the approximation in Equation 4.11 remained small.

After deposition, the samples were amply rinsed with demineralized water to ensure that no electrolyte was left in any of the voids. Finally, the samples were dried under a nitrogen stream. In some instances, super-critical drying was applied at this point instead. However, the stability of the hybrid gold-polymer structure is usually high enough to withstand capillary forces and

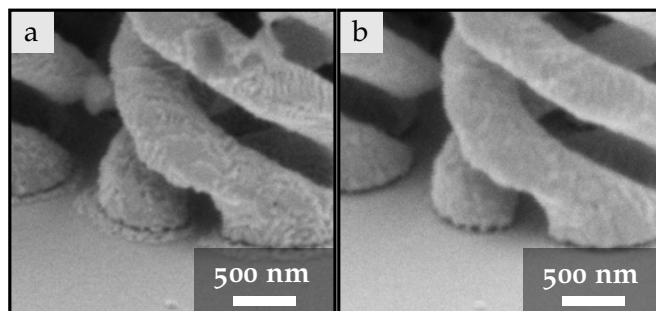


Figure 4.10: Scanning electron micrographs of fabricated gold structures before (a) and after (b) wet-etching with KI/I₂-based aqueous etchant. In (a) residual gold is evident around the gold structures. After etching, no residual is visible anymore in (b).

super-critical drying is therefore not necessary.

4.3.4 POLYMER REMOVAL AND POST-PROCESSING

In order to remove the polymer template that would diminish optical performance, the samples were placed upside down in a watch glass and exposed to oxygen plasma for a minimum of 16 hours. For densely packed arrays plasma-etching was repeated if necessary.

Despite silanization of the ITO-covered substrate prior to lithography, adhesion of the polymer structures is far from perfect. Especially for densely packed arrays the great number of tall, freestanding polymer structures in combination with the small polymer patches in between pose a great challenge. Even though still stable, very little detachment from the substrate surface is enough for gold electrolyte to diffuse into the created voids and form small gold particles during deposition. These particles, visible in the scanning electron micrograph in Figure 4.10(a) have a size on the order of approximately 50 nanometers. Due to the random distribution this would lead to scattering, a significantly lower transmission and, thus, to a strongly diminished optical performance. A wet-etching procedure was therefore employed. However, as the polymer template is already removed, the structures are highly vulnerable to capillary forces. Furthermore, one must ensure that the surface tension of the etchant does not hinder wetting of the entire array.

The latter challenge was tackled by again exposing the sample to a carbon-dioxide atmosphere. In contrast to the procedure before electrochemical deposition, the sample was not immersed into water, but ethanol which has a comparable solubility for carbon-dioxide [116], but a much lower surface tension [117]. From ethanol, the samples were transferred to water and subsequently etched in a commercial KI/I₂-based etchant (MicroChemicals TechniEtch ACI2) that had been diluted with water in a ratio of 1:9. The etch rate of approximately $6 \frac{\text{nm}}{\text{min}}$ was determined experimentally by measuring the thicknesses of larger gold structures before and after etching. Total etch times of 400 seconds were sufficient to completely remove the undesired gold residue as can be seen from Figure 4.10(b). The samples were subsequently rinsed in water, then transferred consecutively to water, isopropyl alcohol, and acetone and finally super-critically dried.

4.4 CIRCULAR-POLARIZATION INFRARED SPECTROSCOPY

In the final section of this chapter I will briefly discuss the method by which we characterize our fabricated metamaterials optically. As we are looking at lattice periods in the range of a few microns ($a = 1.5 - 3 \mu\text{m}$) supported by a glass substrate with refractive index $n \approx 1.5$, the minimum operation wavelengths where no higher diffracted orders occur are respectively $\lambda_{\text{min}} = 2.25 - 4.5 \mu\text{m}$. With bandwidths of typically more than one octave, the frequency range of interest therefore spreads across a large part of the midinfrared spectrum. Spectroscopy at these wavelengths is a particular challenge, as special optics are required for detection, focussing, and polarizing.

Here, we employ a commercial fourier-transform infrared (FTIR) spectrometer (Tensor 27, Bruker Optik GmbH) with a liquid-nitrogen cooled mercury-cadmium-telluride detector, that allows for detection of wavelengths of up to $13 \mu\text{m}$. However, glass strongly absorbs at wavelengths of approximately $6.5 \mu\text{m}$ and above. In order to obtain the best possible signal, $36\times$ Cassegrain objectives are used due to their lack of glass components. The opening angle of these objectives is however between 15° and 30° . To ensure normal incidence, we therefore tilt the samples by 22.5° and reduce the full opening angle of the Cassegrain objective with an off-centered small diaphragm to approximately 5° which corresponds to a numerical aperture of 0.044 [118]. The optical paths for both, reflection and transmission measurements are depicted in Figure 4.11.

Despite the use of reflecting optics only, the maximum wavelength for characterization in transmission is at approximately $6.5 \mu\text{m}$ due to the supporting glass substrates. The use of semiconductor substrates, *e.g.*, silicon would allow characterization over even larger bandwidths. Due the opacity at visible wavelengths, however, this would also require a modified fabrication process [61].

To achieve circular polarization for incoming light, we used a commercially available linear wiregrid polarizer (Thorlabs GmbH) in combination with a custom-built superachromatic MgF_2 -based quarter-waveplate (B. Halle Nachfl. GmbH). The wave plate has a phase error below 5% in the spectral

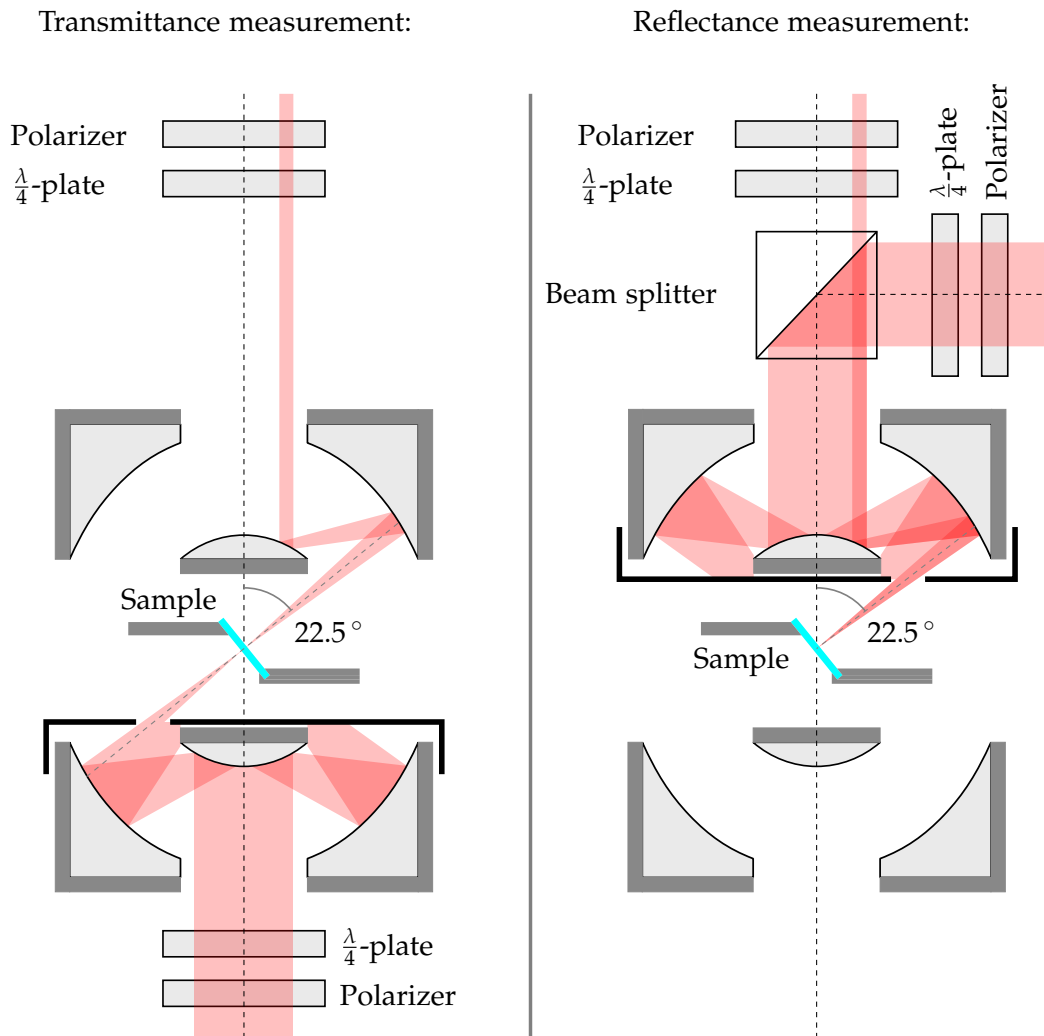
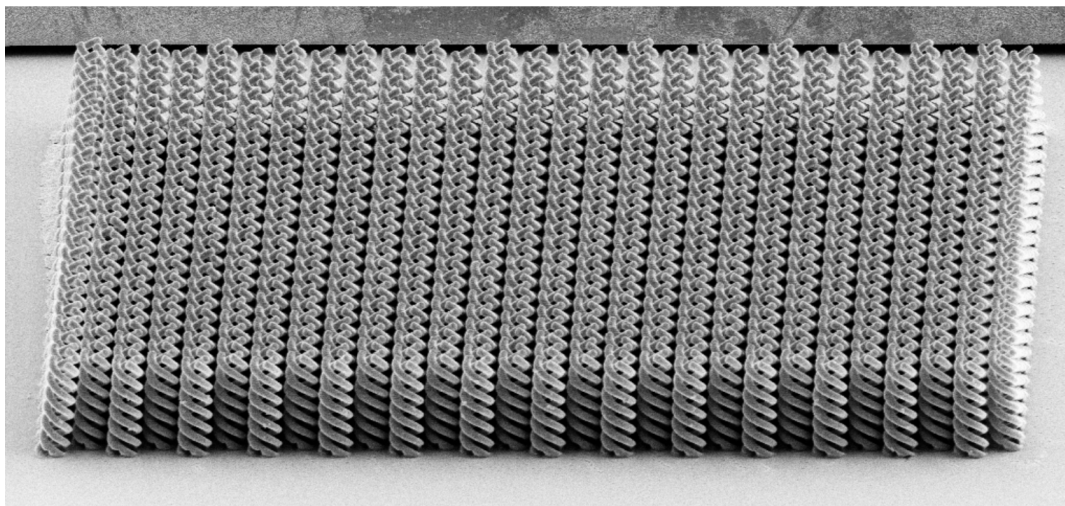


Figure 4.11: Optical paths for transmission and reflection measurement are depicted. In the former case, unpolarized light is incident from below. The aperture reduces the opening angle to 5% and a sample tilt of 22.5° ensures close to normal incidence. A combination of a linear polarizer and a quarter wave-plate before the first Cassegrain objective are used to achieve circular polarization. After the second Cassegrain objective the same combination in reverse order is used to discriminate between different circular polarizations. For reflection measurements, a beam splitter is added and light is coupled in from a side port above the sample. The remaining beam path is equivalent to that of transmission.

range of interest from 3 μm to 6 μm . The linear polarizer and wave plate are combined in a home-built holder that is inserted into the respective slot, depending on whether reflection or transmission is measured. The same combination in reverse order is used for analyzing the polarization after the sample and allows for a discrimination between polarization-conserving transmittances and conversions. Both are normalized to the polarization-conserving transmittances on the bare ITO-covered glass substrate.

5 Chapter 5

EXPERIMENTAL RESULTS



Scanning electron micrograph of $N = 3$ helical metamaterial.

In this chapter, I will present our experimental achievements in fabricating complex helical metamaterials for operation at mid-infrared frequencies. For this we have employed the fabrication process that was introduced in the previous chapter. Furthermore, I will present spectroscopic data showing broadband measurements for all elements of the Jones transmission and reflection matrices. I will first describe the results for the case of N -helices, here $N = 3$, followed by circular-polarization converters as they have been introduced in Section 3.4. I will also briefly discuss an alternative fabrication route, based on STED-inspired direct laser writing and a subsequent double-inversion process. Finally, I will conclude this chapter with a short overview on alternative fabrication approaches beyond laser lithography and a general discussion of the corresponding advantages and disadvantages.

5.1 TRIPLE-HELICAL METAMATERIALS

In Section 3.2 we have discussed N -helical metamaterials and their principle of operation. Here, I will now demonstrate the fabrication and spectroscopic data of such N -helices. The lowest degree of rotational symmetry that still fully eliminates circular-polarization conversions is $N = 3$. Therefore, we will focus on triple-helices arranged in a hexagonal lattice in the scope of this section, as it significantly facilitates fabrication.

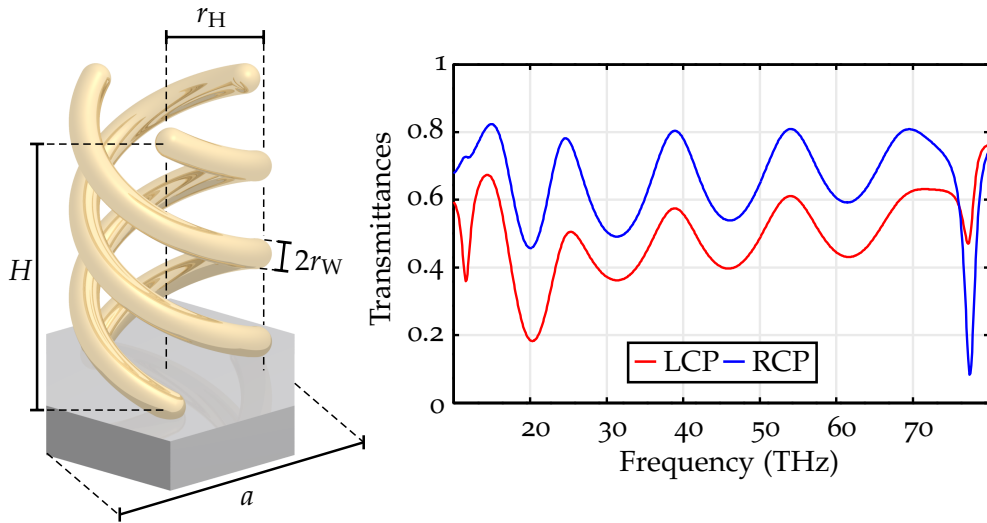


Figure 5.1: Illustration of a unit cell with indications of the geometrical parameters $a = 2.5 \mu\text{m}$, $H = 2.66 \mu\text{m}$, $r_H = 750 \text{ nm}$, and $r_W = 270 \text{ nm}$. On the right the corresponding numerical transmittance spectra are shown for a constituent Drude gold model. Circular-polarization conversions are not shown, as they are zero for symmetry reasons. Adapted from Reference [119].

The geometrical parameters discussed in Section 3.2 are despite STED-inspired lithography out of reach for our fabrication process. Therefore, more realistic geometrical parameters have been the target for fabrication. We will first take a look at numerically calculated spectra with geometrical parameters that have been achieved for $N = 3$ helices. The lateral lattice period is $a = 2.5 \mu\text{m}$, the helix radius $r_H = 750 \text{ nm}$, the pitch height $H = 2.66 \mu\text{m}$, and the wire radius $r_W = 270 \text{ nm}$. We have again assumed a

constituent Drude metal (see Chapter 3). The number of axial pitches is assumed to be $N_p = 2$ in the calculation. While a higher number of pitches would certainly also yield an improved optical performance, the challenge in fabricating such high structures rapidly increases. This aspect will be discussed in more detail in Section 5.3.

The corresponding transmittance spectra for the geometrical parameters described above are depicted in Figure 5.1. Pronounced circular dichroism is visible for frequencies from 10 THz to 75 THz, thus spanning across almost two octaves and the entire mid-infrared. Polarization conversions have been neglected in the diagram as they are zero.

Employing the fabrication procedure as it was described in the previous chapter, we fabricate hexagonal arrays of triple-helices with an overall footprint of $60 \mu\text{m} \times 60 \mu\text{m}$. The individual phases during fabrication are shown in Figure 5.2. For demonstration purposes a sample was developed after lithography and examined in the scanning electron microscope instead of further processing. The polymer template is depicted in Figure 5.2(a). Care must be taken, when designing the writing path for N -helices, as one might be tempted to create one helix after the other within one unit cell.

Due to proximity effects, however, the effective threshold would decrease

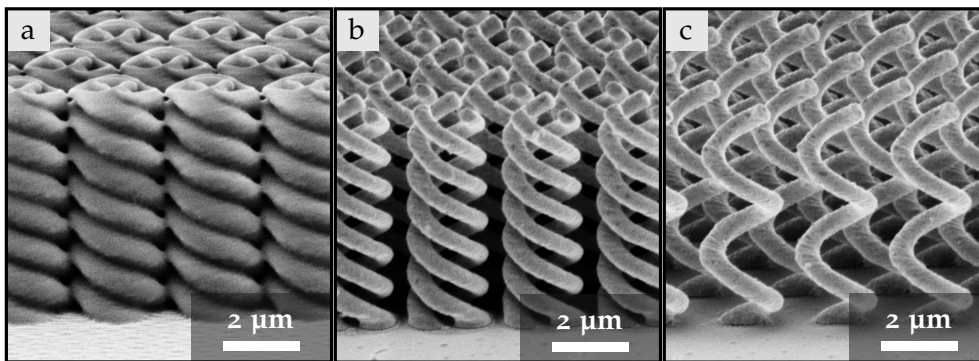


Figure 5.2: Scanning electron micrographs of a fabricated polymer template after development for demonstration purposes (a), the final $N = 3$ gold helices after removal of the polymer template (b), and single helices ($N = 1$) fabricated for a fair comparison on the same sample with identical geometrical parameters (c). Adapted from Reference [119].

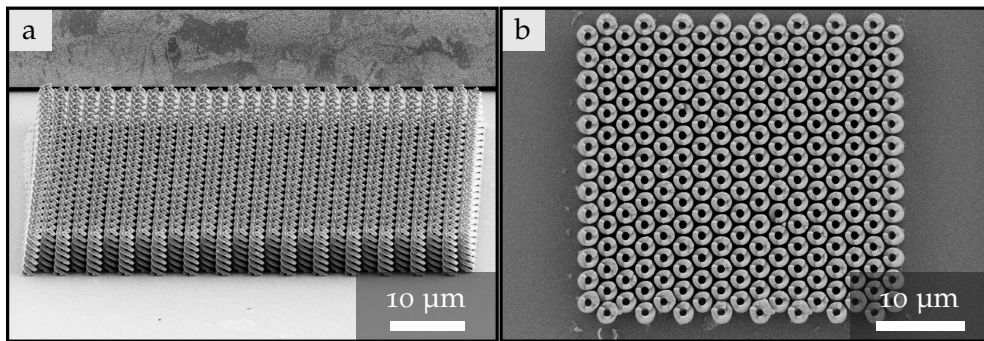


Figure 5.3: Scanning electron micrographs of the entire helical-metamaterial array viewed under an oblique angle (a) and from above (b). The periodicity and structural quality are underlined. In (a) the macroscopically large gold film that was grown next to the polymer floor is visible in the background.

slightly with every helix, leading to different exposure of each polymer shell, and therefore different wire thicknesses. By repetition in all unit cells, linear birefringence would be introduced and one would again obtain circular-polarization conversions. This could in fact be solved by choosing a random sequence for each unit cell. While 3-fold rotational symmetry would then be broken in each unit cell, the overall symmetry for many unit cells would be recovered. Here, we have instead used an approach allowing for 3-fold rotationally invariant unit cells, by writing a closed-loop path that creates the shell of all three helices simultaneously.

After electrochemical deposition and removal of the polymer templated *via* oxygen and wet-etching in order to remove the gold residue, the templates in 5.2(b) are obtained. As we have seen in the previous chapter, the height to which gold is deposited after a given time can be calculated very accurately. Due to the closely packed array and the helical path, the time was determined empirically with a series of identical samples. The desired height of two pitches was clearly met for this sample.

Furthermore, hexagonal arrays of single helices were fabricated as depicted in 5.2(c). This is important for a fair comparison of the achieved suppression of conversions. As I have briefly mentioned in Chapter 3, the magnitude of circular polarizations can be varied to a certain extent by varying the geometrical parameters. Therefore, on the same sample we have written additional arrays of $N = 3$ helix templates. In contrast to the ones described

above, the polymer floor was designed in such a way that two of the hollow tubes within a unit cell were sealed off. After subsequent electrochemical deposition and oxygen plasma etching, we obtained arrays of single helices with truly identical parameters.

Before we examine the optical spectra, let us first take a look at the periodicity and rotational symmetry of the fabricated arrays. From the scanning electron micrographs in Figure 5.3 it is evident that the periodicity in these arrays is superb. Furthermore, no difference between the individual helix wires within one unit cell can be seen with the bare eye.

We have characterized these arrays by mid-infrared circular-polarization far-field spectroscopy as I have introduced it in Section 4.4. In the following measurements, light impinges from the air side onto the helices. Spectra have been recorded for frequencies from 45 THz to 80 THz. For lower frequencies the supporting glass substrate is opaque. At higher frequencies, higher diffracted orders are present which are not part of the discussion here. Despite these restrictions, the measurement range still spans across almost one octave, a bandwidth that is already very challenging for achieving and analyzing circular polarization.

Let us now first take a look at the spectra in transmission for single helices, *i.e.*, $N = 1$ as depicted in Figure 5.4. In the left panels, corresponding numerical calculations are depicted. As expected for this array of left-handed helices, transmittance for left-circularly polarized light (LCP) is strongly suppressed, while the transmittance for right-circularly polarized light (RCP) is high. Circular-polarization conversions are depicted in the panel below and reach values of up to 7%. In the corresponding right panels the experimental data are depicted. Evidently, the qualitative and quantitative agreement between theory and experiment is good.

A grey dashed line, shown with the experimental conversions, depicts the measured polarization conversions on a bare substrate and is therefore a measure for the polarization error of the employed polarization optics. The measured polarization conversions are well above this line across the entire measurement range.

For $N = 3$ helices the calculated and measured spectra are depicted in

Figure 5.5. The calculations in the left-hand panels are the same as shown previously at the beginning of this section, but cropped to the frequency range of interest here. Note that circular-polarization conversions are indicated by dashed lines in the bottom panel. As expected, they are strictly zero. The experimental transmittances follow the trends nicely. There are some surprising features, especially for RCP. Fabrication imperfections might be one possible explanation. Furthermore, at 70 THz vibrational excitations of carbon-dioxide lead to very low signals and therefore measurement artifacts

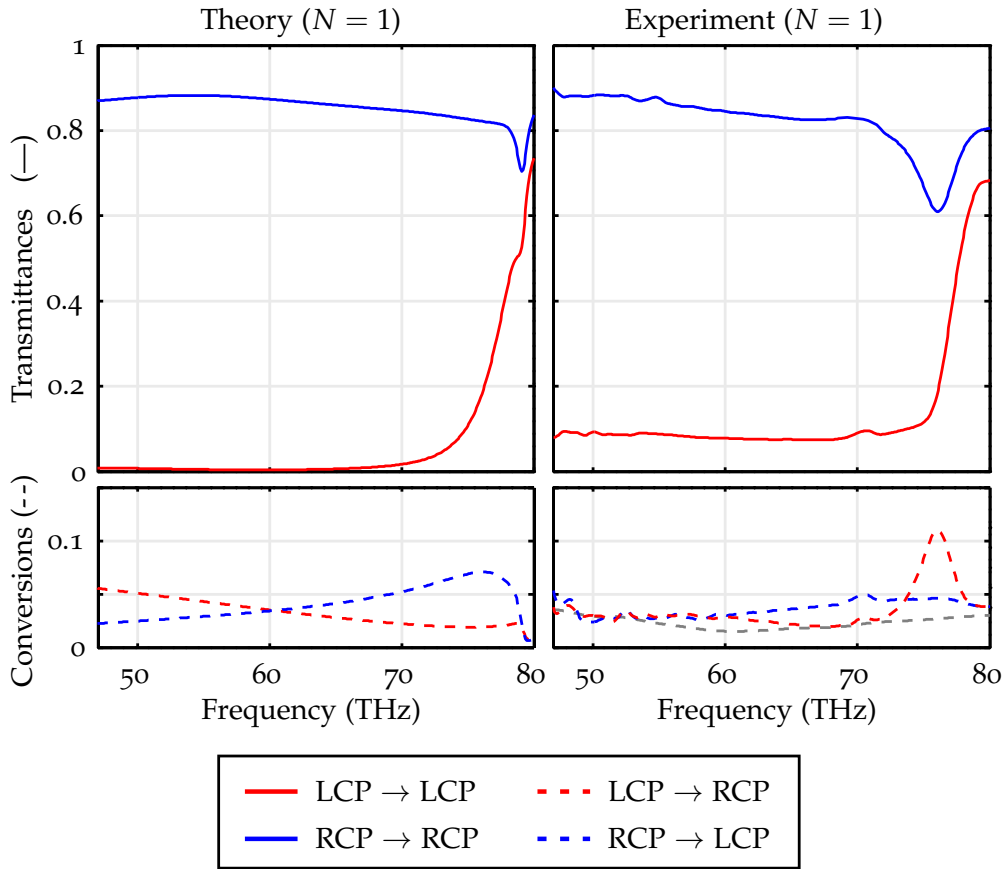


Figure 5.4: Calculated and measured transmittances are shown for the case of single helices, *i. e.*, $N = 1$ with two pitches. Numerically calculated spectra and measurement data are depicted in the left and right panels, respectively. The cross-polarizations of the bare substrate are indicated by a grey dashed line. Adapted from Reference [119].

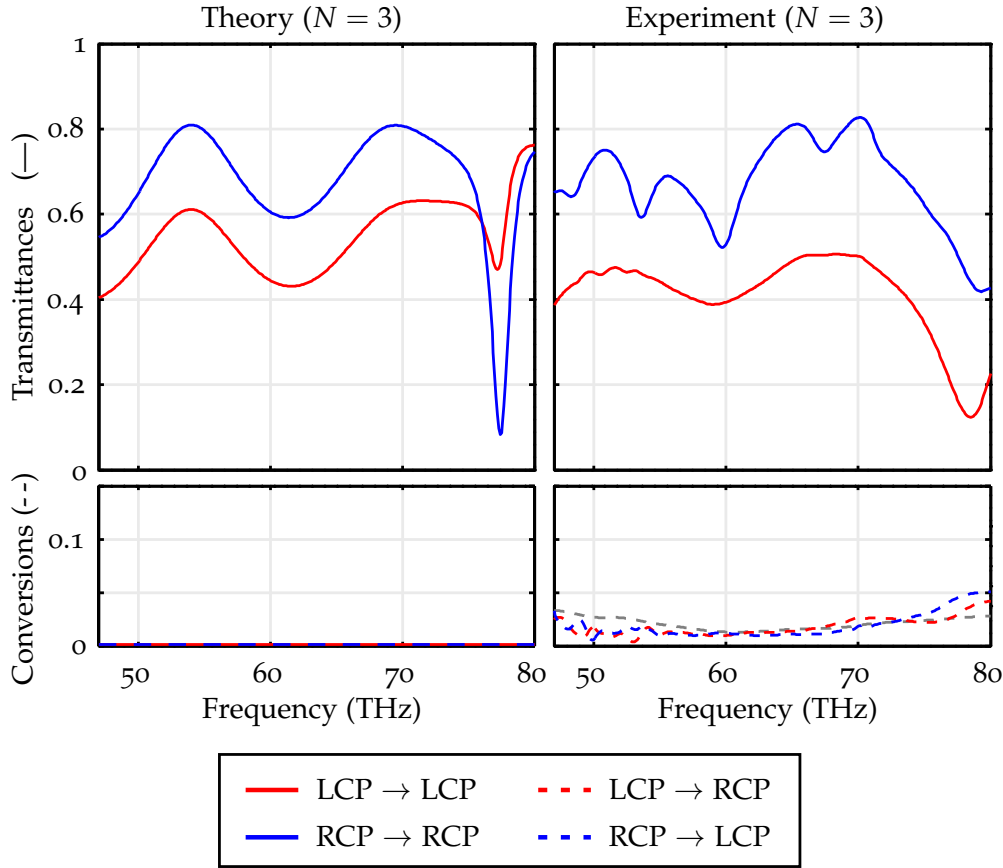


Figure 5.5: Calculated and measured transmittances are shown for the case of $N = 3$ helices with two pitches. Numerically calculated spectra and measurement data are depicted in the left and right panels, respectively. The cross-polarizations of the bare substrate are indicated by a grey dashed line. Adapted from Reference [119].

as the one seen here. Much more importantly, however, is the fact that circular-polarization conversions have successfully been suppressed to a degree where they cannot be distinguished from the polarization errors of the employed optics anymore (grey dashed line).

We have also measured the reflectance spectra that are depicted in Figure 5.6 for an array of single helices (a) and an array of $N = 3$ helices (b). Here, the effect of suppressing polarization conversions is even more striking. For $N = 1$, the blocked left circular polarization is reflected with the same

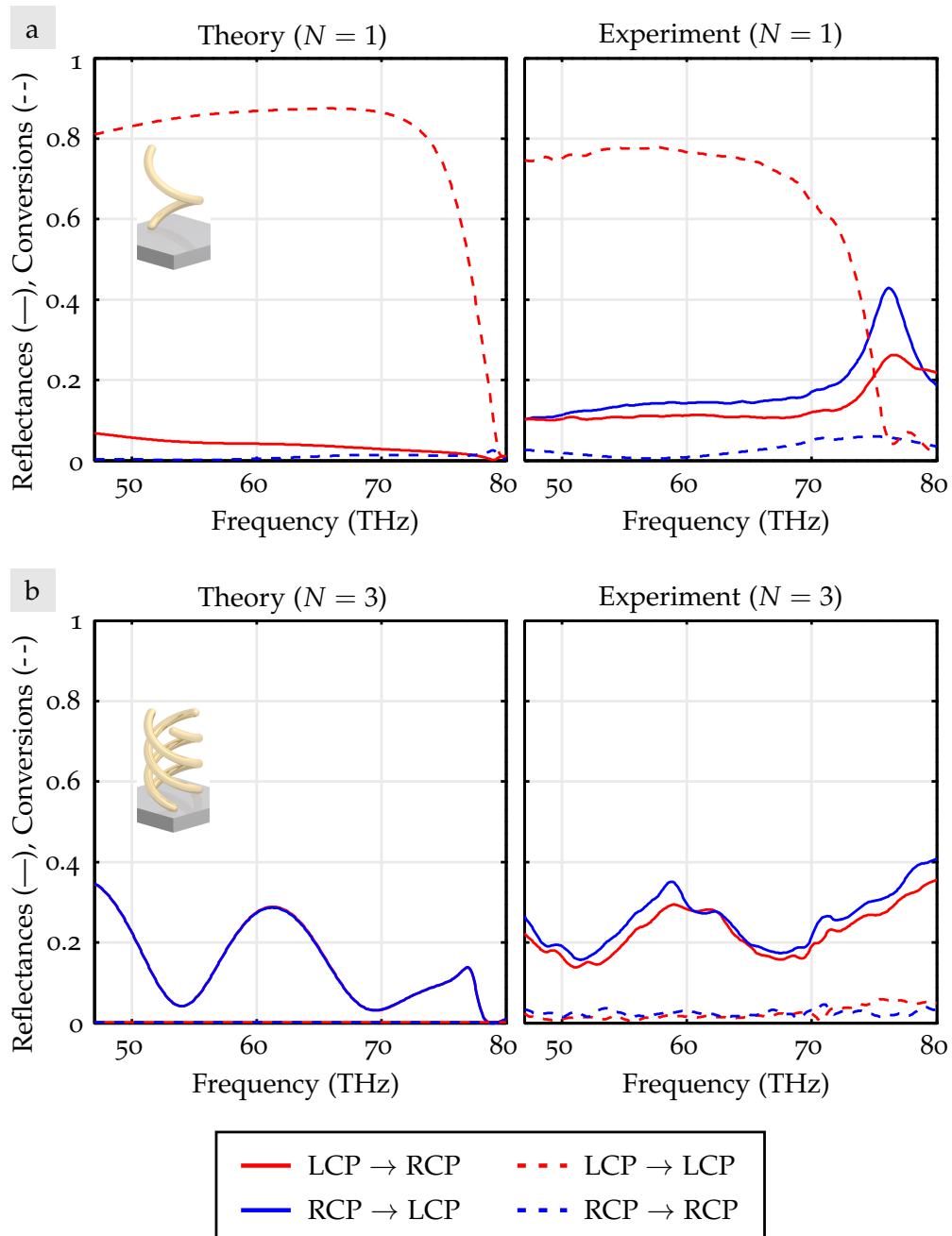


Figure 5.6: (a) Calculated and measured reflectances (solid lines), as well as conversions (dashed lines), are shown for the case of single helices, *i.e.*, $N = 1$ with two pitches. Numerically calculated spectra and measurement data are depicted in the left and right panels, respectively. (b) In analogy to (a) the corresponding spectra are shown for $N = 3$ helices. Adapted from Reference [119].

handedness, leading to a high conversion $|r_{LL}|^2$ of more than 80%. Again, the experimental data follow the trends nicely. The normal reflectances are slightly higher. For reciprocity reasons, they should furthermore be equal independent of any fabrication imperfections. This measurement artifact can therefore possibly be assigned to a sample tilt deviating from the targeted 22.5° which results in non-normal incidence. This could also explain the small peak that is visible at approximately 75 THz.

For $N = 3$ helices, circular-polarization conversions, *i. e.* $|r_{LL}|^2$ and $|r_{RR}|^2$, are close to zero as expected from the numerical calculations shown in the left panel and from our symmetry-based analysis in Chapter 3. Furthermore, the diagonal elements are close to equal, as expected from reciprocity reasoning.

In conclusion, I have shown in this section that we have successfully fabricated $N = 3$ helical metamaterials for operation at mid-infrared frequencies with very good structural quality and overall periodicity. The good agreement of the experimental data with the numerical calculations based on a constituent Drude metal furthermore suggests good metal quality – an advantage over some other fabrication approaches discussed in Subsection 5.4.2. I have furthermore shown experimental data for the squared moduli of the Jones transmission and the Jones reflection matrix in circular polarization basis for a frequency range of almost one octave. In the following section we will see how circular-polarization converters, as they have been introduced in Section 3.4, were fabricated in a similar way.

5.2 BROADBAND CIRCULAR-POLARIZATION CONVERTERS

In this section, I will present the experimental achievements in fabricating circular-polarization converters, as we have introduced them in Section 3.4. The therein discussed geometrical parameters shall also serve as the targeted parameters for fabrication here, *i.e.*, a lattice period of $a = 2 \mu\text{m}$, a helix radius of $r_H = 500 \text{ nm}$, a wire radius of $r_W = 250 \text{ nm}$, a connection arc radius $r_C = 400 \text{ nm}$, and an axial lattice period of $H = 2 \mu\text{m}$. Employing the same fabrication process as before, polymer templates were first fabricated on an ITO-covered glass substrate as depicted in the scanning electron micrograph in Figure 5.7(a). In order to compensate for inaccurate deposition times, the top half of the polymer template has two axial pitches instead of the targeted 1.5 pitches. The good structural quality and periodicity is evident.

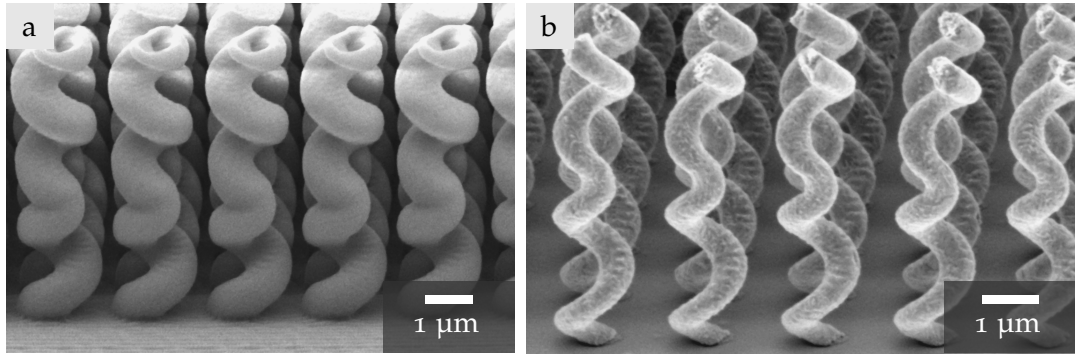


Figure 5.7: Scanning electron micrographs of circular-polarization converting helical metamaterial at different stages during fabrication. (a) Polymer templates after development. (b) Final gold structures after polymer removal. Adapted from Reference [118].

After electro-chemical gold deposition and subsequent removal of the polymer template, the gold structures in (b) were achieved. The lower right-handed helix has the targeted number of 1.5 axial pitches and the connection arc exhibits no sharp bends or variations in the wire thickness. The upper left-handed helix, however, has only one axial pitch. As shown in the numerical calculations in Appendix A, this does not affect the performance for circular-polarization conversion significantly. It does lead to a slightly

increased transmittance from LCP to LCP as can be intuitively understood, as the reflection of left-circularly polarized light is slightly decreased.

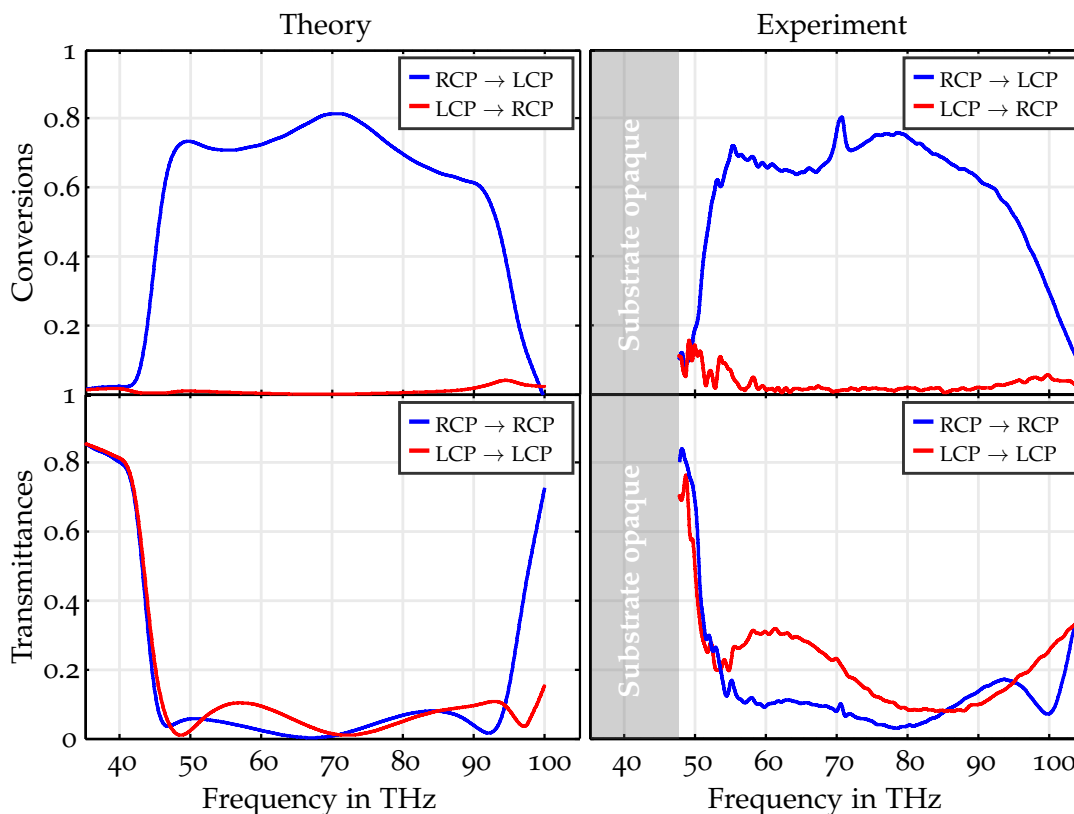


Figure 5.8: Calculated and experimental spectra are shown in the left and right panels, respectively. For the experimental spectra, a grey box has been added to indicate the spectral region in which the underlying glass substrate is opaque. Conversions are depicted in the top row, normal transmittances correspondingly in the bottom row. Reprinted from Reference [118].

Let us take a look at the experimental data. In Figure 5.8 I have plotted the corresponding numerical calculations on the left-hand side and the measured spectra respectively on the right. The squared moduli of the off-diagonal elements of the Jones transmission matrix in circular-polarization basis are depicted in the top row, the diagonal elements correspondingly in the bottom one. As before, we have restricted the measurements to frequencies above 47 THz due to absorptions of the glass substrates at longer wavelengths. This

is indicated by the grey box in the experimental spectra.

Examining the polarization conversions, one finds very good agreement with the theoretical spectra, both qualitatively and quantitatively. At 70 THz we again observe small deviations due atmospheric carbon-dioxide absorption. The squared moduli of the diagonal elements also show generally good agreement with the numerically calculated spectra. As previously mentioned the larger polarization-conserving transmittance for LCP is due to the slightly lower number of pitches of the upper helix in comparison to theory.

We recall furthermore that the observed difference in the two conversion spectra corresponds to the transmission asymmetry for each circular polarization with regard to forward or reverse propagation. With a bandwidth of one octave and conversions as well as asymmetry on the order of 60 % to 80 %, these results pose new benchmarks circularly polarized light.

We have therefore successfully demonstrated additional applications for our newly-developed fabrication process, allowing for record-breaking asymmetric circular-polarization conversions. As we have discussed in Section 3.4, coupling plays an important role for operation of this helical-metamaterial design. With the employed fabrication procedure the necessary resolution is at hand to allow for such feature sizes as the crucial connection arc. The geometrical parameter discussed in this and the previous section were chosen such that reproducible fabrication was ensured. For down-scaled geometrical parameters the reproducibility and therefore the overall structure quality and periodicity would suffer.

In the next section I will summarize the experimental achievements with regard to fabrication and will furthermore point out the advantages our the novel fabrication approach, as well as certain limitations.

5.3 DISCUSSION

The actual improvement for the newly introduced fabrication process is not easily quantifiable in terms of resolution or feature size. For pure STED-inspired direct laser writing (STED-DLW) of polymer structures, actual numbers of resolution improvement can be deduced from photonic crystal spectra [104]. However, these numbers cannot simply be adopted here. On one hand, feature sizes of previously fabricated designs were not limited by the resolution of the employed optics during lithography, but by the chemistry of the positive-tone photoresist [8, 63]. On the other hand, a fair comparison would require fabrication on the same sample and identical geometrical parameters.

In order to discuss the actual improvement yielded by this novel fabrication method (see Section 4.3), I will therefore compare metamaterials as they have been fabricated within in the scope of this thesis with previous publications on helical metamaterials [8, 63] qualitatively. The latter is shown in the scanning electron micrograph in Figure 5.9(a). Furthermore, the $N = 3$ helical metamaterial and the circular-polarization converters, both discussed in the previous sections, are shown in (b) and (c), respectively.

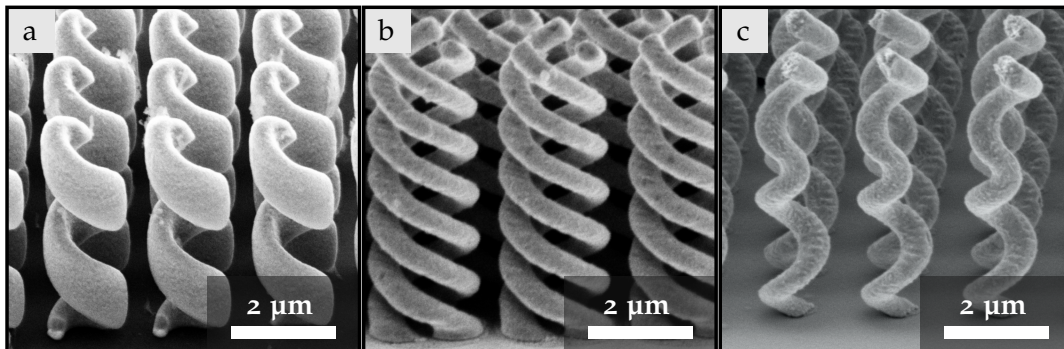


Figure 5.9: (a) Scanning electron micrographs of helical metamaterial fabricated by conventional direct laser writing in a positive-tone photoresist. Adapted from Reference [8]. Scanning electron micrographs of (b) $N = 3$ helical metamaterial and (c) circular-polarization converters fabricated by STED-DLW based approach.

It should be noted, that this comparison is not completely fair, as one should also examine helical metamaterials fabricated by conventional direct laser writing in a negative-tone photoresist similar to our STED-DLW based approach. I neglect this comparison, though, and instead refer to previous publications where the enhanced resolution of STED-DLW has been demonstrated [104]. From Figure 5.9, the improved aspect ratio and radius of the helix wire is evident. Simply by comparing the scanning electron micrographs, it is apparent that without this improvement, fabrication of these more sophisticated designs would not be possible for a fixed lattice period.

As we have discussed for $N = 3$ helices in Section 3.2, competitive extinction ratios can only be reached by increasing the number of axial pitches significantly. So far, we have only discussed the case of $N_p = 2$. Larger numbers of N_p are, however, challenging. With an increasing number of axial pitches, the distance z from the substrate also increases, leading to strong aberrations of the excitation and depletion focus. This effect is illustrated in Figure 5.10, where a polymer template with $N_p = 3.5$ was created.

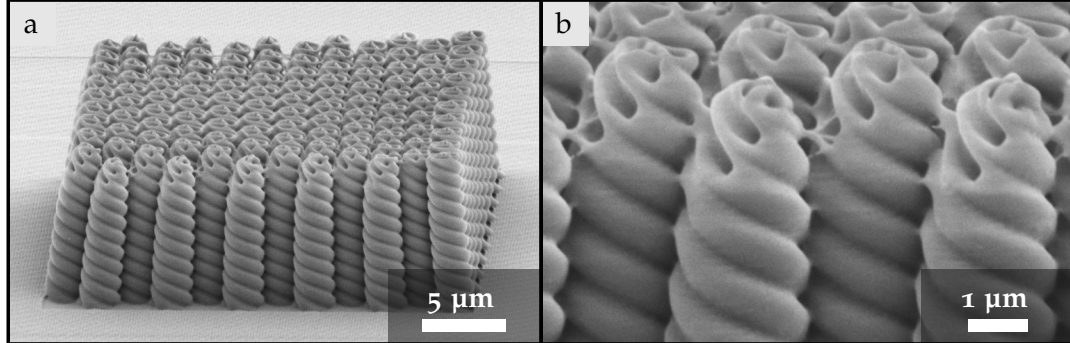


Figure 5.10: (a) Scanning electron micrographs of polymer template for $N = 3$ helical metamaterial with $N_p = 3.5$ axial pitches. (b) Zoom-in for the same polymer template. Under-exposed areas due to aberrations are clearly visible.

Especially in the zoom-in, shown in (b), underexposed areas are clearly visible (compare Figure 5.2(a)). Compensating the power in dependence of the z -position yields some improvement, but compensation factors must be determined empirically. In contrast, Dip-in STED-DLW allows for aberration-

free lithography [61]. Furthermore, heights of the fabricated structures are not limited by the working distance of the objective lens. Therefore, Dip-in STED-DLW could possibly allow for a much larger number of axial pitches in the future.

In the following section I will briefly outline a different fabrication approach, also based on STED-inspired direct laser writing that could allow for even smaller feature sizes. Furthermore, I will discuss fabrication techniques for helical metamaterials by other groups and their advantages and disadvantages in comparison to our method.

5.4 ALTERNATIVE FABRICATION APPROACHES

5.4.1 DOUBLE-INVERSION OF DIRECT LASER WRITTEN TEMPLATES

Even though our fabrication method is based on STED-inspired direct laser writing (STED-DLW) which yields a significantly improved resolution, a major drawback is the necessity to first create polymer shell templates. The need for a closed surface does not only increase the writing times, but also leads to a decrease in resolution again, due to proximity effects. Especially metamaterial designs with sharp bends are therefore challenging for this approach.

Here, I will briefly discuss an alternative approach that was developed in the scope of J. Qu's master thesis in our group and is also based on the creation of a polymer-template written *via* STED-DLW. Subsequently, however, the gold structures are achieved by a double-inversion process consisting of atom-layer deposition, reactive-ion etching, and electro-chemical gold deposition.

In a first step, the substrates were preprocessed as described in Section 4.3.1. By conventional direct laser writing polymer plane parallel to the substrate was written and supported by pillars and side-walls. To decrease process times significantly, the commercial direct laser writing setup Nanoscribe Professional GT (Nanoscribe GmbH) was used that allows for quick scanning of the laser focus by galvo-pivoted mirrors. Subsequently, using either conventional direct laser writing or STED-DLW – both in a negative-tone photoresist – arrays of the desired polymer structures were created below but in contact with the previously written roof-like structure. In contrast to our previously described approach, not the polymer shells but the positive of the desired structures were written, significantly decreasing writing times and proximity effects. *Via* atom-layer deposition the polymer samples, as well as the entire substrate were conformally covered with aluminum-oxide (Al_2O_3) with a thickness on the order 100 nm. Anisotropic reactive-ion etching was used to remove the top layer of aluminum-oxide from the roof and also from the bare ITO-covered substrate. After removing the polymer from within the Al_2O_3 -shell *via* oxygen plasma etching, electro-chemical gold deposition was used to fill the shells with gold. Finally, the aluminum-oxide shell was

removed in a wet-etching procedure with potassium hydroxide solution. The intermediate steps of the procedure are illustrated in the scanning electron micrographs in Figure 5.11 for an array of single helices where conventional direct laser writing was employed.

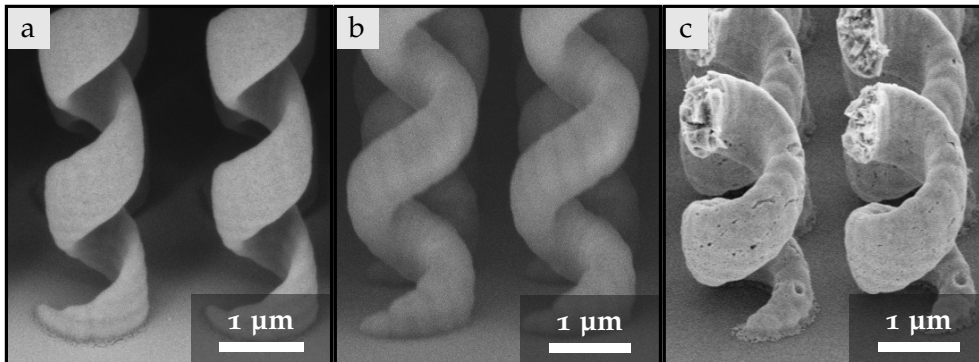


Figure 5.11: Scanning electron micrographs of helical metamaterial fabricated *via* an alternative fabrication approach. (a) Polymer template written with conventional direct laser writing. (b) Aluminum-oxide covered polymer template. (c) Final gold structures after removal of the aluminum-oxide *via* wet-etching. (courtesy of J. Qu).

This alternative approach has the advantage of exploiting the full achievable resolution of STED-inspired direct laser writing and, furthermore, allows for more freedom in the choice of the geometrical designs. Reproducibility of the process, as well as structure quality and periodicity of the final structures still requires improvement. Nevertheless, double-inversion approaches could offer true STED-DLW resolution improvement in the future.

5.4.2 FABRICATION APPROACHES BEYOND DIRECT LASER WRITING

In this final section, I will discuss approaches by other groups in fabricating helical metamaterials for operation at visible or infrared frequencies. I will put the corresponding advantages and disadvantages into perspective. Parts of this section have previously been submitted for publication in Reference [120].

FOCUSED-ION-BEAM INDUCED DEPOSITION

An alternative promising method for fabricating three-dimensional metallic metamaterials is decomposition of a gaseous precursor initiated by either a focused electron beam or a focused ion beam [121, 122]. As the basic principle of focused-ion-beam induced deposition (FIBID) and focused-electron-beam induced deposition (FEBID) is very similar, I will limit the discussion here to the former. Both methods, however, have been employed successfully for the fabrication of helical metamaterials [123].

The principle of FIBID is based on an ion beam that is focused onto a substrate covered with a platinum-based precursor. Fabrication has been demonstrated on silicon and gallium-nitride covered sapphire substrates, with the latter being transparent at visible frequencies and, thus, favorable for applications. Due to surface-charge effects, bare glass substrates cannot be used. The decomposition of the precursor leads to deposition of the solid metal, *e.g.*, platinum on the substrate. By slowly moving the position of the ion beam such that the subsequent exposure volume has an overlap with previously deposited material, three-dimensional structures can be created. Therefore, FIBID and FEBID are slightly more limited in the choice of the geometry in comparison to direct laser writing, as horizontal elements are inherently not possible. For most helical-metamaterial designs, this is not a limiting factor though. Advantageous on the other hand, is the enhanced resolution making feature sizes well below 100 nm and lattice constants for helical metamaterials down to 400 nm possible [123, 124].

Due to the complex interactions of ion beam, precursor, substrate, and already deposited nanostructure, deposition parameters have to be adjusted empirically to yield optimal structure quality. These deposition parameters, however, lead to a deteriorated composition of the constituent material, *i.e.*, an increase in carbon concentration and a decrease in platinum concentration [123]. This in turn, can lead to an inferior optical performance. Furthermore, one must note that the generally slow deposition speed on the order of tens of nanometers per second is reduced even further, due to local pressure reduction of the precursor. Therefore, for large-scale arrays so-called “refresh times” on the order of minutes have to be introduced after each individual helix to allow for precursor diffusion.

More recently, by exposing not an entire helix successively, but only thirds

of a pitch at a time, $N = 3$ helical metamaterials have been fabricated via FIBID [125]. This method can be extended to any arbitrary number of intertwined helices, limited only by the resolution.

Focused-ion-beam induced deposition is a promising candidate for future fabrication of complex helical metamaterials. While resolution and design freedom are two distinct advantages, slow writing speeds, the need for high-index substrates, and, most of all, inferior metal quality are the downside.

GLANCING-ANGLE DEPOSITION

While both, direct laser writing and focused-ion-beam induced deposition, offer great design freedom, fabrication of metamaterials on large-scale areas is out of reach. Parallelization of the fabrication can for example be achieved by physical vapor deposition under a glancing angle. With this technique porous films and metamaterials can be fabricated with feature sizes below one hundred nanometers. At the same time, the fabrication speed is increased by many orders of magnitude, as areas corresponding to the entire supporting wafer or substrate can be structured simultaneously. Glancing-angle deposition (GLAD) is based on inhomogeneous nucleation and, subsequently, a shadowing effect for physical vapor deposition under an oblique angle [126]. When rotating the substrate during evaporation, helical structures are formed. Furthermore, by structuring the template prior to GLAD, *e. g.*, *via* electron-beam lithography, growth can be restricted to certain periodic points on the substrate leading to an improved periodicity and structural quality. Until recently, however, GLAD was limited to dielectrics, as especially noble metals have high surface mobility, leading to atom diffusion and thus hindering the creation of complex three-dimensional structures [127]. The Ghosh group in 2013 circumvented this problem, by first creating a dielectric helical template via GLAD, which was subsequently covered with gold or silver nanoparticles by physical vapor deposition under a small tilt angle [128]. Due to self-shadowing and diffusion of the deposited metal atoms, no film of metal but isolated small metal islands are created. This leads to a strong chiro-optical response that can be further increased by increasing the thickness of the silver nanoparticles. On the downside, the overall transmittance will successively decrease and scattering losses due to randomly distributed metal nanoparticles are to be expected.

The Fischer group tackled the direct deposition of noble metals, by cooling the supporting substrate to a temperature of 170 K, therefore hindering atom diffusion [127, 129]. Furthermore, prior to GLAD, a self-assembly-based process was employed, in order to create periodically placed gold nanoparticles with controllable size on the substrate. Therefore, structuring with time-consuming electron-beam lithography is needless. Subsequently, the gold helices with two pitches were removed from the supporting substrate and suspended in aqueous solution. Corresponding circular-polarization transmission measurements exhibit strong circular dichroism at visible frequencies, despite the random spatial orientation of the helices. The bandwidth, on the other hand, is well below one octave.

By varying the composition of the evaporation flux, helical structures of different constituent materials or alloys can be created. With this, circular dichroism for silver-copper alloy helix arrays before removal from the supporting glass substrate has been demonstrated [129]. However, one must note, that in this case unwanted circular polarization conversions will again play a role and diminish the achievable extinction ratio. Similarly, the Zhao group has recently reported the fabrication of titanium-silver composite helices via GLAD [130].

In conclusion, glancing angle deposition has been shown to produce high quality metal helices with feature sizes on the order of tenth of nanometers, bringing circular dichroism to visible frequencies. Due to the parallel fabrication approach on the entire substrate or wafer, fabrication speeds surpass those of DLW, FIBID, and FEBID by many orders of magnitude. Slightly more complex designs and even the fabrication of composite structures consisting of more than one metal have been demonstrated.

For compact periodic helical metamaterials, GLAD approaches will always yield linear birefringence and, thus, circular polarization conversions. Furthermore, complex designs, as intertwined helices or super lattices for example, are inherently not possible with GLAD.

DNA-BASED SELF-ASSEMBLY

Self-assembly techniques are unrivalled in resolution by any top-down approach and are thus attractive for creating metamaterials for operation at visible frequencies. Furthermore, as fabrication can be parallelized to a large

extent, process times can be reduced considerably. For many years, however, self-assembly of metallic nanostructures has been limited to the fabrication of very simple designs. Over the past decade though, molecular linking of plasmonic nanoparticles has allowed for the fabrication of nanostructures that are more complex and in particular DNA has emerged as a paradigm linker for more sophisticated designs [131].

Recently, DNA-based self-assembly has also been employed to create helical nanostructures [132]. In a first step, DNA origami-folded helix-bundles were created. Gold nanoparticles (AuNPs) with a diameter of 10 nm were synthesized in solution and subsequently conjugated with thiolated ssDNA strands. These DNA-coated AuNPs were hybridized to the DNA origami structure, yielding either right-handed or left-handed helix formations of gold nanoparticles.

With this, resonant circular dichroism was observed for visible wavelengths with an amplitude, however, only on the order of millidegrees and thus orders of magnitude smaller than for GLAD approaches. The optical performance can, however, be enhanced by electroless gold deposition. This step increases the sizes of the nanoparticles and leads to a small, expected red-shift of the peak, but mostly increases the amplitude of the signal by a factor of approximately 400 [132].

Furthermore, composite shells, consisting of an alloy of gold and silver, can also be created, yielding the possibility to finely tune the spectral position and the amplitude of the CD signal. Nevertheless, helical nanostructures fabricated via DNA-based self-assembly show rather weak circular dichroism and small bandwidth, compared to the methods discussed in the previous paragraphs, resulting from the disconnected nanoparticle design. Furthermore, the formation of compact, periodic metamaterials is impossible. For solution-based applications, however, DNA-based self-assembly is a promising method. Parallelized large-scale fabrication of more complex designs is fundamentally possible and feature sizes presented so far are out of reach for top-down approaches like DLW and FIBID and even challenging for GLAD.

To conclude this section, I have summarized the three methods discussed above together with direct laser writing approaches Table 5.1 together with

Table 5.1: Fabrication approaches for helical metamaterials at optical or infrared frequencies. The corresponding publications and typical operation ranges are given, as well as general advantages and disadvantages.

Method	Spectral range	Advantages	Disadvantages
(STED-)DLW [8, 63, 118, 119]	Mid-infrared	high metal quality highest degree of design freedom	limited resolution low writing speeds
FIBID / FEBID [123–125]	Near-infrared	improved resolution large design freedom	low metal quality low writing speeds
GLAD [127–130]	Visible	small feature sizes fabrication of composites wafer-scale fabrication	low structural quality small bandwidths limited design freedom
DNA-based self-assembly [132]	Visible	small feature sizes easily scalable fabrication volume	small chiro-optical responses narrow bandwidths no ordered media

the characteristic strengths and weaknesses. Furthermore, a typical spectral range is given at which operation has been demonstrated for the corresponding technique.

With steadily increasing complexity of helical-metamaterial designs at a same time a demand for more advanced micro- and nanofabrication techniques. We have reviewed the recent advances in laser lithography and focused-ion-beam induced deposition. Both methods allow for the fabrication of highly complex three-dimensional metallic nanostructures for operation at mid- and near-infrared frequencies. On the other hand, fabrication techniques for wafer-scale fabrication have been introduced in the form of glancing-angle deposition and DNA-based self-assembly, bringing giant chiro-optical effects even to visible frequencies.

6

Chapter 6

CONCLUSIONS AND OUTLOOK

In the scope of this thesis, I have demonstrated both experimentally and theoretically that helical-metamaterial designs and applications are not limited merely to arrays of single helices and to operation as broadband circular polarizers. More sophisticated unit cells can be created where helices are used as the basic building blocks.

The theoretical aspects of more complex helical metamaterials were covered in Chapter 3. While arrays of single helices inherently exhibit undesired circular-polarization conversions, that stem from linear birefringence, I have shown theoretically that by recovering discrete rotational symmetry these conversions can be eliminated. With the analysis in Section 3.2, which is based on reciprocity and symmetry arguments, I have proven that there is a fundamental difference in the operation principle of any chiral metamaterial with discrete rotational symmetry in comparison to conventional helical metamaterials. Most importantly, losses are inherently necessary to achieve conversion-free circular-polarization capability as there simply cannot be any difference in reflection if only reciprocal constituent materials are at hand. This is in large contrast to the common wire-grid polarizer for linear polarization

I have furthermore discussed N -helical metamaterial designs where multiple intertwined helices within one unit cell recover the needed discrete rotational symmetry. Numerical calculations clearly support the previous theoretical arguments. Despite the fundamental difference of operation of

N -helical metamaterials in comparison to conventional helical metamaterials, strong circular dichroism is observed over similar or even larger bandwidths. The elimination of conversions, however, comes at a price of an inferior extinction ratio. In Section 3.3, I have demonstrated that competitive extinction ratios can be achieved by increasing the number of axial pitches. Additionally, tapering the helix radius along the helix axis allows for simultaneous enhancement of the extinction ratio and the relative bandwidth.

Instead of eliminating circular-polarization conversions, one can also aim at strongly enhancing one conversion and suppressing the other, leading to asymmetric transmission as I have shown in Section 3.4. Here, a helical-metamaterial design based on two coupled helices of opposite handedness was introduced, leading to record-breaking asymmetric circular polarization conversions over a bandwidth of approximately one octave. The operation principle, as well as the importance of coupling was discussed and illustrated *via* numerical calculations.

In Chapter 4, the experimental methods were introduced with which we have tackled the fabrication. The increased complexity of the proposed unit cells naturally also requires an improved resolution that conventional direct laser writing cannot offer. For this, I have reviewed the basics of diffraction-unlimited stimulated-emission-by-depletion inspired direct laser writing (STED-DLW). Furthermore, electro-chemical metal deposition was introduced. Based on these, I have described a novel fabrication approach allowing for a strongly enhanced resolution, in particular in the axial direction. Additionally, post-processing of the samples *via* subsequent chemical wet-etching to improve structure quality and optical performance was introduced and demonstrated.

I have illustrated the characterization method, employing broadband mid-infrared circular polarization optics and fourier-transform infrared spectroscopy.

Finally, in Chapter 5, I have presented our experimental achievements in fabricating the previously proposed helical-metamaterial designs for operation at mid-infrared frequencies. First, I have shown the successful realization of $N = 3$ helices with very good structural quality and overall

periodicity. Two axial pitches were demonstrated and corresponding optical measurements were in very good agreement with theory. The fabricated metamaterials exhibit strong circular dichroism over a large relative bandwidth of more than one octave and circular-polarization conversions were suppressed entirely.

Employing the same fabrication approach, the helical metamaterial design previously discussed in Section 3.4 was realized and asymmetric circular-polarization conversions of up to 80% over a relative bandwidth of one octave in the mid-infrared were measured. Up to date, this is the highest value achieved experimentally by a metamaterial design for broadband polarization conversion of circularly polarized light.

For both these metamaterial designs, fabrication based on conventional direct laser writing in a positive-tone resist does not offer the resolution needed to achieve the corresponding crucial features, namely intertwined helices and a connection arc with small bending radius, respectively.

Lastly, in Section 5.4, I have reviewed alternative fabrication approaches for helical metamaterials and the respective advantages and disadvantages.

Even though helical metamaterials can be seen as the analog to the well-known wire-grid polarizer for linear polarization, conversion-free broadband polarization capability is much more challenging. Driven by important applications like vibrational circular-dichroism spectroscopy, the ever-increasing number of helical-metamaterial designs in combination with newly emerging and constantly improving micro- and nano-fabrication approaches will bring true circular-polarization capabilities to visible, infrared, and terahertz frequencies. Furthermore, very little research has covered the effects of non-reciprocal constituent media – found in commonly used Faraday rotators and optical isolators – for helical metamaterials. In general, such a non-reciprocal metamaterial would allow for polarization-sensitive reflectance, even if circular polarization-conversions have been suppressed. It remains to be seen in the future, whether further improvements for reciprocal metamaterials or a non-reciprocal approach will allow for easily accessible circular polarization, the same way as the wire-grid polarizer has allowed for linear polarization.

A NUMERICAL PARAMETER SWEEP

We have examined the effects of varying geometrical parameters *via* extensive numerical calculations for the circular-polarization converters, as they have been introduced in Section 3.4. The squared moduli of the Jones transmission matrix are depicted on the following pages in dependence of three crucial parameters, the helix radius r_H , the axial pitch H , and the number of pitches N_p .

VARIATION OF THE HELIX RADIUS r_H

Figure A.1 shows the effects of different helix radii. As intuitively expected, this yields mainly a spectral shift. The targeted helical radius was chosen such that bandwidth and asymmetric conversion for circularly polarized light were both enhanced.

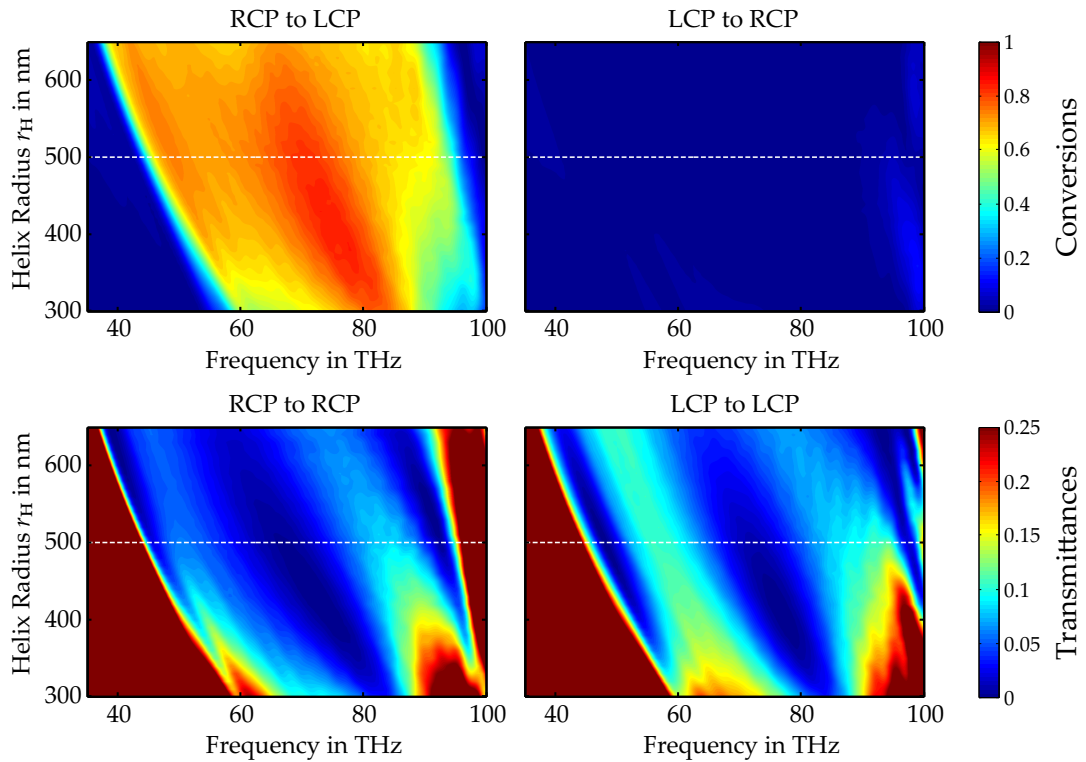


Figure A.1: Top row shows the circular-polarization conversion spectra for incoming RCP and LCP, respectively. The bottom row correspondingly shows the polarization-conserving transmittances for incoming RCP and LCP, however, plotted on a different color scale. A white, dashed line was added in all plots at $r_H = 500$ nm to indicate the desired geometrical parameter for optimized optical performance. Reproduced from Reference [118] (Supporting Online Information).

VARIATION OF THE AXIAL PITCH H

Figure A.2 shows the effects of different pitch heights H . The optimal pitch height is found for $H = a$, where a is the lateral lattice period.

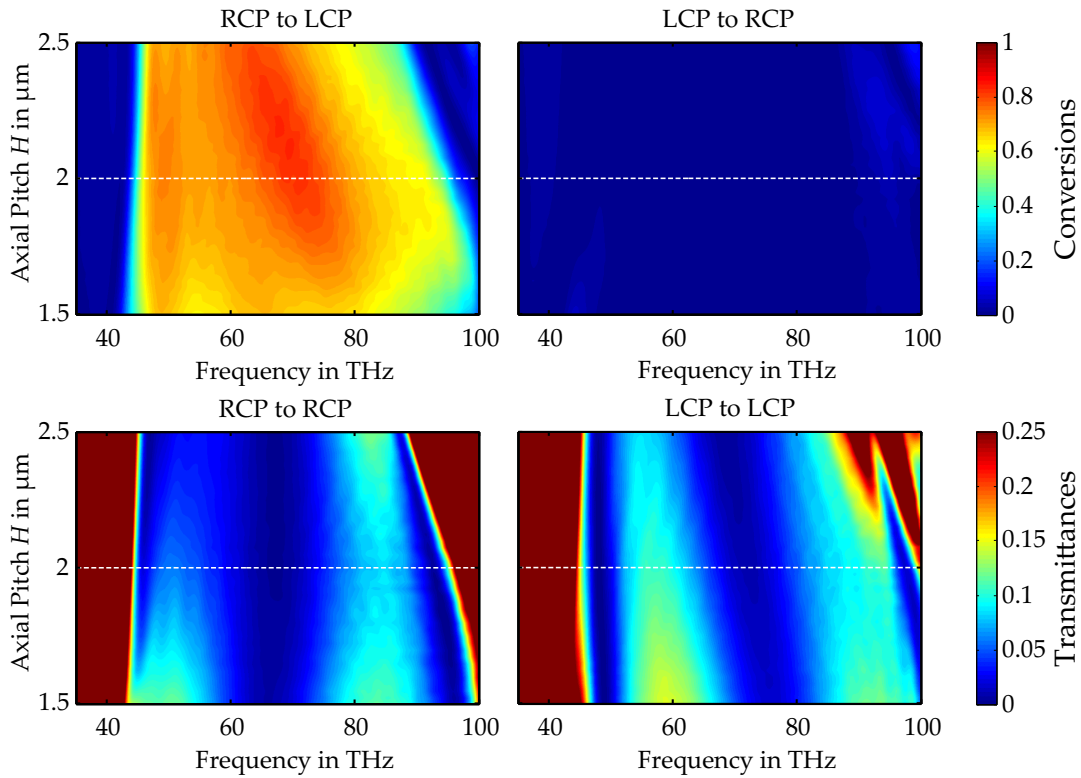


Figure A.2: Top row shows the circular-polarization conversion spectra for incoming RCP and LCP, respectively. The bottom row correspondingly shows the polarization-conserving transmittances for incoming RCP and LCP, however, plotted on a different color scale. A white, dashed line was added in all plots at $H = 2 \mu\text{m}$ to indicate the desired geometrical parameter for optimized optical performance. Reproduced from Reference [118](Supporting Online Information).

VARIATION OF THE NUMBER OF PITCHES N_p

Figure A.3 shows the effects of the number of pitches N_p of each helix. For any N_p broadband circular-polarization conversions are observed.

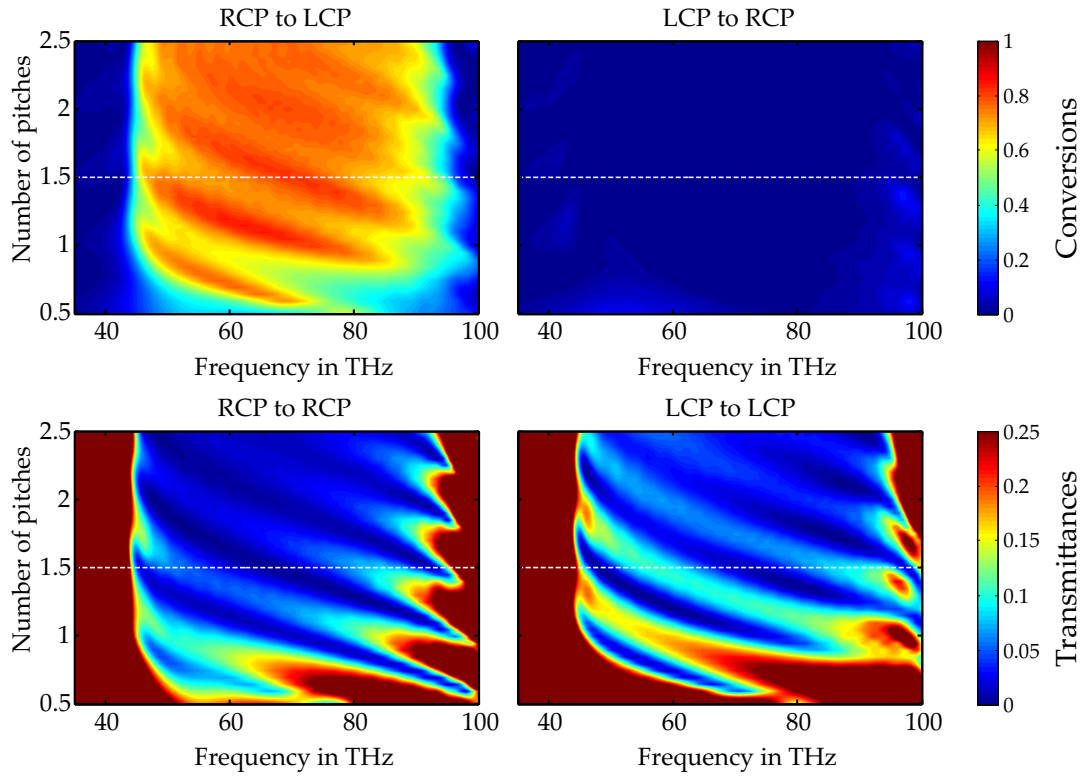


Figure A.3: Top row shows the circular-polarization conversion spectra for incoming RCP and LCP, respectively. The bottom row correspondingly shows the polarization-conserving transmittances for incoming RCP and LCP, however, plotted on a different color scale. A white, dashed line was added in all plots at $N = 1.5$ to indicate the desired geometrical parameter for optimized optical performance. Reproduced from Reference [118] (Supporting Online Information).

BIBLIOGRAPHY

- [1] W. Haidinger, "Ueber das directe Erkennen des polarisirten Lichts und der Lage der Polarisationsebene", *Ann. Phys.* **139**, 29–39 (1844) (Cited on page 5).
- [2] V. Westphal and S. W. Hell, "Nanoscale resolution in the focal plane of an optical microscope", *Phys. Rev. Lett.* **94**, 143903 (2005) (Cited on page 6).
- [3] S. Beychok, "Circular dichroism of biological macromolecules", *Science* **154**, 1288–1299 (1966) (Cited on page 7).
- [4] B. Ranjbar and P. Gill, "Circular dichroism techniques: Biomolecular and nanostructural analyses – A review", *Chem. Biol. Drug Des.* **74**, 101–120 (2009) (Cited on page 7).
- [5] R. D. Singh and T. A. Keiderling, "Vibrational circular dichroism of poly(γ -benzyl-L-glutamate)", *Biopolymers* **20**, 237–240 (1981) (Cited on page 7).
- [6] J.-H. Choi and M. Cho, "Terahertz chiroptical spectroscopy of an α -helical polypeptide: A molecular dynamics simulation study", *J. Phys. Chem. B* **118**, 12837–12843 (2014) (Cited on page 7).
- [7] V. K. Valev, J. J. Baumberg, C. Sibilia, and T. Verbiest, "Chirality and chiroptical effects in plasmonic nanostructures: Fundamentals, recent progress, and outlook", *Adv. Mater.* **25**, 2517–2534 (2013) (Cited on pages 7, 38).
- [8] J. K. Gansel, M. Thiel, M. S. Rill, M. Decker, K. Bade, V. Saile, G. von Freymann, S. Linden, and M. Wegener, "Gold helix photonic metamaterial as broadband circular polarizer", *Science* **325**, 1513–1515 (2009) (Cited on pages 7, 39, 40, 43, 84, 92, 115, 124).

- [9] E. Hecht, *Optik*, 5., verb. Aufl. (Oldenbourg, 2009) (Cited on pages [9](#), [17](#)).
- [10] B. E. A. Saleh and M. C. Teich, *Fundamentals of photonics*, 2. Ed. (Wiley, 2007) (Cited on pages [9](#), [13](#), [14](#)).
- [11] L. Novotny and B. Hecht, *Principles of nano-optics*, 1. publ. (Cambridge University Press, 2007) (Cited on pages [9](#), [15](#)).
- [12] W. Cai and V. Shalaev, *Optical metamaterials: Fundamentals and applications* (Springer, 2009) (Cited on pages [9](#), [31](#)).
- [13] J. C. Maxwell, "A dynamical theory of the electromagnetic field", English, *Philos. T. R. Soc. Lond.* **155**, 459–512 (1865) (Cited on page [10](#)).
- [14] J. C. Maxwell, *A treatise on electricity and magnetism*, Vol. 2 (Cambridge University Press, 2010) (Cited on page [10](#)).
- [15] J. Jackson, K. Müller, C. Witte, and M. Diestelhorst, *Klassische Elektrodynamik* (De Gruyter, 2014) (Cited on pages [10](#), [25](#)).
- [16] I. V. Lindell and A. J. Viitanen, "Eigenwaves in the general uniaxial bianisotropic medium with symmetric parameter dyadics", *Prog. Electromagn. Res.* **9**, 1–18 (1994) (Cited on pages [23–25](#)).
- [17] I. V. Lindell, *Electromagnetic waves in chiral and bi-isotropic media* (Artech House, 1994) (Cited on pages [23–25](#), [28](#)).
- [18] M. Hesse, H. Meier, and B. Zeeh, *Spektroskopische Methoden in der organischen Chemie : 102 Tabellen*, 7., überarb. Aufl. (Thieme, 2005) (Cited on page [26](#)).
- [19] H. Lorentz, "The theorem of Poynting concerning the energy in the electromagnetic field and two general propositions concerning the propagation of light", *Amsterdamer Akademie der Wetenschappen* **4**, 176 (1896) (Cited on page [28](#)).
- [20] A. Hoop, "A reciprocity theorem for the electromagnetic field scattered by an obstacle", English, *App. Sci. Res. B* **8**, 135–140 (1960) (Cited on page [28](#)).
- [21] R. J. Potton, "Reciprocity in optics", *Rep. Prog. Phys.* **67**, 717 (2004) (Cited on pages [28](#), [29](#)).

-
- [22] M. Born and E. Wolf, *Principles of optics: electromagnetic theory of propagation, interference and diffraction of light*, 6. Ed. (Cambridge University Press, 1999) (Cited on page 29).
- [23] N. P. Armitage, "Constraints on Jones transmission matrices from time-reversal invariance and discrete spatial symmetries", *Phys. Rev. B* **90**, 035135 (2014) (Cited on page 30).
- [24] D. R. Smith, W. J. Padilla, D. C. Vier, S. C. Nemat-Nasser, and S. Schultz, "Composite medium with simultaneously negative permeability and permittivity", *Phys. Rev. Lett.* **84**, 4184–4187 (2000) (Cited on page 31).
- [25] S. Linden, C. Enkrich, M. Wegener, J. Zhou, T. Koschny, and C. M. Soukoulis, "Magnetic response of metamaterials at 100 Terahertz", *Science* **306**, 1351–1353 (2004) (Cited on pages 32, 40).
- [26] N. Liu and H. Giessen, "Three-dimensional optical metamaterials as model systems for longitudinal and transverse magnetic coupling", *Opt. Express* **16**, 21233–21238 (2008) (Cited on page 32).
- [27] N. Liu, H. Liu, S. Zhu, and H. Giessen, "Stereometamaterials", *Nature Photon.* **3**, 157–162 (2009) (Cited on pages 32, 38).
- [28] C. E. Kriegler, M. S. Rill, S. Linden, and M. Wegener, "Bianisotropic photonic metamaterials", *IEEE J. Sel. Top. Quantum Electron.* **16**, 367–375 (2010) (Cited on pages 32, 33).
- [29] N. Liu and H. Giessen, "Coupling effects in optical metamaterials", *Angew. Chem. Int. Ed.* **49**, 9838–9852 (2010) (Cited on page 32).
- [30] M. Decker, N. Feth, C. M. Soukoulis, S. Linden, and M. Wegener, "Retarded long-range interaction in split-ring-resonator square arrays", *Phys. Rev. B* **84**, 085416 (2011) (Cited on page 32).
- [31] Y. Liu and X. Zhang, "Metamaterials: a new frontier of science and technology", *Chem. Soc. Rev.* **40**, 2494 (2011) (Cited on page 34).
- [32] C. M. Soukoulis and M. Wegener, "Past achievements and future challenges in the development of three-dimensional photonic metamaterials", *Nature Photon.* **5**, 523–530 (2011) (Cited on pages 34, 72).

- [33] J. B. Pendry, "Negative refraction makes a perfect lens", *Phys. Rev. Lett.* **85**, 3966–3969 (2000) (Cited on page 34).
- [34] V. M. Shalaev, W. Cai, U. K. Chettiar, H.-K. Yuan, A. K. Sarychev, V. P. Drachev, and A. V. Kildishev, "Negative index of refraction in optical metamaterials", *Opt. Lett.* **30**, 3356 (2005) (Cited on page 35).
- [35] G. Dolling, C. Enkrich, M. Wegener, C. M. Soukoulis, and S. Linden, "Low-loss negative-index metamaterial at telecommunication wavelengths", *Opt. Lett.* **31**, 1800–1802 (2006) (Cited on page 35).
- [36] G. Dolling, M. Wegener, and S. Linden, "Realization of a three-functional-layer negative-index photonic metamaterial", *Opt. Lett.* **32**, 551–553 (2007) (Cited on page 35).
- [37] G. Dolling, M. Wegener, C. M. Soukoulis, and S. Linden, "Negative-index metamaterial at 780 nm wavelength", *Opt. Lett.* **32**, 53–55 (2007) (Cited on page 35).
- [38] M. S. Rill, C. E. Kriegler, M. Thiel, G. von Freymann, S. Linden, and M. Wegener, "Negative-index bianisotropic photonic metamaterial fabricated by direct laser writing and silver shadow evaporation", *Opt. Lett.* **34**, 19–21 (2009) (Cited on page 35).
- [39] R. Fleury, F. Monticone, and A. Alù, "Invisibility and cloaking: Origins, present, and future perspectives", *Phys. Rev. Applied* **4**, 037001 (2015) (Cited on page 35).
- [40] J. B. Pendry, D. Schurig, and D. R. Smith, "Controlling electromagnetic fields", *Science* **312**, 1780–1782 (2006) (Cited on page 35).
- [41] U. Leonhardt, "Optical conformal mapping", *Science* **312**, 1777–1780 (2006) (Cited on page 35).
- [42] D. Schurig, J. J. Mock, B. J. Justice, S. A. Cummer, J. B. Pendry, A. F. Starr, and D. R. Smith, "Metamaterial electromagnetic cloak at microwave frequencies", *Science* **314**, 977–980 (2006) (Cited on page 35).
- [43] J. Li and J. B. Pendry, "Hiding under the carpet: a new strategy for cloaking", *Phys. Rev. Lett.* **101**, 203901 (2008) (Cited on page 35).

-
- [44] T. Ergin, N. Stenger, P. Brenner, J. B. Pendry, and M. Wegener, “Three-dimensional invisibility cloak at optical wavelengths”, *Science* **328**, 337–339 (2010) (Cited on page 35).
- [45] T. Ergin, J. Fischer, and M. Wegener, “Optical phase cloaking of 700 nm light waves in the far field by a three-dimensional carpet cloak”, *Phys. Rev. Lett.* **107** (2011) 10.1103/physrevlett.107.173901 (Cited on pages 35, 81).
- [46] R. Schittny, M. Kadic, T. Bückmann, and M. Wegener, “Invisibility cloaking in a diffusive light scattering medium”, *Science* **345**, 427–429 (2014) (Cited on page 35).
- [47] M. Decker, R. Zhao, C. M. Soukoulis, S. Linden, and M. Wegener, “Twisted split-ring-resonator photonic metamaterial with huge optical activity”, *Opt. Lett.* **35**, 1593–1595 (2010) (Cited on pages 35, 36, 38).
- [48] M. Decker, M. Ruther, C. E. Kriegler, J. Zhou, C. M. Soukoulis, S. Linden, and M. Wegener, “Strong optical activity from twisted-cross photonic metamaterials”, *Opt. Lett.* **34**, 2501–2503 (2009) (Cited on pages 35, 36, 38).
- [49] J. B. Pendry, “A chiral route to negative refraction”, *Science* **306**, 1353–1355 (2004) (Cited on page 36).
- [50] B. Wang, J. Zhou, T. Koschny, M. Kafesaki, and C. M. Soukoulis, “Chiral metamaterials: simulations and experiments”, *J. Opt. A – Pure Appl. Op.* **11**, 114003 (2009) (Cited on page 36).
- [51] Y. Zhao, M. Belkin, and A. Alu, “Twisted optical metamaterials for planarized ultrathin broadband circular polarizers”, *Nat. Commun.* **3**, 870 (2012) (Cited on pages 36, 38).
- [52] J. Wu, B. Ng, S. P. Turaga, M. B. H. Breese, S. A. Maier, M. Hong, A. A. Bettiol, and H. O. Moser, “Free-standing terahertz chiral meta-foils exhibiting strong optical activity and negative refractive index”, *Appl. Phys. Lett.* **103**, 141106, (2013) (Cited on page 36).
- [53] Y. Cui, L. Kang, S. Lan, S. Rodrigues, and W. Cai, “Giant chiral optical response from a twisted-arc metamaterial”, *Nano Lett.* **14**, 1021–1025 (2014) (Cited on pages 36, 38).

- [54] M. Li, L. Guo, J. Dong, and H. Yang, "An ultra-thin chiral metamaterial absorber with high selectivity for LCP and RCP waves", *J. Phys. D: Appl. Phys.* **47**, 185102 (2014) (Cited on page 36).
- [55] J. Wu, B. Ng, H. Liang, M. B. H. Breese, M. Hong, S. A. Maier, H. O. Moser, and O. Hess, "Chiral metafoils for terahertz broadband high-contrast flexible circular polarizers", *Phys. Rev. Applied* **2**, 014005 (2014) (Cited on page 36).
- [56] M. Hentschel, M. Schäferling, T. Weiss, N. Liu, and H. Giessen, "Three-dimensional chiral plasmonic oligomers", *Nano Lett.* **12**, 2542–2547 (2012) (Cited on page 38).
- [57] S. Takahashi, T. Tajiri, Y. Ota, J. Tatebayashi, S. Iwamoto, and Y. Arakawa, "Circular dichroism in a three-dimensional semiconductor chiral photonic crystal", *Appl. Phys. Lett.* **105**, 051107, (2014) (Cited on page 38).
- [58] M. Thiel, M. Decker, M. Deubel, M. Wegener, S. Linden, and G. von Freymann, "Polarization stop bands in chiral polymeric three-dimensional photonic crystals", *Adv. Mater.* **19**, 207–210 (2007) (Cited on page 38).
- [59] M. Thiel, G. von Freymann, and M. Wegener, "Layer-by-layer three-dimensional chiral photonic crystals", *Opt. Lett.* **32**, 2547–2549 (2007) (Cited on page 38).
- [60] M. Thiel, M. S. Rill, G. von Freymann, and M. Wegener, "Three-dimensional bi-chiral photonic crystals", *Adv. Mater.* **21**, 4680–4682 (2009) (Cited on page 38).
- [61] M. Thiel, J. Ott, A. Radke, J. Kaschke, and M. Wegener, "Dip-in depletion optical lithography of three-dimensional chiral polarizers", *Opt. Lett.* **38**, 4252–4255 (2013) (Cited on pages 38, 99, 117).
- [62] H. G. Liddell and R. Scott, *A Greek-English lexicon*, New (9.) Ed. (Clarendon Press, 1996) (Cited on page 38).
- [63] J. K. Gansel, M. Latzel, A. Frölich, J. Kaschke, M. Thiel, and M. Wegener, "Tapered gold-helix metamaterials as improved circular polarizers", *Appl. Phys. Lett.* **100**, 101109, (2012) (Cited on pages 39, 46, 57, 115, 124).

-
- [64] E. Plum, V. A. Fedotov, and N. I. Zheludev, "Extrinsic electromagnetic chirality in metamaterials", *J. Opt. A – Pure Appl. Op.* **11**, 074009 (2009) (Cited on page 40).
- [65] J. K. Gansel, M. Wegener, S. Burger, and S. Linden, "Gold helix photonic metamaterials: A numerical parameter study", *Opt. Express* **18**, 1059–1069 (2010) (Cited on pages 44, 56, 57).
- [66] L. Wu, Z. Yang, M. Zhao, P. Zhang, Z. Lu, Y. Yu, S. Li, and X. Yuan, "What makes single-helical metamaterials generate pure circularly polarized light?", *Opt. Express* **20**, 1552–1560 (2012) (Cited on page 44).
- [67] Z. Yang, M. Zhao, P. X. Lu, and Y. F. Lu, "Ultrabroadband optical circular polarizers consisting of double-helical nanowire structures", *Opt. Lett.* **35**, 2588–2590 (2010) (Cited on page 46).
- [68] Z. Yang, M. Zhao, and Y. F. Lu, "Similar structures, different characteristics: Optical performances of circular polarizers with single- and double-helical metamaterials", *J. Lightwave Technol.* **28**, 3055–3061 (2010) (Cited on page 46).
- [69] Z. Zhao, D. Gao, C. Bao, X. Zhou, T. Lu, and L. Chen, "High extinction ratio circular polarizer with conical double-helical metamaterials", *J. Lightwave Technol.* **30**, 2442–2446 (2012) (Cited on page 46).
- [70] J. Kaschke, J. K. Gansel, and M. Wegener, "On metamaterial circular polarizers based on metal N-helices", *Opt. Express* **20**, 26012–26020 (2012) (Cited on pages 47, 48, 50).
- [71] J. Kaschke, M. Blome, S. Burger, and M. Wegener, "Tapered N-helical metamaterials with three-fold rotational symmetry as improved circular polarizers", *Opt. Express* **22**, 19936–19946 (2014) (Cited on pages 47, 48, 50, 56).
- [72] C. Menzel, C. Rockstuhl, and F. Lederer, "Advanced jones calculus for the classification of periodic metamaterials", *Phys. Rev. A* **82**, 053811 (2010) (Cited on pages 47, 48).
- [73] I. Fernandez-Corbaton, "Forward and backward helicity scattering coefficients for systems with discrete rotational symmetry", *Opt. Express* **21**, 29885–29893 (2013) (Cited on page 48).

- [74] Z. Yang, M. Zhao, and P. X. Lu, "Improving the signal-to-noise ratio for circular polarizers consisting of helical metamaterials", *Opt. Express* **19**, 4255–4260 (2011) (Cited on page 50).
- [75] P. Zhang, Z. Yang, M. Zhao, L. Wu, Z. Lu, Y. Cheng, R. Gong, Y. Zheng, and J. Duan, "Similar structures, different characteristics: circular dichroism of metallic helix arrays with single-, double-, and triple-helical structures", *J. Opt. Soc. Am. A* **30**, 677–681 (2013) (Cited on page 55).
- [76] M. Schäferling, X. Yin, N. Engheta, and H. Giessen, "Helical plasmonic nanostructures as prototypical chiral near-field sources", *ACS Photonics* **1**, 530–537 (2014) (Cited on page 62).
- [77] M. Mutlu, A. E. Akosman, A. E. Serebryannikov, and E. Ozbay, "Diode-like asymmetric transmission of linearly polarized waves using magnetoelectric coupling and electromagnetic wave tunneling", *Phys. Rev. Lett.* **108**, 213905 (2012) (Cited on page 65).
- [78] C. Menzel, C. Helgert, C. Rockstuhl, E.-B. Kley, A. Tünnermann, T. Pertsch, and F. Lederer, "Asymmetric transmission of linearly polarized light at optical metamaterials", *Phys. Rev. Lett.* **104**, 253902 (2010) (Cited on page 65).
- [79] N. K. Grady, J. E. Heyes, D. R. Chowdhury, Y. Zeng, M. T. Reiten, A. K. Azad, A. J. Taylor, D. A. R. Dalvit, and H.-T. Chen, "Terahertz metamaterials for linear polarization conversion and anomalous refraction", *Science* **340**, 1304–1307 (2013) (Cited on page 65).
- [80] S.-C. Jiang, X. Xiong, Y.-S. Hu, Y.-H. Hu, G.-B. Ma, R.-W. Peng, C. Sun, and M. Wang, "Controlling the polarization state of light with a dispersion-free metastructure", *Phys. Rev. X* **4**, 021026 (2014) (Cited on page 65).
- [81] Y. Li, J. Zhang, S. Qu, J. Wang, H. Chen, Z. Xu, and A. Zhang, "Wideband selective polarization conversion mediated by three-dimensional metamaterials", *J. Appl. Phys.* **115**, 234506, (2014) (Cited on page 65).
- [82] H. Shi, J. Li, A. Zhang, J. Wang, and Z. Xu, "Broadband cross polarization converter using plasmon hybridizations in a ring/disk cavity", *Opt. Express* **22**, 20973–20981 (2014) (Cited on page 65).

- [83] Y. Xu, Q. Shi, Z. Zhu, and J. Shi, "Mutual conversion and asymmetric transmission of linearly polarized light in bilayered chiral metamaterial", *Opt. Express* **22**, 25679–25688 (2014) (Cited on page 65).
- [84] W. Zhang, W. M. Zhu, E. E. M. Chia, Z. X. Shen, H. Cai, Y. D. Gu, W. Ser, and A. Q. Liu, "A pseudo-planar metasurface for a polarization rotator", *Opt. Express* **22**, 10446–10454 (2014) (Cited on page 65).
- [85] P. Zhang, M. Zhao, L. Wu, Z. Lu, Z. Xie, Y. Zheng, J. Duan, and Z. Yang, "Giant circular polarization conversion in layer-by-layer nonchiral metamaterial", *J. Opt. Soc. Am. A* **30**, 1714–1718 (2013) (Cited on page 65).
- [86] C. Wu, N. Arju, G. Kelp, J. A. Fan, J. Dominguez, E. Gonzales, E. Tutuc, I. Brener, and G. Shvets, "Spectrally selective chiral silicon metasurfaces based on infrared Fano resonances", *Nat. Commun.* **5**, (2014) (Cited on page 65).
- [87] C. Pfeiffer, C. Zhang, V. Ray, L. J. Guo, and A. Grbic, "High performance bianisotropic metasurfaces: Asymmetric transmission of light", *Phys. Rev. Lett.* **113**, 023902 (2014) (Cited on page 65).
- [88] L. Wu, Z. Yang, Y. Cheng, R. Gong, M. Zhao, Y. Zheng, J. Duan, and X. Yuan, "Circular polarization converters based on bi-layered asymmetrical split ring metamaterials", English, *Appl. Phys. A Mater. Sci. Process.* **116**, 643–648 (2014) (Cited on page 65).
- [89] H. F. Ma, G. Z. Wang, G. S. Kong, and T. J. Cui, "Broadband circular and linear polarization conversions realized by thin birefringent reflective metasurfaces", *Opt. Mater. Express* **4**, 1717–1724 (2014) (Cited on page 65).
- [90] J. D. Kraus, *Antennas*, 2. Ed. (McGraw-Hill, 1988) (Cited on page 67).
- [91] C. Rockstuhl, F. Lederer, C. Etrich, T. Pertsch, and T. Scharf, "Design of an artificial three-dimensional composite metamaterial with magnetic resonances in the visible range of the electromagnetic spectrum", *Phys. Rev. Lett.* **99**, 017401 (2007) (Cited on page 72).
- [92] G. von Freymann, A. Ledermann, M. Thiel, I. Staude, S. Essig, K. Busch, and M. Wegener, "Three-dimensional nanostructures for photonics", *Adv. Funct. Mater.* **20**, 1038–1052 (2010) (Cited on page 72).

- [93] J. K. Hohmann, M. Renner, E. H. Waller, and G. von Freymann, “Three-dimensional μ -printing: An enabling technology”, *Adv. Opt. Mater.* (2015) 10.1002/adom.201500328 (Cited on pages 72, 76).
- [94] S. Kawata, H.-B. Sun, T. Tanaka, and K. Takada, “Finer features for functional microdevices”, *Nature* 412, 697–698 (2001) (Cited on page 72).
- [95] M. Straub and M. Gu, “Near-infrared photonic crystals with higher-order bandgaps generated by two-photon photopolymerization”, *Opt. Lett.* 27, 1824–1826 (2002) (Cited on page 72).
- [96] M. Deubel, G. von Freymann, M. Wegener, S. Pereira, K. Busch, and C. M. Soukoulis, “Direct laser writing of three-dimensional photonic-crystal templates for telecommunications”, *Nat. Mater.* 3, 444–447 (2004) (Cited on page 72).
- [97] M. Thiel, J. Fischer, G. von Freymann, and M. Wegener, “Direct laser writing of three-dimensional submicron structures using a continuous-wave laser at 532 nm”, *Appl. Phys. Lett.* 97, 221102, (2010) (Cited on page 74).
- [98] T. Bückmann, N. Stenger, M. Kadic, J. Kaschke, A. Frölich, T. Kennerknecht, C. Eberl, M. Thiel, and M. Wegener, “Tailored 3d mechanical metamaterials made by dip-in direct-laser-writing optical lithography”, *Adv. Mater.* 24, 2710–2714 (2012) (Cited on page 76).
- [99] A. W. Schell, J. Kaschke, J. Fischer, R. Henze, J. Wolters, M. Wegener, and O. Benson, “Three-dimensional quantum photonic elements based on single nitrogen vacancy-centres in laser-written microstructures”, *Sci. Rep.* 3, 1577– (2013) (Cited on page 76).
- [100] J. Fischer, “Three-dimensional optical lithography beyond the diffraction limit”, PhD thesis (Institute of Applied Physics, Karlsruhe Institute of Technology, 2012) (Cited on pages 77, 79, 82).
- [101] J. Fischer and M. Wegener, “Three-dimensional optical laser lithography beyond the diffraction limit”, *Laser Photonics Rev.* 7, 22–44 (2013) (Cited on pages 77, 78).

-
- [102] S. W. Hell and J. Wichmann, "Breaking the diffraction resolution limit by stimulated emission: stimulated-emission-depletion fluorescence microscopy", *Opt. Lett.* **19**, 780–782 (1994) (Cited on page 79).
- [103] E. Rittweger, K. Y. Han, S. E. Irvine, C. Eggeling, and S. W. Hell, "STED microscopy reveals crystal colour centres with nanometric resolution", *Nature Photon.* **3**, 144–147 (2009) (Cited on page 79).
- [104] J. Fischer and M. Wegener, "Three-dimensional direct laser writing inspired by stimulated-emission-depletion microscopy", *Opt. Mater. Express* **1**, 614–624 (2011) (Cited on pages 81, 83, 115, 116).
- [105] A. Frölich, J. Fischer, T. Zebrowski, K. Busch, and M. Wegener, "Titania woodpiles with complete three-dimensional photonic bandgaps in the visible", *Adv. Mater.* **25**, 3588–3592 (2013) (Cited on page 81).
- [106] J. Fischer, J. B. Mueller, J. Kaschke, T. J. A. Wolf, A.-N. Unterreiner, and M. Wegener, "Three-dimensional multi-photon direct laser writing with variable repetition rate", *Opt. Express* **21**, 26244–26260 (2013) (Cited on page 81).
- [107] J. B. Mueller, J. Fischer, F. Mayer, M. Kadic, and M. Wegener, "Polymerization kinetics in three-dimensional direct laser writing", *Adv. Mater.* **26**, 6566–6571 (2014) (Cited on page 81).
- [108] J. Fischer, G. von Freymann, and M. Wegener, "The materials challenge in diffraction-unlimited direct-laser-writing optical lithography", *Adv. Mater.* **22**, 3578–3582 (2010) (Cited on page 83).
- [109] S.-J. Zhang, Y. Li, Z.-P. Liu, J.-L. Ren, Y.-F. Xiao, H. Yang, and Q. Gong, "Two-photon polymerization of a three dimensional structure using beams with orbital angular momentum", *Appl. Phys. Lett.* **105**, 061101 (2014) (Cited on page 84).
- [110] M. S. Rill, C. Plet, M. Thiel, I. Staude, G. von Freymann, S. Linden, and M. Wegener, "Photonic metamaterials by direct laser writing and silver chemical vapour deposition", *Nat. Mater.* **7**, 543–546 (2008) (Cited on page 84).
- [111] M. Paunović and M. Schlesinger, *Fundamentals of electrochemical deposition*, 2. Ed. (Wiley-Interscience, 2006) (Cited on pages 84, 86, 89).

- [112] R. G. Ehl and A. J. Ihde, "Faraday's electrochemical laws and the determination of equivalent weights", *J. Chem. Educ.* **31**, 226 (1954) (Cited on page 89).
- [113] J. K. Gansel, "Helical optical metamaterials", PhD thesis (Institute of Applied Physics, Karlsruhe Institute of Technology, 2012) (Cited on pages 90, 94).
- [114] M.-S. Kang, H. Ma, H.-L. Yip, and A. K.-Y. Jen, "Direct surface functionalization of indium tin oxide via electrochemically induced assembly", *J. Mater. Chem.* **17**, 3489–3492 (2007) (Cited on page 92).
- [115] S. E. Koh, K. D. McDonald, D. H. Holt, C. S. Dulcey, J. A. Chaney, and P. E. Pehrsson, "Phenylphosphonic acid functionalization of indium tin oxide: surface chemistry and work functions", *Langmuir* **22**, 6249–6255 (2006) (Cited on page 94).
- [116] I. Dalmolin, E. Skovroinski, A. Biasi, M. Corazza, C. Dariva, and J. V. Oliveira, "Solubility of carbon dioxide in binary and ternary mixtures with ethanol and water", *FFE* **245**, 193–200 (2006) (Cited on page 98).
- [117] G. Vazquez, E. Alvarez, and J. M. Navaza, "Surface tension of alcohol + water from 20 to 50° C", *J. Chem. Eng. Data* **40**, 611–614 (1995) (Cited on page 98).
- [118] J. Kaschke, L. Blume, L. Wu, M. Thiel, K. Bade, Z. Yang, and M. Wegener, "A helical metamaterial for broadband circular polarization conversion", *Adv. Opt. Mater.* **3**, 1411–1417 (2015) (Cited on pages 99, 112, 113, 124, 130–132).
- [119] J. Kaschke and M. Wegener, "Gold triple-helix mid-infrared metamaterial by STED-inspired laser lithography", *Opt. Lett.* **40**, 3986–3989 (2015) (Cited on pages 104, 105, 108–110, 124).
- [120] J. Kaschke and M. Wegener, "Optical and infrared helical metamaterials", *Nanophotonics*, accepted (Cited on page 119).
- [121] S. Matsui, T. Kaito, J.-i. Fujita, M. Komuro, K. Kanda, and Y. Haruyama, "Three-dimensional nanostructure fabrication by focused-ion-beam chemical vapor deposition", *J. Vac. Sci. Technol. B* **18**, 3181–3184 (2000) (Cited on page 120).

-
- [122] I. Utke, P. Hoffmann, and J. Melngailis, "Gas-assisted focused electron beam and ion beam processing and fabrication", *J. Vac. Sci. Technol. B* **26**, 1197–1276 (2008) (Cited on page 120).
- [123] M. Esposito, V. Tasco, M. Cuscunà, F. Todisco, A. Benedetti, I. Tarantini, M. D. Giorgi, D. Sanvitto, and A. Passaseo, "Nanoscale 3D chiral plasmonic helices with circular dichroism at visible frequencies", *ACS Photonics* **2**, 105–114 (2015) (Cited on pages 120, 124).
- [124] M. Esposito, V. Tasco, F. Todisco, A. Benedetti, D. Sanvitto, and A. Passaseo, "Three dimensional chiral metamaterial nanospirals in the visible range by vertically compensated focused ion beam induced-deposition", *Adv. Opt. Mater.* **2**, 154–161 (2014) (Cited on pages 120, 124).
- [125] M. Esposito, V. Tasco, F. Todisco, M. Cuscunà, A. Benedetti, D. Sanvitto, and A. Passaseo, "Triple-helical nanowires by tomographic rotatory growth for chiral photonics", *Nat. Commun.* **6**, 6484 (2015) (Cited on pages 121, 124).
- [126] D.-X. Ye, T. Karabacak, R. C. Picu, G.-C. Wang, and T.-M. Lu, "Uniform Si nanostructures grown by oblique angle deposition with substrate swing rotation", *Nanotechnology* **16**, 1717–1723 (2005) (Cited on page 121).
- [127] A. G. Mark, J. G. Gibbs, T.-C. Lee, and P. Fischer, "Hybrid nanocolloids with programmed three-dimensional shape and material composition", *Nat. Mater.* **12**, 802–807 (2013) (Cited on pages 121, 122, 124).
- [128] J. H. Singh, G. Nair, A. Ghosh, and A. Ghosh, "Wafer scale fabrication of porous three-dimensional plasmonic metamaterials for the visible region: chiral and beyond", *Nanoscale* **5**, 7224–7228 (2013) (Cited on pages 121, 124).
- [129] J. G. Gibbs, A. G. Mark, S. Eslami, and P. Fischer, "Plasmonic nanohelix metamaterials with tailorable giant circular dichroism", *Appl. Phys. Lett.* **103**, 213101, (2013) (Cited on pages 122, 124).

- [130] G. K. Larsen, Y. He, J. Wang, and Y. Zhao, “Scalable fabrication of composite Ti/Ag plasmonic helices: Controlling morphology and optical activity by tailoring material properties”, *Adv. Opt. Mater.* **2**, 245–249 (2014) (Cited on pages 122, 124).
- [131] S. J. Tan, M. J. Campolongo, D. Luo, and W. Cheng, “Building plasmonic nanostructures with DNA”, *Nat. Nanotechnol.* **6**, 268–276 (2011) (Cited on page 123).
- [132] A. Kuzyk, R. Schreiber, Z. Fan, G. Pardatscher, E.-M. Roller, A. Högele, F. C. Simmel, A. O. Govorov, and T. Liedl, “DNA-based self-assembly of chiral plasmonic nanostructures with tailored optical response”, *Nature* **483**, 311–314 (2012) (Cited on pages 123, 124).

ACKNOWLEDGMENTS

I would like to kindly thank many people who have played a role in the successful completion of this thesis and without who this work would not have been possible.

First of all, I would like to thank Prof. Dr. Martin Wegener for the opportunity to work in his group on this challenging but exciting topic. The support has been outstanding throughout the entire time.

I also thank Prof. Dr. Carsten Rockstuhl for agreeing in taking the time to serve as the second examiner and reviewer.

A lot of the work discussed in this thesis would not have been possible without collaboration partners. Here, I would like to thank in particular Dr. Klaus Bade for technical support and for providing us with the gold electrolyte. Similarly, I am very grateful for the help and the numerical calculations that Dr. Sven Burger and Dr. Mark Blome have provided. I thank also Prof. Dr. Yang ZhenYu and Wu Lin with who I have had the pleasure of working together both in Karlsruhe and in Wuhan.

I also want to thank Dr. Joachim Fischer, Dr. Justyna Gansel, Dr. Michael Thiel, and Dr. Manuel Decker who have either supervised my work or who have been open for questions and discussions. With Jingyuan Qu and Leonard Blume, I had the pleasure of working with in the scope of their master and diploma thesis, respectively, and I thank them for the fruitful discussions and shared research.

Furthermore, I have always enjoyed going to work in the morning thanks to the entire group. I want to thank especially Dr. Benjamin Richter, Dr. Tiemo Bückmann, Dr. Alexander Quick, and Andreas Wickberg, who have become more than just colleagues. I am also very happy to have shared a lab with Dr. Jonathan Müller who was always open for discussions and with whom I have enjoyed working closely together.

Research is, however, not possible without people who work in the back-

ground. I would like to thank the entire secretary staff, Renate Helfen, Claudia Alaya, and Monica Brenkmann, for keeping our amount of paperwork to a minimum. Thanks also go out to Johann Westhauser who has helped with many technical everyday things but most of all, has designed crucial mechanical components for the electrochemical deposition process and fourier-transform spectrometer. Also, I would like to thank the electronics workshop Helmut Lay, Michael Hippe, and Werner Gilde, who have ensured a perfect IT-environment.

Thanks also to all the proof readers, Dr. Robert Schittny, Andreas Wickberg, Jingyuan Qu, Patrick Müller, Dr. Benjamin Richter, and Claudia Niemeyer, who have helped to keep mistakes in this thesis to a minimum.

Finally, I would like to thank people who have been supporting me for much longer than the time of my PhD thesis. I thank my parents for believing in me, supporting me, and kindling an interest in physical sciences from early on and my sister Maria for always being there for me, if I need her.

Most of all, I thank my girlfriend Claudia, who has supported and helped me throughout the last years, who has always been there for me, and who had to endure my moods lately. I am truly blessed in having found her.